Palladium Based Compounds as Efficient and Durable Electrode Materials Towards Electrochemical Energy Production in Fuel Cells

A Thesis submitted in partial fulfilment for the degree of

Master of Science

as a part of

Integrated Ph.D. Programme (Chemical Science)

By

Mr. Saurav Chandra Sarma

New Chemistry Unit

Jawaharlal Nehru Centre for Advanced Scientific Research

(A Deemed University)

Bangalore-560064 (INDIA)

March 2016

Dedicated to my family

and teachers

Declaration

I hereby declare that the matter embodied in the thesis entitled "**Palladium Based Compounds as Efficient and Durable Electrode Materials Towards Electrochemical Energy Production in Fuel Cells**" is the result of investigations carried out by me at the New Chemistry Unit, Jawaharlal Nehru Centre for Advanced Scientific Research, Bengaluru, India under the supervision of Dr. Sebastian C. Peter and that it has not been submitted elsewhere for the award of any degree or diploma.

In keeping with the general practice in reporting scientific investigations, due acknowledgement has been made wherever the work described is based on findings of other investigators. Any omission that might have occurred by oversight or error of judgement is regretted.

Date: ----------

Bengaluru, India Saurav Chandra Sarma

Certificate

I hereby declare that the matter embodied in the thesis entitled "**Palladium Based Compounds as Efficient and Durable Electrode Materials Towards Electrochemical Energy Production in Fuel Cells**" has been carried out by Mr. Saurav Chandra Sarma at the New Chemistry Unit, Jawaharlal Nehru Centre for Advanced Scientific Research, Bengaluru, India under my supervision and that it has not been submitted elsewhere for the award of any degree or diploma.

Date: ----------

Bengaluru, India Dr. Sebastian C. Peter

Acknowledgements

Ideas, they say, are laid waste without effort. This project began as an idea and traversed through many phases before becoming what it is today. It is a culmination of efforts, research, suggestions and enthusiasm of all the people who have encouraged me in this work. The project report would seem incomplete if I fail to acknowledge those who have made it see the light of the day.

I would like to express my sincere gratitude and heartfelt thanks to my mentor **Dr**. **Sebastian C. Peter, New Chemistry Unit, Jawaharlal Nehru Centre for Advanced Scientific Research** for his unflinching support and guidance throughout the project. His words of wisdom and expertise in subject matter were of immense help right from the beginning of the project.

I would like to express my sincere thanks to **Prof. C. N. R. Rao, FRS, the Chairman, New Chemistry Unit, Jawaharlal Nehru Centre for Advanced Scientific Research** for being the source of inspiration, generous support and encouragement throughout my JNC life. I also thank him for providing the infrastructure and necessary facilities to carry out my research work.

I would like to thank all my course instructors for their excellent courses**.**

My sincere thanks to all the technical staff of NCU and CPMU, especially Mr. Sreenivas, Mr. Anil, Mrs. Usha, Mrs. Bhavya, Ms. Selvi, Mr. Jagadish, Mr. Mahesh and Mr. Vasu for their help with the various characterization techniques.

I am thankful to JNCASR for financial support and fellowship.

I also take this opportunity to thank all my present and past labmates Dr. Udumula Subbarao, Dr. Sumanta Sarkar, Mr. Soumyabrata Roy, Mr. Rajkumar Jana, Mr. Vidyanshu Mishra, Ms. Shreya Sarkar, Mr. Dundappa Mumbaraddi, Ms. Swetha Ramani, Dr. Vijaykumar S. Marakatti, Mr. Vamseedhara Vemuri, Mr. Pramod Halappa and Dr. Ramesh Siva for their fruitful discussions, help and co-operation for helping me by providing the necessary knowledge base and resources for project completion, presentation and verification.

I take pleasure in thanking summer and project students: Mr. Yatish Khulbe, Ms. Hiranmayee Vadlamani, Mr. Sthitadhi Maiti, Mr. Anupam Bhim, Ms. Vinita Ahuja, Ms. Juhi Dutta, Ms. Shikha Dhiman, Ms. Ekashmi Rathore and Mr. Mahesh Talluri.

My special thanks to the teachers at my school and college (Cotton College, Guwahati) teachers. Last but not the least I thank all my friends, whose words of encouragement and criticism have moulded this report in its present form.

Finally and most importantly, I am grateful to my family, especially my parents and brother for their love, moral support and constant encouragement throughout my life. Their love, blessings and affection have made me what I am today.

Last but not least, I thank Almighty God for providing me this wonderful opportunity.

Saurav

Preface

This dissertation entitled "**Palladium Based Compounds as Efficient and Durable Electrode Materials Towards Electrochemical Energy Production in Fuel Cells"** is focused on the investigation of palladium based nanomaterials as cathode and anode materials for direct ethanol fuel cell (DEFC). Ethanol oxidation reaction (EOR) takes place at the anode and oxygen reduction reaction (ORR) takes place at the cathode of DEFC. Interest in EOR is motivated by low cost and easy availability of the fuel and ORR is motivated by its application in the cathodes of most fuel cells. The slow kinetics and less efficiency of the catalysts are the major barriers to the widespread usage of fuel cells, thus motivating research aimed at increasing understanding of existing electrocatalysts and driving demand for the development of improved electrocatalysts for EOR and ORR.

Chapter 1 deals with the brief overview about basics of fuel cells. This chapter describes various types of fuel cells with special focus on DEFC. A detailed understanding of the anode and cathode materials for DEFC has been discussed. The chemistry of the EOR and ORR are crucial parts of DEFC which have been overviewed. It also discusses about the experimental methods to determine the performance of the catalyst.

Chapter 2 focuses on the search of a stable material that shows considerable activity for EOR. Strategical synthesis methods have been employed for the search of better anode material for DEFC. Comparison of rare-earth (*RE*) based palladium compound RE_xPd_{1-x} (*RE* = Yb, Eu) is made with transition metal based TM_xX_{1-x} (*TM* = Ni, Cr). Detailed electrochemical measurements are carried and *RE* based compounds are found to enhance

the activity of palladium to a larger extent compared to pure palladium and the transition metals substituted ones.

Chapter 3 focuses on the investigation of electrochemical ORR activity of the ternary compound $CoPd_2Se_2$ as cathode material for DEFC. Binary phase of $Pd_{17}Se_{15}$ also exists which have been quantified to be present to as low as 7%. A detailed characterization and electrochemical measurements have been carried out.

Chapter 4 characterizes and investigates the ORR activity of the minor phase present along with $CoPd_2Se_2$ as discussed in Chapter 3. Electrochemical measurements were carried out under the same parameters as discussed in chapter 3. Both $CoPd_2Se_2$ and $Pd_{17}Se_{15}$ were found to have similar ORR activity in terms of onset potential.

This thesis concludes with the list of novel findings of the work done during last one year. Finally, future directions are also provided.

List of Abbreviations

CV	Cyclic Voltammetry
LSV	Linear Sweep Voltammetry
CA	Chronoamperometry
GC	Glassy Carbon
PEMFC	Polymer Electrolyte Membrane Fuel Cell
DEFC	Direct Ethanol Fuel Cell
ECSA	Electrochemically Active Surface Area
RHE	Reversible Hydrogen Electrode
ORR	Oxygen Reduction Reaction
EOR	Ethanol Oxidation Reaction
Hg/HgO	Mercury/Mercury Oxide reference electrode
SEM	Scanning Electron Microscope
TEM	Transmission Electron Microscopy
HRTEM	High Resolution Transmission Electron Microscopy
XRD	X-ray Diffraction
XPS	X-ray Photoelectron Spectroscopy

TABLE OF CONTENTS

Chapter 2. The Role of Rare-Earths in Enhancing Electrocatalytic Activity of Pd Nanoparticles Towards Ethanol Oxidation Reaction

Chapter 1

1. Introduction

1.1. Background

The principle of energy conversion in internal combustion engine (ICE) has not changed much over 200 years. In ICE, the chemical energy is converted to thermal energy i.e. heat, when fuel is burnt in heat engines. This heat generated is then converted to other forms of energy such as mechanical or electrical energy. Due to the over-increasing demand of the electrical energy during the last century, the need for highly efficient combustion engine has become crucial. Furthermore, the scope of renewable energies such as solar, wind, and water is increasing due to the concerns about the pollution of the environment by the conventional energy sources. All of these factors encourage the use of fuel cells, which will play an active and important role in near future.

Fuel cells make use of easily available material as fuel and have low pollutant emission that lists it to be one of a few key next generation resources in automobile industry. A fuel cell uses fundamentals of electrochemistry to produce energy in terms of electricity, with relatively benign water and heat as by products. Fuel cells applications are not only limited to vehicles; they can provide energy for large systems such as utility power stations and other devices as small as a light bulb.

A fuel cell is an energy conversion device that converts fuel to electricity directly yielding some useful by-products. Schematic of a simplified fuel cell is given below:

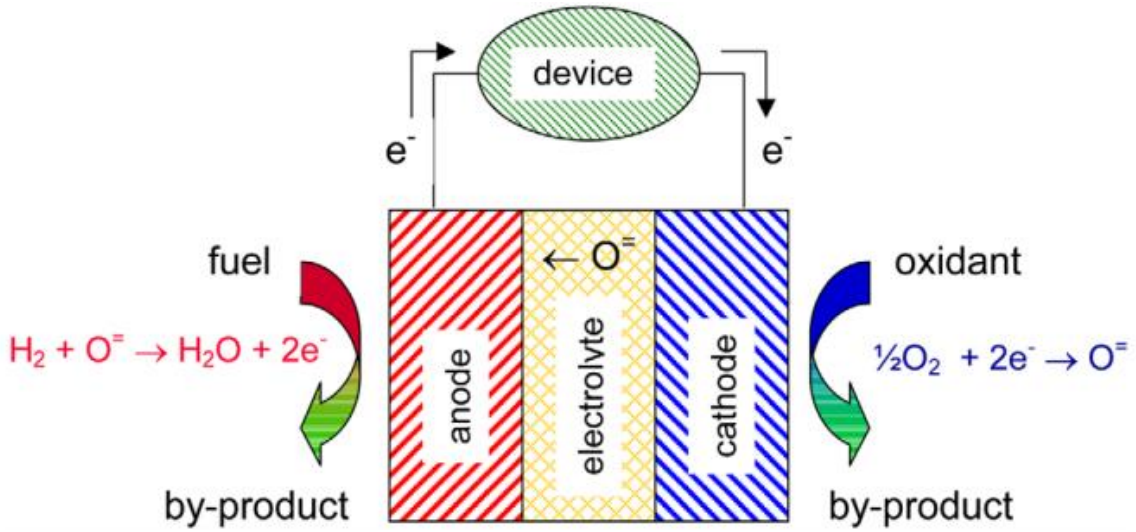

Figure 1.1. Schematic of a fuel cell, comprised of an electrolyte, an anode and a cathode (reprinted with permission from ref [1] ©2003 Elsevier)

In the case of typical H_2/O_2 fuel cell system, hydrogen and oxygen gas (or air) are used as fuels at negative (anode) and positive (cathode) respectively, as described in **Figure 1.1**. It uses a Polymer Electrolyte Membrane (PEM) as an electrolyte. At the anode, hydrogen molecules diffuse through the porous pathway to encounter a catalyst which is generally platinum. At this point, anode catalysts dissociate each hydrogen molecule into two hydrogen atoms which will then be bonded to two-neighbouring Pt atoms. Each of these two hydrogen atoms then release an electron to form two H^+ ions. These H^+ ions are then conducted through the proton exchange membrane while the two electrons pass through the external circuit and reach cathode. On the cathode side, oxygen gets reduced to form water, thus completing the electrochemical reactions.

1.2. Motivation

The work is motivated largely by the Sabatier principle. It states that the interaction between the catalyst and the substrate should be right enough that it is neither too strong nor too weak. If the interaction is too weak then the substrate will fail to bind to the catalyst

and then no reaction will take place. On the other hand, if it is too strong then the catalyst surface will get blocked by the substrate or product.

If Sabatier's principle is the only factor that governs a reaction, a plot of the reaction rate versus the free energy of adsorption of the intermediate results in a volcano curve. Starting from a high, positive (endergonic) energy of adsorption ΔG_{ad}, the rate at first rises with decreasing ΔG_{ad}; this is the ascending branch of the volcano. Near $\Delta G_{ad} \approx 0$ the rate passes through a maximum, and then starts to decrease as ΔG_{ad} becomes more exergonic (descending branch).

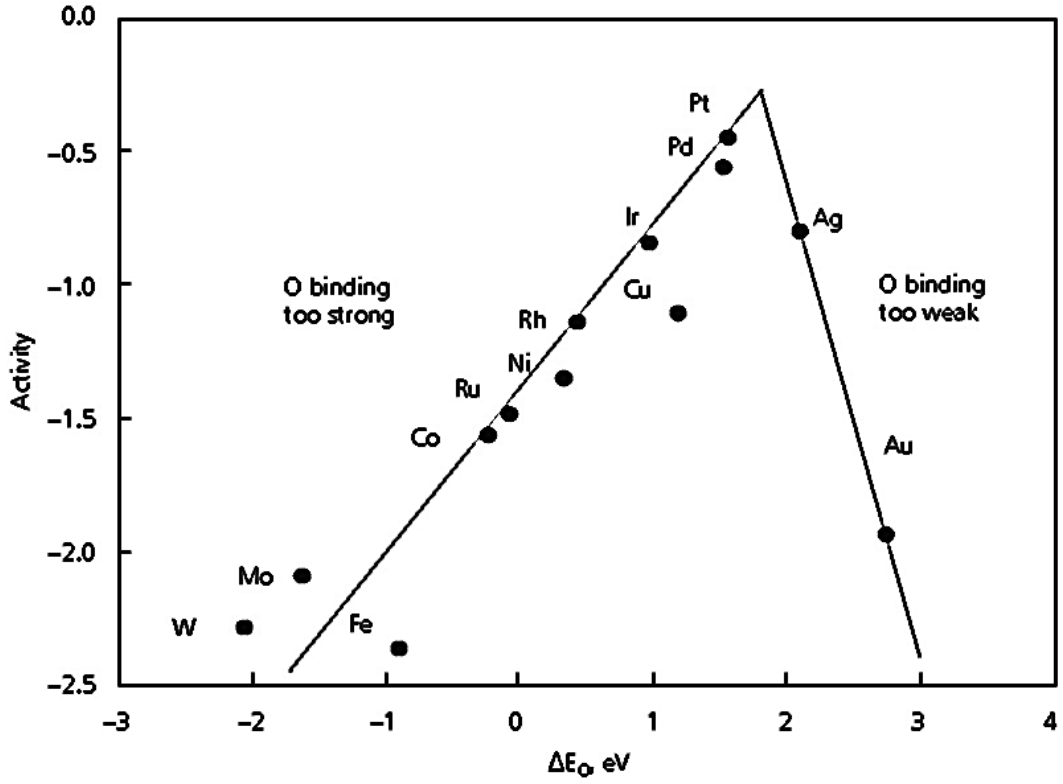

Figure 1.2. Trends in ORR activity as a function of oxygen binding energy.

From the volcano plot in **Figure 1.2** we find that the Pt has the most ideal energy of adsorption and desorption i.e. it binds neither too strongly nor weakly. However, considering the high cost and scarcity of the material, we chose palladium in this work as it has low cost compared to platinum and is about 50 times more abundant than Pt.

1.3. Classification of Fuel Cells

The fuel used by fuel cells is mostly hydrogen but can be hydrogen containing compounds (methanol, ethanol, gas, etc.). This fuel is not burnt thermally but oxidized in an electrochemical reaction, providing direct electrical energy. Based on the type of fuels used in the cell, it is divided generally into six types:

1.3.1. Proton Exchange Membrane Fuel Cell (PEMFC)

The PEMFC employs a polymeric membrane as its electrolyte material. Protons produced by the oxidation of hydrogen, at the anode, are transported to the cathode, where they participate in the reduction of oxygen, with pure water being the only by-product. The cation-conducting polymer (or ionomer) membrane is typically very thin (~ 20 μm) and light, so that PEM fuel cells have very high power densities. The stability of the membrane material governs the operating temperature of the PEMFC. Presently, membranes are typically made from perfluorinated sulfonic acid (PFSA) polymers such as Nafion® or Aquivion. They rely on liquid water to provide their proton conductivity and hence their operational temperature are limited to less than 100 ^{o}C. Precious-metal catalysts are used as electrode material at low temperatures to facilitate electrode reactions. Search for an active membrane material that can operate at high temperature (upto 200 ^{o}C) is an active area of research today. Although precious metal catalysts are still required at these temperatures, they are less prone to poisoning by contaminants, and water management is greatly simplified. The advantages of the PEM fuel cell are its higher power density and quick start up for automotive vehicles. The low operating temperature makes the technology competitive in transportation and commercial applications like laptop computers, bicycle, and mobile phones. There are three types of proton exchange membrane fuel cell- direct ethanol fuel cell (DEFC), direct methanol fuel cell (DMFC) and direct formic acid fuel cell (DFAFC).

a) Direct Ethanol Fuel Cell (DEFC)

Direct ethanol fuel cell is a sub-category of PEMFC in the sense that both of them have similar chemical reactions except the fact that here ethanol is used as a fuel instead of hydrogen. The ethanol fuel can be easily extracted from biomass through fermentation process from renewable energy sources such as sugar cane, wheat, corn or even straw. Here at the anode electrode with the mixture of water, the liquid ethanol is oxidized and generating CO_2, hydrogen ions and electrons. The reaction involved in cathode is same as PEM fuel cell and the generated voltage at its terminal is in the range of 0.5–0.9 V.

b) Direct Methanol Fuel Cell (DMFC)

Methanol can be oxidised by precious metal catalysts and is far easier to store and handle than hydrogen, making it convenient for use as an anode reactant in fuel cells. DMFCs employ polymeric membranes similar to hydrogen-fuelled PEMFCs, although they are usually thicker to limit the crossover of methanol to the cathode, which lowers the efficiency of the cell. Despite the advantages of methanol as a fuel, DMFCs are limited to low-power applications because their power output (and therefore their power density) is limited by the relatively slow reaction kinetics of the methanol oxidation reaction (MOR) compared to hydrogen oxidation. Additionally, the oxidation of methanol produces CO_2 as a by-product, meaning that DMFCs do not share the zero emission credentials of hydrogen-fuelled PEMFCs, and Pt catalysts are effectively poisoned by CO produced as an intermediate in the anode reaction, so CO-tolerant catalysts are necessary.

c) Direct formic acid fuel cell (DFAFC)

Here, formic acid is used as a fuel and continuously fed into the system. DFAFC converts formic acid and oxygen into carbon dioxide and water to produce energy. Storage of formic acid is much easier and safer than that of hydrogen because it does not need to

be done at high pressures and (or) low temperatures, as formic acid is a non-flammable liquid at standard temperature and pressure.

1.3.2. Alkaline Fuel Cell (AFC)

Here, KOH is used as an electrolyte, which limits its operational temperature to below 100 ^{o}C. The electrolyte is also prone to poisoning by CO_2, which means that pure oxygen must be used at the cathode, as opposed to air. Despite this practical limitation and low gravimetric power density [$kW.kg^{-1}$] of the AFC, it has been employed successfully in specialist applications such as spacecraft. It can again be divided into two types - Proton ceramic fuel cell and direct borohydride fuel cell.

1.3.3. Phosphoric Acid Fuel Cell (PAFC)

Here, molten phosphoric acid (H_3PO_4) serves as an electrolyte and has an operational temperature between 150-200 ^{o}C. Pt-based electrocatalysts are required on both electrodes. High operating temperature makes them particularly tolerant to CO poisoning, meaning that reformate hydrogen can be utilised as the anode reactant with minimal purification. However, the high operating temperature and chemically-aggressive electrolyte present a significant challenge towards material stability. Also, slow start-up and low-power density makes the PAFC unsuitable for applications other than large-scale stationary power generation.

1.3.4. Molten Carbonate Fuel Cell (MCFC)

Similar to the PAFC, the MCFC uses a molten sodium or lithium carbonate electrolyte, which requires an operating temperature of around 650 ^{o}C. At such high temperatures, precious metal catalysts can be substituted for inexpensive alternatives such as Raney nickel, and hydrocarbon fuels such as methane or propane become viable for use as anode reactants. However the same durability and start-up issues suffered by the PAFC

also apply to the MCFC, meaning that they are suitable only for large-scale stationary applications

1.3.5. Solid Oxide Fuel Cell (SOFC)

The SOFC has the highest operating temperature of any fuel cell variant, requiring temperatures up to 1000º C for its ceramic electrolyte to conduct O^{2-} ions from cathode to anode. Inexpensive catalysts (typically nickel) can be utilised, as well as hydrocarbon fuels. The extreme operating temperature allows easy recovery of waste heat, so that SOFCs are particularly suitable for combined heat and power (CHP) systems. Early designs employing planar electrodes suffered from issues of slow start-up and poor durability toward thermal cycling, but these problems have been diminished by the advent of tubular and micro-tubular cell geometries. Whilst materials durability remains a significant challenge in the development of SOFCs, commercial products are already beginning to emerge for industrial and residential CHP applications.

Comparison among the different types of fuel cell is listed in **Table 1.1**.

Table 1.1. Characteristics of typical fuel cell systems and applications

Fuel Cell Type	Mobile Ion	Operating Temperature (ºC)	Applications
Alkaline (AFC)	OH^-	20-200	Space Vehicles (e.g. Apollo)
Proton Exchange Membrane (PEMFC)	H^+	30-100	Vehicles and mobile applications
Direct Methanol (DMFC)	H^+	20-90	Portable electronic system of low power
Phosphoric Acid (PAFC)	H^+	200	Large devices utilising high power
Molten Carbonate (MCFC)	CO_3^{2-}	650	Medium to large scale heat and power utilising system
Solid Oxide (SOFC)	O^{2-}	500-1000	Applicable for small and large devices

1.4. I-V characteristic of Fuel Cells

Fuel cell should be able to meet the demand of large electrical energy when large currents are drawn. However, when there is a current load, the cell voltage (V) decreases due to various irreversible processes called 'polarization losses'. Polarization refers to an effect reducing the performance of fuel cell. This effect is a displacement of electrode potential from the equilibrium value. Three different polarization limitations are identified which are described in **Figure 1.2.**

1.4.1. Ohmic Polarization

The ohmic polarization arises due to electrical resistance in the fuel cell components and includes

a) Resistance to the flow of ions in the electrolyte (ionic resistance).
b) Resistance to the flow of electrons and ions in the catalyst layer (ionic and electronic resistance).

It can be expressed as η_{ohm} = I. R, where I is the cell current and R is the overall cell resistance including electronic, ionic and contact resistances.

1.4.2. Activation Polarization

It arises due to the charge transfer reactions occurring taking place at the surface of the electrodes. It is greatly influenced by adsorption/desorption of reactant and/or product species. Also, the transfer of electrons across double layer and nature of electrode surface dictates activation polarization. It can be expressed as

$$\eta_{act} = \left(\frac{RT}{\alpha nF}\right) \ln\left(\frac{i}{i_0}\right)$$

where α is the transfer coefficient and i_0 is the exchange current density.

1.4.3. Concentration Polarization

As current density is increased, there comes a point at which reactants cannot be supplied quickly enough to the active catalytic layers of the electrode to satisfy the current demand. The concentration(s) of reactants at the electrode surface then decrease, causing the electrode potential also to decrease. It arises due to the change in the concentration of the reactants at the surface of the electrodes as the reactants are used up.

It can be expressed as

$$\eta_{\text{conc}} = \left(\frac{RT}{nF}\right) \ln\left(\frac{C_s}{C_{bulk}}\right)$$

where C_s is the concentration at the electrode surface and $C_{bulk}$is the concentration at the bulk of the solution.

1.4.4. Fuel Crossover and Internal Currents

It arises due to unused fuel passing through the electrolyte and stray currents due to electron conduction through electrolyte. In principle, the electrolyte should transport only ions but sometimes, particularly in the case of direct methanol fuel cells, fuel diffusion and electron conduction can result in significant losses.

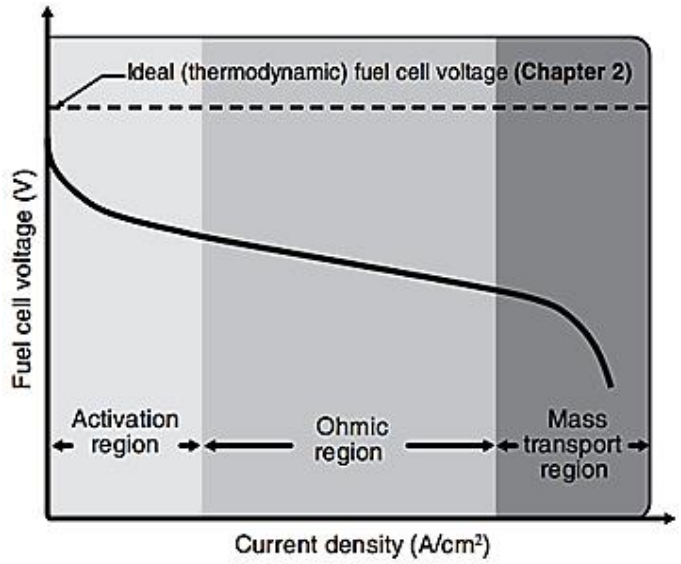

Figure 1.2. Schematic representation of different types of polarization (Figure generated from http://nptel.ac.in/courses/103102015/2)

1.5. Anodic reaction in DEFC

1.5.1. Ethanol Oxidation Reaction (EOR)

As an alternative fuel, ethanol can be produced on a massive scale from biomass feed stocks originating from agriculture (first-generation bioethanol), forestry, and urban residues (second-generation bioethanol), is attracting increasing interest.[2-5] Compared to another common fuel like methanol, ethanol complements the shortcomings of methanol owing to its non-toxicity, higher boiling point, and most importantly, renewability. In addition, ethanol has a high specific energy of 8.01 $kWh \cdot kg^{-1}$, which is comparable to that of gasoline.[6-7] The sluggish kinetics of the EOR presents a major challenge for its development.[8]

1.5.2. Reaction mechanism of EOR

Ethanol electrooxidation involves two types of mechanism. The complete oxidation of ethanol forms CO_2 as the final product but in many cases ethanol is partially oxidised forming unwanted by-products mainly acetaldehyde and acetic acid.[9-13] The product of EOR on Pt/C, PtRu/C and PtSn/C have been proved to be a mixture of acetaldehyde, acetic acid and CO_2.[11, 14-15] Commonly accepted mechanism of ethanol electroxidation in Pt or Pd surfaces is shown below[16-21]

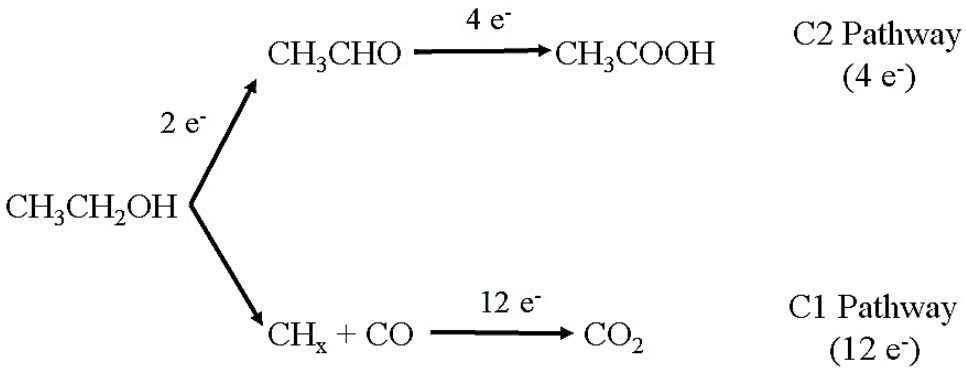

a) C1 Pathway: It proceeds via adsorbed carbon monoxide intermediate to form CO_2.[22]

$$\mathbf{CH_3CH_2OH + 3H_2O \rightarrow 2CO_2 + 12H^+ + 12\ e^-}$$

$$CH_3CH_2OH + 5H_2O \rightarrow 2HCO_3^- + 14\,H^+ + 12\,e^-$$

$$CH_3CH_2OH + 5H_2O \rightarrow 2CO_3^{2-} + 16H^+ + 12\,e^-$$

b) C2 Pathway: C2 pathway mainly leads to the formation of acetic acid (or acetate in alkaline solutions) by delivering four electrons and/or acetaldehyde by delivering two electrons.[22]

$$CH_3CH_2OH + H_2O \rightarrow CH_3COOH + 4H^+ + 4e^-$$

$$CH_3CH_2OH \rightarrow CH_3CHO + 2H^+ + 2e^-$$

Though C1 pathway has high efficiency, C2 pathway is more dominant.[17, 23-24] Products obtained through ethanol oxidation can be analyzed through various techniques such as infrared spectroscopy,[9, 25-29] online differential electrochemical mass spectrometry (DEMS),[29-33] ion chromatography and liquid chromatography.

1.5.3. State-of-the-art material for EOR

Ethanol oxidation has been reported to be very facile on Pt and its alloys such as PtRu,[34] PtSn,[35] PtNi[36] and PtIr.[37] Some of the non Pt based catalysts which have been used for the elctroxidation of ethanol are PdNi,[38] PdAu,[39] PdRu.[40] Pd on various supports such as TiO_2/C, Al_2O_3/C, VO_x/C, CeO_2/C, Co_3O_4/C, MnO_2/C, NiO/C, In_2O_3/C and CNTs.[41-45]

1.6. Cathodic reaction in DEFC

1.6.1. Oxygen Reduction Reaction (ORR)

Although the oxygen reduction reaction (ORR) is important in variety of electrochemical processes and technologies including corrosion (and corrosion inhibition), sensors, and metal-air batteries, the application of the ORR in fuel cells is of particular interest. In a fuel cell, the anode and cathode are separated by an electrolyte that permits the mass-transfer of ions between the electrodes. In contrast to batteries that must be recharged electrically or discarded when their reactants are consumed, reactants are

replenished or continuously supplied in a fuel cell. While a variety of fuels may be used as electron sources at the anode (including hydrogen, methanol, and formic acid etc.) the ubiquity of oxygen in the atmosphere and the large thermodynamic driving force of the oxygen reduction reaction make oxygen the most appealing oxidant for most fuel cell cathodes. The desired reaction is the four electron reduction of oxygen to water, the two electron reduction of oxygen to hydrogen peroxide is less desirable because of the lower efficiency and the generation of corrosive peroxide associated with it.

$$O_2 + 4e^- + 4H^+ \rightleftharpoons 2H_2O \qquad E^0 = 1.23\ V$$

$$O_2 + 2e^- + 2H^+ \rightleftharpoons 2H_2O \qquad E^0 = 0.67\ V$$

Although 1.23 V reduction potential of the ORR provides a substantial thermodynamic driving force the reaction is kinetically slow. The sluggish kinetics of the ORR are typically attributed to the strength of the O=O bond (498 kJ/mol) that must be broken in the course of the reaction. In order to obtain meaningful current densities from the electroreduction of oxygen the kinetics of the ORR must be increased by lowering the activation energy of the reaction. The activation energy is lowered through the use of electrocatalysts and also by reducing the electrode potential. The difference between the electrode potential (E) and the equilibrium potential (Eeq, 1.23 V for the ORR) of the electrode reaction is known as the overpotential, η

$$\eta = E - E\text{eq}$$

1.6.2. Reaction mechanism of ORR

Although there are many reaction pathways involved in the oxygen reduction reaction, there are two overall pathways that can be assumed:

a) Direct 4-electron pathway: It appears predominantly at noble-metal catalysts (e.g. platinum, palladium, silver) and some metal oxides. After the adsorption of O_2, the

molecule divides into adsorbed oxygen atoms; these can then be reduced and protonated to give water.

Alkaline Medium: $O_2 + 2H_2O + 4e^- \rightarrow 4OH^-$ ($E^o = 0.401$ V vs. SHE)

Acidic Medium: $O_2 + 4H^+ + 4e^- \rightarrow 2H_2O$ ($E^o = 1.229$ V vs. SHE)

b) Indirect 2x2 pathway: It has been mostly observed on graphite, carbon, etc. The O_2 molecule does not cleave after the adsorption; instead the peroxide anion (HO_2^-) is formed by partial reduction as an adsorbed intermediate. This intermediate can be further reduced to water or it can be protonated and leave the surface as hydrogen peroxide.

1.6.3. State-of-the-art material for ORR

Pt and Pt alloy nanoparticles show the best activity for ORR.[46-48] Carbon based materials have slo been investigated to show good activity for ORR. Among them carbon nanotubes (CNTs), graphene, non-metal (N, B, P) doped CNTs and graphene are potential candidates for ORR.[49-53] Other non-Pt catalysts include transition metal nitrides such as TiN and MoN, transition metal carbides like W_2C, TiC, transition metal oxides such as MnO_2, Co_3O_4, Cu_2O and transition metal chalcogenides like Rh_xS_y, Ru_xS_y, Rh_xSe_y, Ru_xSe_y, Co_xS_y.[54-57]

1.7. Experimental methods for the evaluation of electrocatalyst performance

1.7.1. Cyclic Voltammetry (CV)

Cyclic voltammetry is the most useful technique in electrochemistry. It can quickly provide qualitative information about catalysts and electrochemical reactions, such as the electrochemical response of catalysts and the catalytic activity of the catalysts with respect to some electrochemical reactions. In a cyclic voltammetry experiment, working electrode

potential is ramped linearly with time. After the set potential is reached, the working electrode potential is ramped in opposite direction to reach the initial potential. **Figure 1.3** shows the schematic representation of a cyclic voltammetry curve. **Figure 1.3a** represents the anodic and the cathodic sweep during an experiment. **Figure 1.3b** represents a typical CV curve as a response from the system.

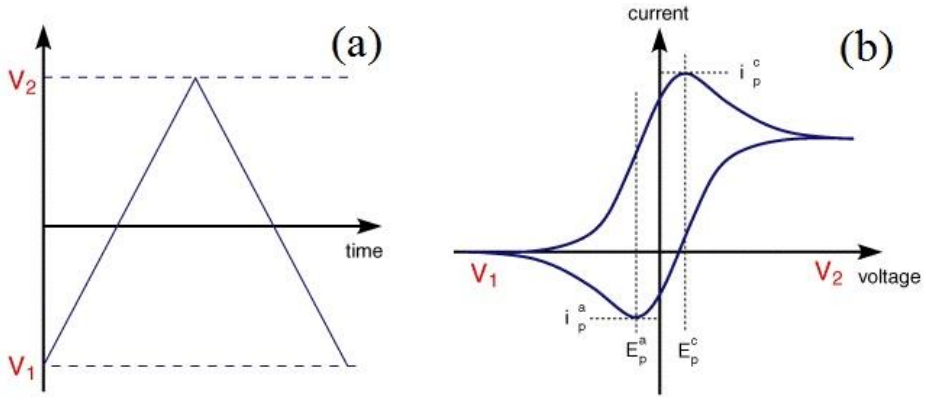

Figure 1.3. Schematic representation of (a) variation of potential with time, (b) CV profile of a catalyst.

1.7.2. Linear Sweep Voltammetry (LSV)

In this technique, working electrode potential is scanned in a particular potential range at a constant rate and the resulting current is measured. The slope of the plot has a unit of volts per unit time and is called the scan rate of the experiment. The faradaic current is found to increase with increase in scan rate. This is due to the increased flux of electroactive material to the electrode at the higher scan rates.

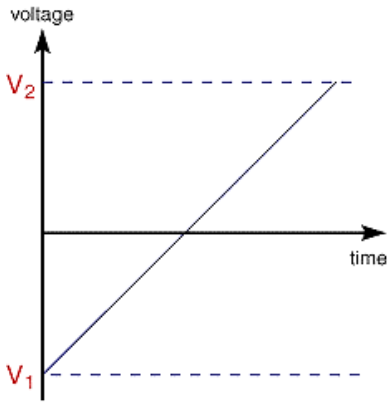

Figure 1.4. Schematic representation showing the variation of potential with time for a linear sweep voltammagram.

1.7.3. Chronoamperometry (CA)

Chronoamperometry (CA), another commonly used electroanalytical technique, is a useful tool for determining diffusion coefficients and for investigating kinetics and mechanisms. At the beginning of the transient experiment the potential of the working electrode is held at E_i. At t = 0 the potential is instantaneously changed to a new value E_1, and corresponding current time response is recorded.

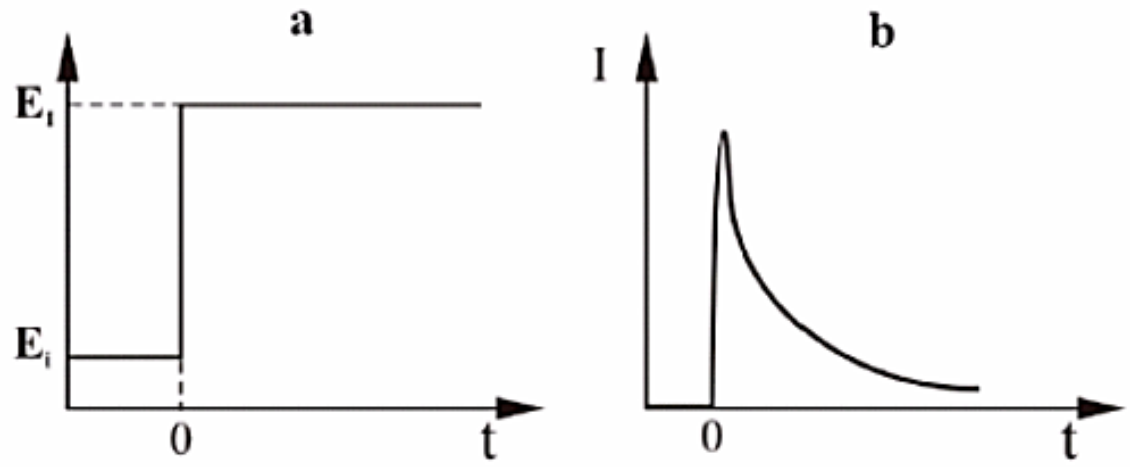

Figure 1.5. Variation of potential and current with time in a chronoamperometric experiment. a) The potential-time profile applied during experiment, E_i is initial value and E_1 is the potential of interest, b) corresponding response of the current due to changes of the potential.

1.7.4. Tafel Plot

The Tafel equation is an equation in electrochemical kinetics relating the rate of an electrochemical reaction to the overpotential. It is a plot of log *i* vs E. The value of the tafel slope helps in the determination of the mechanism of the reaction.

1.7.5. Electrochemically Active Surface Area (ECSA)

The ECSA of an electrode is an important property which must be determined in order to calculate and compare current densities measured for different catalysts and catalyst loadings. The ECSA is a quantitative measure of the active surface area available

for electron transfer. The ratio of the total electrochemically active surface area to the geometric surface area is termed as the roughness factor. Higher the roughness factor, more is the surface area available for the reaction.

1.7.6. Rotating Disk Electrode (RDE)

A rotating disc electrode (RDE) and a rotating ring-disc electrode (RRDE) are employed to detect the intermediates. The ring of the electrode can monitor the amount of hydrogen peroxide formed at the disc. The $2e^-$ and $4e^-$ ORR can occur at the disc and the H_2O_2 is reoxidised to O_2 at the ring. The mechanism of a oxygen reduction reaction in a RDE is shown in **Figure 1.6**.

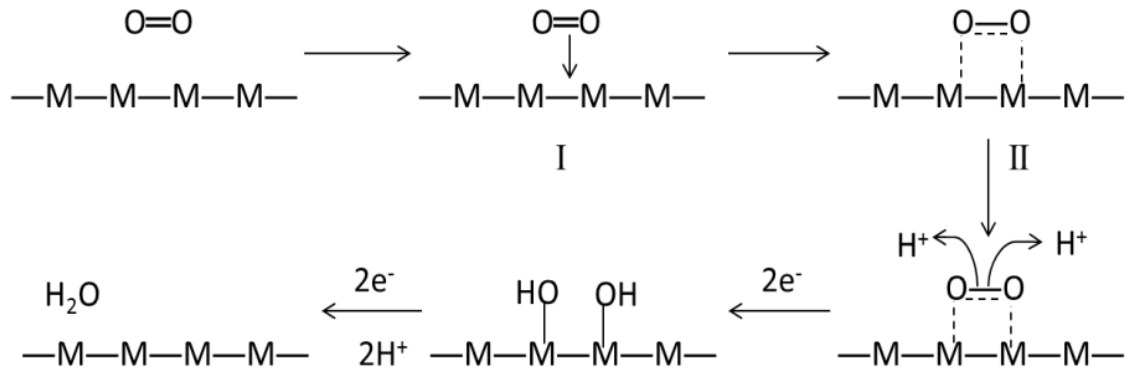

Figure 1.6. Schematic showing the mechanism of oxygen reduction reaction on the surface of a rotating disk electrode.

Considering the low solubility of O_2 of 1.26×10^{-3} mol L^{-1} in aqueous solutions, a forced/convective transport of reactants in the solution is used for studying the kinetics of ORR. Schematic representation of a RDE system is shown in **Figure 1.7**.

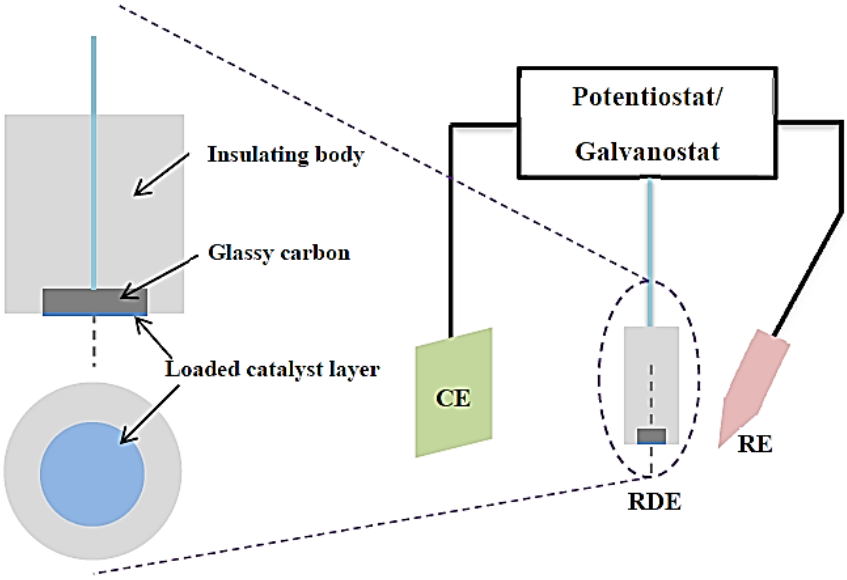

Figure 1.7. Schematic representation of a RDE system.

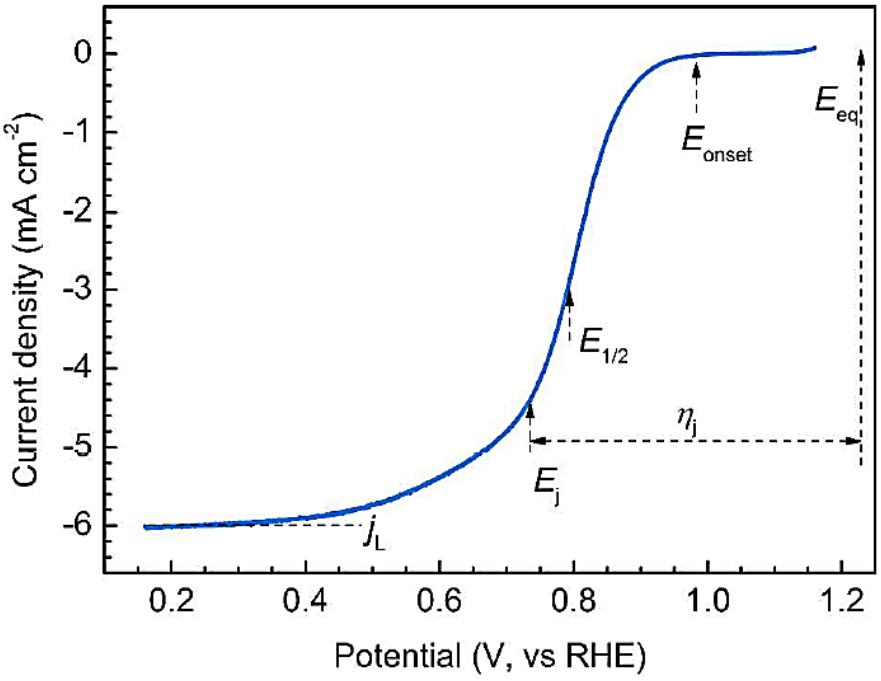

Figure 1.8. LSV plot showing different performance indicators for an oxygen reduction reaction.

An example of a typical RDE polarization curve, with some performance indicators, is shown in **Figure 1.8**. Here, onset potential is represented as Eonset, half-wave

potential is represented as $E_{1/2}$, overpotential under a specific current density is represented as η_j and the diffusion-limiting current density is represented as j_L.

1.7.6.1. Working Principle of RDE

In a rotating disk electrode, a molecule or an ion is being conveyed to the electrode surface and upon arrival it is oxidized or reduced. If a positive bias is applied to the system, the molecule gets oxidized and a negative bias makes it reduced.

Reduction at the rotating electrode implies that electrodes are being added to the molecules or ions from the electrode. A current travelling in this direction is said to be cathodic current and the general form of half-cell reaction taking place is given as:

$$O + ne^- \rightarrow R$$

Oxidation at the electrode surface implies that the electrodes are being removed from the ions or molecules and move to the electrode. A current travelling in this direction is said to be anodic current. A general form of the half-cell reaction taking place in the electrode is given as:

$$R \rightarrow O + ne^-$$

The equilibrium cell reaction is given as:

$$O + ne- \rightleftharpoons R$$

Whenever an observed current is limited only by the rate at which material arrives at the electrode surface, the current is said to be mass transport limited. When working with a rotating electrode, the rate of mass transport is related to the rotation rate of the electrode. Rotating the electrode at a faster rate increases the rate at which material arrives at the electrode surface. Thus, the limiting current increases with increasing rotation rate.

Experiments involving a rotating electrode are designed to purposefully exploit this fundamental relationship between the rotation rate and the limiting current.

1.7.7. Rotating Ring Disk Electrode (RRDE)

The RRDE is a variation on the RDE technique, which allows quantification of peroxide production during ORR. The catalysed disc electrode is surrounded by a concentric Pt ring electrode as shown in **Figure 1.9**. Under rotation, peroxide generated on the disc flows outwards towards the ring, where it is oxidised according to

$$H_2O_2 \rightarrow O_2 + 2H^+ + 2e^- \qquad E^0 = -0.682\ V$$

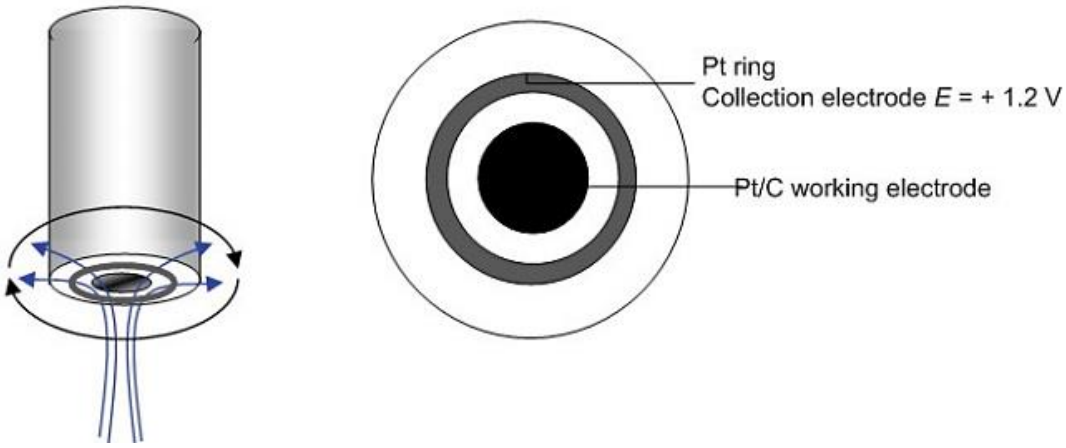

Figure 1.9. Schematic of RRDE assembly and its mass transport characteristics

The potential on the ring is set to around +1.2 V so that the oxidation proceeds under pure diffusion limitation, to ensure that as much peroxide is 'collected' as possible. However, the natural diffusion of peroxide away from the surface of the disc in the direction perpendicular to the disc means that only a fraction of the peroxide is detected. The collection efficiency, N of the RRDE is dependent on its geometry, and can be measured experimentally.

Once the collection efficiency is known, the rate of peroxide formation can be calculated at any potential using

$$\chi_{H2O2} = \frac{2\frac{I_R}{N}}{I_D + \frac{I_R}{N}}$$

where χ_{H2O2} is the number of moles of H_2O_2 formed per mole of O_2, I_R is the ring (collection electrode) current and I_D is the disc (working electrode) current. The rate of peroxide formation is potential-dependent, with Pt/C catalyst typically yielding 5-10 % H_2O_2 at E = 0.1 V.

1.8. General Approach to the Synthesis of Nanoparticles

A large variety of nanoparticles can be synthesized through solution based synthesis method such as solvothermal method, sol-gel method and colloidal synthesis method. For the synthesis of alloys or intermetallic nanoparticles, the precursor salts are dissolved in suitable solvent organic or aqueous solvent.[58] Metal nanoparticles at zero oxidation state are synthesized by the reduction of salts using reducing agent or through controlled decomposition of organometallic compounds. Morphology, size and shape of the particles formed can be tuned by varying parameters such as reaction time, temperature, concentration of reagents and concentration of surfactants.[59-60] Surfactants such as polyvinylpyrrolidone (PVP), sodium dodecyl sulphate (SDS), hexadecyltrimethyl-ammonium bromide (CTAB) are generally used to control the growth and aggregation of nanoparticles.[61-64] Solvent plays a crucial role in the process of synthesis. For instance, polarity of the solvent tunes the interaction between the nanoparticles and the surfactant.[65]

1.9. Objective of the Thesis

With all background discussed above, the main objectives of this thesis have been classified as below.

- Synthesis of low cost Pd-based nanoparticles.

- Study of ethanol oxidation on modified palladium based electrodes by employing conventional electrochemical methods.
- Study of electrochemical oxygen reduction activity to check material's efficiency as cathode materials.
- Study of comparative effect of doping of different elements in Pd compound.
- Special focus is given to chalcogenide and *RE* alloyed Pd as they are least explored.
- Improvement of catalytic activity by designing the promising materials in different sizes and shapes.
- Providing suitable supports to enhance the electrochemical activity towards various electrochemical reactions.
- Comparative studies of the best developed catalysts with the current state-of-the-art materials.

1.10. References

1. Haile, S. M., *Acta Mater.* **2003,** *51* (19), 5981-6000.

2. Xuan, J.; Leung, M. K. H.; Leung, D. Y. C.; Ni, M., *Renew. Sust. Energ. Rev.* **2009,** *13* (6-7), 1301-1313.

3. Wee, J. H., *Renew. Sust. Energ. Rev.* **2007,** *11* (8), 1720-1738.

4. Antolini, E., *J. Power Sources* **2007,** *170* (1), 1-12.

5. Rao, L.; Jiang, Y. X.; Zhang, B. W.; You, L. X.; Li, Z. H.; Sun, S. G., *Prog. Chem.* **2014,** *26* (5), 727-736.

6. Li, M.; Kowal, A.; Sasaki, K.; Marinkovic, N.; Su, D.; Korach, E.; Liu, P.; Adzic, R. R., *Electrochim. Acta* **2010,** *55* (14), 4331-4338.

7. Demirci, U. B., *J. Power Sources* **2007,** *173* (1), 11-18.

8. Yao, L. X.; Chang, Y. H., *Energ. Policy* **2015,** *77*, 131-139.

9. Lai, S. C. S.; Kleijn, S. E. F.; Ozturk, F. T. Z.; Vellinga, V. C. V.; Koning, J.; Rodriguez, P.; Koper, M. T. M., *Catal. Today* **2010,** *154* (1-2), 92-104.

10. Ghumman, A.; Li, G. C.; Bennett, D. V.; Pickup, P. G., *J. Power Sources* **2009,** *194* (1), 286-290.

11. Rousseau, S.; Coutanceau, C.; Lamy, C.; Leger, J. M., *J. Power Sources* **2006,** *158* (1), 18-24.

12. Ghumman, A.; Pickup, P. G., *J. Power Sources* **2008,** *179* (1), 280-285.

13. Sun, S.; Halseid, M. C.; Heinen, M.; Jusys, Z.; Behm, R. J., *J. Power Sources* **2009,** *190* (1), 2-13.

14. Song, S. Q.; Zhou, W. J.; Zhou, Z. H.; Jiang, L. H.; Sun, G. Q.; Xin, Q.; Leontidis, V.; Kontou, S.; Tsiakaras, P., *Int. J. Hydrogen Energ.* **2005,** *30* (9), 995-1001.

15. Wang, Q.; Sun, G. Q.; Jiang, L. H.; Xin, Q.; Sun, S. G.; Jiang, Y. X.; Chen, S. P.; Jusys, Z.; Behm, R. J., *Phys. Chem. Chem. Phys.* **2007,** *9* (21), 2686-2696.

16. Wang, H. F.; Liu, Z. P., *J. Phys. Chem. C* **2007,** *111* (33), 12157-12160.

17. Liang, Z. X.; Zhao, T. S.; Xu, J. B.; Zhu, L. D., *Electrochim. Acta* **2009,** *54* (8), 2203-2208.

18. Lamy, C.; Belgsir, E. M.; Leger, J. M., *J. Appl. Electrochem.* **2001,** *31* (7), 799-809.

19. Zhou, W. J.; Zhou, Z. H.; Song, S. Q.; Li, W. Z.; Sun, G. Q.; Tsiakaras, P.; Xin, Q., *Appl. Catal. B-Environ.* **2003,** *46* (2), 273-285.

20. Lai, S. C. S.; Koper, M. T. M., *Phys. Chem. Chem. Phys.* **2009,** *11* (44), 10446-10456.

21. Camara, G. A.; Iwasita, T., *J. Electroanal. Chem.* **2005,** *578* (2), 315-321.

22. Wang, Y.; Zou, S. Z.; Cai, W. B., *Catalysts* **2015,** *5* (3), 1507-1534.

23. Zhiani, M.; Majidi, S.; Rostami, H.; Taghiabadi, M. M., *Int. J. Hydrogen Energ.* **2015,** *40* (1), 568-576.

24. Buso-Rogero, C.; Herrero, E.; Feliu, J. M., *Chemphyschem* **2014,** *15* (10), 2019-2028.

25. Vigier, F.; Coutanceau, C.; Hahn, F.; Belgsir, E. M.; Lamy, C., *J. Electroanal. Chem.* **2004,** *563* (1), 81-89.

26. Christensen, P. A.; Jones, S. W. M.; Hamnett, A., *J. Phys. Chem. C* **2012,** *116* (46), 24681-24689.

27. Wang, Y.; Jiang, K.; Cai, W. B., *Electrochim. Acta* **2015,** *162*, 100-107.

28. Shao, M. H.; Adzic, R. R., *Electrochim. Acta* **2005,** *50* (12), 2415-2422.

29. Iwasita, T.; Pastor, E., *Electrochim. Acta* **1994,** *39* (4), 531-537.

30. Wang, H.; Jusys, Z.; Behm, R. J., *J. Phys. Chem. B* **2004,** *108* (50), 19413-19424.

31. Wang, H.; Jusys, Z.; Behm, R. J., *Fuel Cells* **2004,** *4* (1-2), 113-125.

32. Wang, H.; Jusys, Z.; Behm, R. J., *J. Power Sources* **2006,** *154* (2), 351-359.

33. Belgsir, E. M.; Bouhier, E.; Yei, H. E.; Kokoh, K. B.; Beden, B.; Huser, H.; Leger, J. M.; Lamy, C., *Electrochim. Acta* **1991,** *36* (7), 1157-1164.

34. Fujiwara, N.; Friedrich, K. A.; Stimming, U., *J. Electroanal. Chem.* **1999,** *472* (2), 120-125.

35. Xu, Z.-F.; Wang, Y., *J. Phys. Chem. C,* **2011,** *115* (42), 20565-20571.

36. D'Villa-Silva, M.; Simões, F. C.; De Souza, R. F.; Da Silva, J. C. M.; Santos, M. C., *ECS Trans.* **2011,** *41* (1), 1299-1306.

37. Lee, Y.-W.; Hwang, E.-T.; Kwak, D.-H.; Park, K.-W., *Catal. Sci. Technol.* **2016,** *6* (2), 569-576.

38. Zhang, Z.; Xin, L.; Sun, K.; Li, W., *Int. J. Hydrogen Energ.* **2011,** *36* (20), 12686-12697.

39. Feng, Y.-Y.; Liu, Z.-H.; Xu, Y.; Wang, P.; Wang, W.-H.; Kong, D.-S., *J. Power Sources* **2013,** *232*, 99-105.

40. Ma, L.; He, H.; Hsu, A.; Chen, R., *J. Power Sources* **2013,** *241*, 696-702.

41. Wang, M.; Guo, D. J.; Li, H. L., *J. Solid State Chem.* **2005,** *178* (6), 1996-2000.

42. Zhang, K. F.; Guo, D. J.; Liu, X.; Li, J.; Li, H. L.; Su, Z. X., *J. Power Sources* **2006,** *162* (2), 1077-1081.

43. Zheng, H. T.; Li, Y. L.; Chen, S. X.; Shen, P. K., *J. Power Sources* **2006,** *163* (1), 371-375.

44. Chu, D. B.; Wang, J.; Wang, S. X.; Zha, L. W.; He, J. G.; Hou, Y. Y.; Yan, Y. X.; Lin, H. S.; Tian, Z. W., *Catal. Commun.* **2009,** *10* (6), 955-958.

45. Sun, Z. P.; Zhang, X. G.; Liu, R. L.; Liang, Y. Y.; Li, H. L., *J. Power Sources* **2008,** *185* (2), 801-806.

46. Wang, C.; Chi, M.; Li, D.; van der Vliet, D.; Wang, G.; Lin, Q.; F. Mitchell, J.; More, K. L.; Markovic, N. M.; Stamenkovic, V. R., *ACS Catal.* **2011,** *1* (10), 1355-1359.

47. Xia, D.; Chen, G.; Wang, Z.; Zhang, J.; Hui, S.; Ghosh, D.; Wang, H., *Chem. Mater.* **2006,** *18* (24), 5746-5749.

48. Chen, C.; Kang, Y.; Huo, Z.; Zhu, Z.; Huang, W.; Xin, H. L.; Snyder, J. D.; Li, D.; Herron, J. A.; Mavrikakis, M.; Chi, M.; More, K. L.; Li, Y.; Markovic, N. M.; Somorjai, G. A.; Yang, P.; Stamenkovic, V. R., *Science* **2014,** *343* (6177), 1339-1343.

49. Yang, L.; Jiang, S.; Zhao, Y.; Zhu, L.; Chen, S.; Wang, X.; Wu, Q.; Ma, J.; Ma, Y.; Hu, Z., *Angew. Chem. Int. Ed.* **2011,** *50* (31), 7132-7135.

50. Wang, S.; Yu, D.; Dai, L.; Chang, D. W.; Baek, J.-B., *ACS Nano* **2011,** *5* (8), 6202-6209.

51. Yang, Z.; Yao, Z.; Li, G.; Fang, G.; Nie, H.; Liu, Z.; Zhou, X.; Chen, X. a.; Huang, S., *ACS Nano* **2012,** *6* (1), 205-211.

52. Liang, J.; Jiao, Y.; Jaroniec, M.; Qiao, S. Z., *Angew. Chem. Int. Ed.* **2012,** *51* (46), 11496-11500.

53. Wang, S.; Yu, D.; Dai, L., *J. Am. Chem. Soc.* **2011,** *133* (14), 5182-5185.

54. Liang, Y.; Li, Y.; Wang, H.; Zhou, J.; Wang, J.; Regier, T.; Dai, H., *Nat. Mater.* **2011,** *10* (10), 780-786.

55. Ziegelbauer, J. M.; Gatewood, D.; Gullá, A. F.; Guinel, M. J. F.; Ernst, F.; Ramaker, D. E.; Mukerjee, S., *J. Phys. Chem. C* **2009,** *113* (17), 6955-6968.

56. Xu, J.; Gao, P.; Zhao, T. S., *Energ. Environ. Sci.* **2012,** *5* (1), 5333-5339.

57. Cheng, F.; Shen, J.; Peng, B.; Pan, Y.; Tao, Z.; Chen, J., *Nat. Chem.* **2011,** *3* (1), 79-84.

58. Huang, P.; Lin, J.; Li, Z.; Hu, H.; Wang, K.; Gao, G.; He, R.; Cui, D., *Chem. Commun.* **2010,** *46* (26), 4800-4802.

59. Yang, C.; Xiao, F.; Wang, J.; Su, X., *J. Colloid Interf. Sci.* **2014,** *435*, 34-42.

60. Swami, A.; Kumar, A.; D'Costa, M.; Pasricha, R.; Sastry, M., *J. Mater. Chem.* **2004,** *14* (17), 2696-2702.

61. Naskar, M. K.; Patra, A.; Chatterjee, M., *J. Colloid Interf. Sci.* **2006,** *297* (1), 271-275.

62. Kumar, S.; Gradzielski, M.; Mehta, S. K., *RSC Adv.* **2013,** *3* (8), 2662-2676.

63. Singh, L. P.; Bhattacharyya, S. K.; Mishra, G.; Ahalawat, S., *Appl. Nanosci.* **2011,** *1* (3), 117-122.

64. Bao, Y. P.; An, W.; Turner, C. H.; Krishnan, K. M., *Langmuir* **2010,** *26* (1), 478-483.

65. Gacem, N.; Diao, P., *Colloids and Surfaces A: Physicochem. Eng. Asp.* **2013,** *417*, 32-38.

Chapter 2

2. The Role of Rare-Earths in Enhancing Electrocatalytic Activity of Pd Nanoparticles towards Ethanol Oxidation Reaction

2.1. Introduction

Both direct methanol fuel cells (DMFCs) and direct ethanol fuel cells (DEFCs) have been projected to be strong candidates to compete with advanced batteries for powering mobile and portable electronic devices owing to their uniquely high specific energy.[1] However, the use of DEFC is more prevalent than DMFC due to the toxicity of methanol. Moreover, ethanol has a volume energy capacity of 6.3 kWh/L, which is higher than hydrogen (2.6 kWh/L) and methanol (4.8 kWh/L).[2] The most significant advantage associated with the change in the electrolyte membrane from acid to base is that the kinetic reaction of both the alcohol anodic oxidation and the oxygen cathodic reduction in alkaline media become faster than in acidic media, thus making it possible to reduce the catalyst loading.[3-5]

Pure platinum on carbon is considered as the current state-of-the-art material, but is prone to CO poisoning generated during EOR. So elements such as Ru,[6-10] Sn,[6-7, 11] Pb,[12-14] Bi,[15-18] Re,[19] Sb,[18] Ir,[20] Au,[21] Ce,[22] Rh,[23] Pd,[24-26] Fe,[27] Ni,[21, 28] P,[29] Mo[10, 30] have been widely employed to enhance the activity of platinum and prevent CO poisoning.

However, due to the scarcity and high price of Pt-based catalysts, it is not a good choice for long-term commercialization.

In this regard, palladium based catalysts, which are less costly, more abundant and have facile EOR kinetics, can be considered as the alternative to Pt based compounds. Pd in alkaline medium have higher CO tolerance compared to Pt in acidic medium.[31] This has led researchers to alloy palladium with various transition elements to increase the electrochemical activity towards the oxidation of small organic molecules (SOMO). Elements such as Ni,[1-2] Ag,[32] Au,[33-35] P,[36] Co,[37] Sn,[38-40] Ru,[41] Zn[42] are alloyed with Pd for different electrocalaysis reactions such as SOMO, HER and ORR.

In this context it is worth to mention that the role of rare earth (*RE*) in improving the catalytic activity of Pd or Pt has not been explored much. Few examples of *RE* based materials are binary alloys of nickel and samarium or dysprosium used for direct borohydride fuel-cell[43] and Co-Ni-*RE* and Fe-*RE* based crystalline alloys used as electrode materials for hydrogen evolution reaction in alkaline medium.[44]

In this work, the role of *RE* doping in enhancing the activity of Pd nanoparticles, towards electroxidation of ethanol is studied. Among the *RE*s, Yb and Eu have special interest to our motivation due to their ability to exist in two energetically similar electronic configurations: the magnetic Yb^{3+} ($4f^{13}$) and the nonmagnetic Yb^{2+} ($4f^{14}$). Because of the close proximity in terms of energy, Yb based compounds, in many occasions, show mixed valent/intermediate valent states.[45-49] Because of this, Yb based compounds have also the ability to exhibit various unique properties. The reactivity of an atom apparently depends on the oxidation state and size of the ion. Since Yb has the ability to exist in two different oxidation states, their reactivity should also be different. The valence transition of Yb is energetically favorable, but Yb^{2+} is a more stable valence

state in comparison to Yb^{3+} because of substantial decrease in strain and higher exchange coupling interaction in Yb^{2+}.[46] However, the non-magnetic Yb^{2+} has ionic radius of 194 pm,[50-51] which is larger than the magnetic Yb^{3+} with an ionic radius, 174 pm.[51] Due to the large size, the reactivity of Yb^{2+} is expected to be more than Yb^{3+} therefore the compounds with Yb^{2+} are expected to react more with oxygen compared to the trivalent compounds. In similar line, Eu based compounds also deserve scientific interest as they can also exhibit two energetically similar electronic configurations; the nonmagnetic Eu^{3+} ($4f^6$) and the magnetic Eu^{2+} ($4f^7$).

Finally, it should be mentioned that the name "Rare Earths" could be misleading us. For instance, the most abundant *RE* element, Ce, is approximately equally abundant in the earth's crust as other elements used for everyday applications, such as copper (Cu), and is more abundant than boron (B), lead (Pb) or tin (Sn). Even the rarest of the *RE*s, thulium (Tm) is more abundant than Cd, Au and Pt. Although many of the *RE* elements are more abundant than common metals such as Pb or Cd, one of the main problems concerning *RE* elements is their extraction from minerals. In fact they are extracted in minerals all together, that is, all the light *RE*s, from lanthanum (La) to Sm are extracted from minerals such as monazite, and the heavy *RE*s, starting from gadolinium (Gd) are extracted from minerals such as xenotime. Since they have similar sizes, so their separation is difficult as they have the same chemical properties. Generally, only separation based on the difference in their physical properties can be used, for instance the ion-exchange method. For these reasons, the prices of *RE* elements are generally higher than, for instance, that of Pb.

Based on above motivation, in this work, we have focused our research in doping Pd with Yb or Eu to form RE_xPd_{1-x} ($0.08<x<0.15$) and study the activity of the substituted Pd alloys towards ethanol electroxidation. The alloys are synthesized using

solvothermal approach and TEG as solvent. The synthesized nanoparticles are characterized by powder X-ray diffraction (PXRD), energy dispersive X-ray (EDAX), X-ray absorption near edge spectroscopy (XANES) and transmission electron microscopy (TEM). Further we have also compared the electrochemical properties of the synthesized *RE* based alloys with that of transition metal (Ni and Cr) based alloys. However, *RE*s are found to enhance the activity of palladium to a much greater extent compared to that of the transition metals.

2.2. Experimental Section

2.2.1. Synthesis

2.2.1.1. Chemicals

The following materials were used for the synthesis: Ytterbium chloride ($YbCl_3$) (99.99%), europium chloride ($EuCl_3$) (99.99%) were purchased from Sigma Aldrich. Potassiumhexachloroplatinate (II) (K_2PtCl_6) (99.9%) was purchased from Merck. Potassiumtetrachloropalladate (II) (K_2PdCl_4) (99.99%), ethylene glycol (EG) (99+%), and tetraethylene glycol (TEG) were purchased from Alfa Aesar. Sodium borohydride ($NaBH_4$) (98%, Sigma Aldrich) was used as the reducing agent in all the solution phase reactions. All air sensitive chemicals were handled inside the glove box.

2.2.1.2. Solvothermal Method

In a typical synthesis, $YbCl_3$ (0.1 mmol, 27.9 mg), $EuCl_3$ (0.1 mmol, 25.8 mg). K_2PtCl_4 (0.3 mmol, 124.52 mg) and K_2PdCl_4 (0.3 mmol, 97.92 mg) were weighed in appropriate quantity in order to prepare the following alloy RE_xPd_{1-x} (*RE*= Yb, Eu) where $0.08<x<0.15$. A small amount (~1-2 ml) of EG was added after the addition of precursors to prevent the hydrolysis of these salts. After the addition of the precursors, $NaBH_4$ was added to reduce the Pd salts to their corresponding zero oxidation state. The autoclaves were then filled with solvent ethylene glycol approximately 18-20 ml (80%) to form the

reaction solution. The addition of $NaBH_4$ to the suspension produced a black colour, which was caused by the reduction of Pd^{2+} ions to metallic Pd. The chambers were then tightened and the contents were properly mixed using orbital shaker. The autoclaves were then placed in an oven for 24 hours at a temperature of 220 °C. After the completion of 24 h, the autoclaves were taken out and the solutions from the autoclaves were transferred to the respective centrifuge tubes. All the centrifuge tubes were labelled with the respective compounds. Before centrifuging, the solution in the centrifuge tubes was mixed thoroughly using the vortex and sonicator. The catalysts obtained were then washed with ethanol. The mixture was centrifuged at 5000 rpm for 5 min after each washing cycle and the supernatant solution was removed. The same procedure was repeated for 5 times so as to remove all the other organic solvents from the mixture and the compound was washed thoroughly. After the last wash cycle the particles were dried using vacuum oven at 60 ^oC. The dried compounds were then used for further characterizations.

The same strategy was extended to synthesize TM_xPd_{1-x} (*TM* = Ni, Cr) maintaining the same value of $0.08<x<0.15$.

2.2.1.3. Ceramic Method

In order to obtain ordered nanoparticles, the samples were annealed by using ceramic method. The *RE* substituted Pd obtained from the solvothermal method was transferred in a 9 mm fused silica tube which was flame sealed under a vacuum of 10^{-3} torr, to prevent oxidation during heating. The reactants were then heated to 800 °C through 10 h, maintained at that temperature for 5 h to allow proper homogenization, then cooled to 600 °C in 2 h and kept at this temperature for 24 h. Finally, the sample was allowed to naturally cool down to room temperature.

2.3. Characterization

2.3.1. Powder X-ray Diffraction (PXRD)

Phase identity and purity of the RE_xPd_{1-x} (*RE*= Eu and Yb) nanoparticles and related compounds were determined by powder XRD measurements that were carried out with a Bruker D8 Discover diffractometer using Cu-*K*α radiation (λ = 1.5406 Å) over the angular range $20^{\circ} \leq 2\theta \leq 80^{\circ}$ at room temperature calibrated against corundum standard. The experimental powder XRD patterns of the above compounds were then matched with that of simulated one obtained from Pearson Crystal Database (PCD).

2.3.2. Transmission Electron Microscopy (TEM)

TEM images and selected area electron diffraction (SAED) patterns were collected using a Tecnai and JEOL 200 kV TEM. TEM samples were prepared by first sonication of the nano-crystalline powders in ethanol solution and then drop cast onto a holey carbon grid.

2.3.3 Electrochemical Studies

All the electrochemical measurements were performed on a CHI 760E electrochemical workstation with three electrode channels at room temperature. Three electrodes set-up consists of a glassy carbon (GC) (having diameter 3 mm) as working electrode, platinum wire as counter electrode and Hg/HgO (MMO) as the reference electrode. The solution was purged with nitrogen gas for 35 min prior to the measurement. The catalyst ink was prepared by dispersing 1 mg of catalyst in 200 μL of mixed solvent solution (IPA:H_2O = 1:3 v/v). From the prepared catalyst ink 5 μL was dropcasted on GC electrode and dried under table lamp for 20 min. Then 5 μL of nafion binder (0.05 wt%) was added to the catalyst-modified GC electrode. Before depositing the catalyst, the GC electrode was sequentially polished with 1, 0.3 and 0.05 μm alumina slurry, and washed several times with distilled water. Commercial Pd/C (20 wt%, Sigma

Aldrich) was used for comparison of activity. Cyclic voltammetry (CV) measurement was carried out with 0.5 M KOH aqueous solution as well as 0.5 M KOH + 1M EtOH electrolyte solution at a scan rate 50 mV/sec. Chronoamperometry (CA) measurements were performed in 0.5M KOH+1M EtOH electrolyte solution for 1000 sec.

2.3.4 X-ray Absorption Near Edge Spectroscopy (XANES)

Room temperature XANES experiments on RE_xPd_{1-x} were performed at PETRA III, P06 beamline of DESY, Germany. Measurements at the Eu L_{III} and Yb L_{III} edges and at ambient pressure were performed in transmission mode using gas ionization chambers to monitor the incident and transmitted X-ray intensities. Monochromatic X-rays were obtained using a Si (111) double crystal monochromator which was calibrated by defining the inflection point (first derivative maxima) of Cu foil as 8980.5 eV. The beam was focused employing a Kirkpatrick–Baez (K–B) mirror optic. A rhodium coated X-ray mirror was used to suppress higher order harmonics. A CCD detector was used to record the transmitted signals. The sample was prepared by mixing an appropriate amount of finely ground sample powder with cellulose and cold pressing them to a pellet.

2.4. Result and Discussions

2.4.1. Structure and PXRD Analysis

The compounds RE_xPd_{1-x} (*RE* = Eu and Yb) in nano dimension were synthesized using solvothermal method. The crystal structures of the REX_3 (*RE* = La-Nd, Sm-Er, Yb and Lu) intermetallic compounds have been determined by Harris and Raynor.[52-53] They found that the compounds crystallize in the Cu_3Au structure type with the space group of $Pm\bar{3}m$. Although we have targeted for the ordered $REPd_3$, the synthesis resulted in disordered compounds $RE_xPd_{1-x.}$ The comparison between the crystal structures of *RE*

substituted Pd (with the space group of $Fm\bar{3}m$) and ordered REX_3 compounds (with the space group of $Pm\bar{3}m$) is shown in **Figure 2.1**. In the case of RE_xPd_{1-x} crystal structure, the *RE* and transition metal (*TM*) together share a corner as well face center and end up in the space group of $Fm\bar{3}m$, but in the case of ordered crystal structure both *RE* and *TM* have independent crystallographic site (**Figure 2.1).**

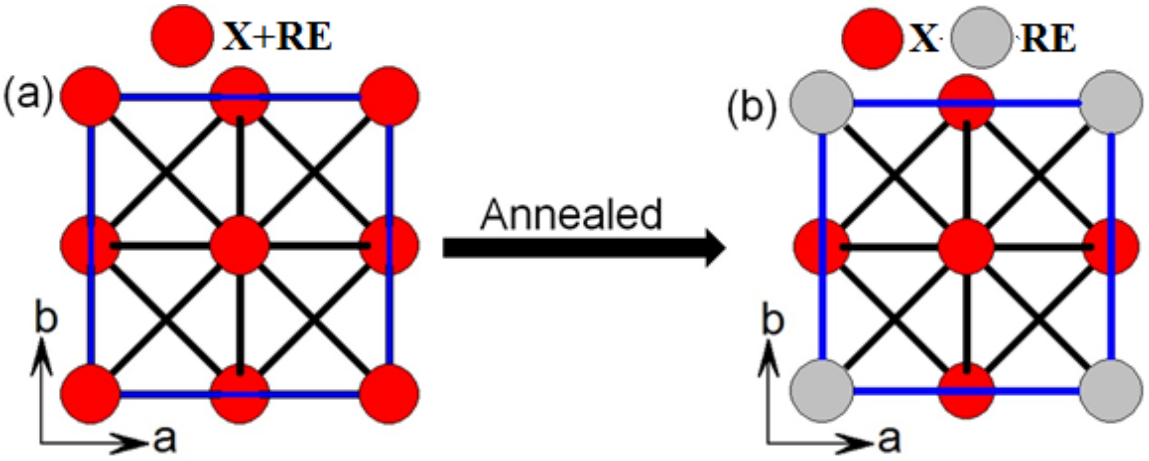

Figure 2.1. Crystal structure of (a) disordered RE_xPd_{1-x} (*RE* = Eu and Yb) and (b) ordered $REPd_3$ (*RE* = Eu and Yb). Unit cell is out lined as blue solid lines.

The PXRD data (**Figure 2.2**) of the samples RE_xPd_{1-x}, synthesized by solvothermal processes, confirmed the formation of disordered phases. Figure 2a-d shows the combined experimental PXRD patterns of Eu_xPd_{1-x} and Yb_xPd_{1-x} disordered phases and simulated ordered patterns of the respective compounds. The XRD pattern of ordered simulated $REPd_3$ shows eleven peaks at 22.186°, 31.27°, 38.81°, 45.02°, 50.78°, 55.66°, 65.63°, 69.85°, 74.50°, 78.49°, 83.14° in the range of $20^o<2\theta(\text{degree})<80^o$ respectively consistent with the (100), (110), (111), (200), (210), (211), (220), (311) and (322) reflections of the ordered $REPd_3$ structure. For the disordered simulated $Yb_{0.08}Pd_{0.92}$ sample PXRD pattern shows only five main characteristic peaks (111), (200), (220), (311) and (322), which are matching with the ordered as well our synthesized RE_xPd_{1-x}.

This is also another confirmation that our compounds RE_xPd_{1-x} were formed in disordered phase.

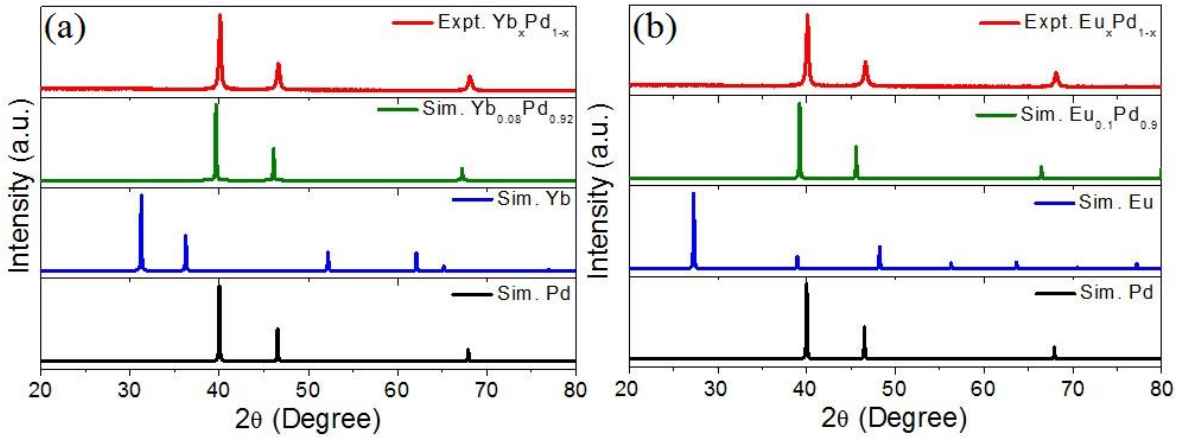

Figure 2.2. PXRD comparison between simulated and experimental for the compounds (a) Yb_xPd_{1-x} and (b) Eu_xPd_{1-x} synthesized by solvothermal method.

The products obtained have disordered structure as can be seen from the PXRD pattern. To convert the products from the disordered to the ordered composition usually thermal annealing is required.[54] So, all the obtained samples were exposed to thermal annealing. Eu_xPd_{1-x} was annealed at 600 °C and Yb_xPd_{1-x} at 800 °C (**Figure 2.3a,b**). **Figure 2.3** shows the comparison of the PXRD plots of the RE_xPd_{1-x} annealed sample with their simulated pattern. It has been found that even after annealing at high temperature the phases remain disordered.

Then Yb based samples were annealed at 800 °C, which resulted in the formation of impurity phase $YbO_{1.5}$ in addition to Yb_xPd_{1-x} (**Figure 2.3a**). It is well known that *RE* can easily form oxides in presence of even small amount of oxygen. From this comparison it can be concluded that the PXRD plots of annealed Yb_xPd_{1-x} sample and the $YbO_{1.5}$ simulated pattern are quite similar. For instance, peaks at 30.21°, 35.08°, 50.50°, 59.88°, 63.01° and 82.14° for the annealed sample matches well with that of $YbO_{1.5}$ phase. It means that there might have been some unreacted metallic Yb present in the sample that may got oxidized by atmospheric oxygen

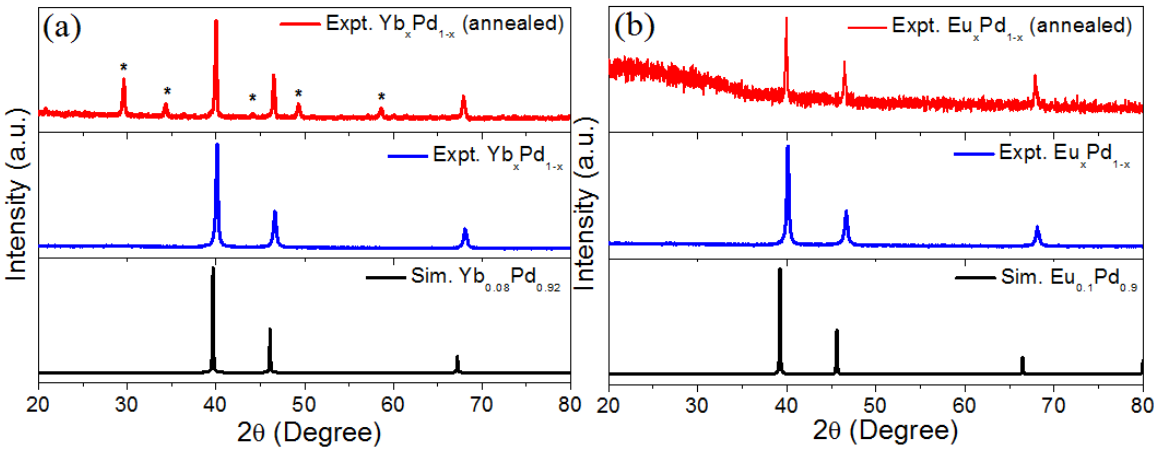

Figure 2.3. (a,b) PXRD comparison of simulated and experimental of RE_xPd_{1-x} (*RE* = Yb and Eu) samples with annealed samples (a, b @ 600 ^{0}C and c, d @ 800 ^{0}C). (*Represents $YbO_{1.5}$ peaks).

As mentioned previously, transition metal analogues of RE_xPd_{1-x} have been synthesized to study their doping effect on the electrocatalytic activity of Pd. TM_xPd_{1-x} (*TM* = Ni, Cr) were synthesized for this comparison study. The simulated and experimental PXRD patterns of the samples are shown in **Figure 2.4**.

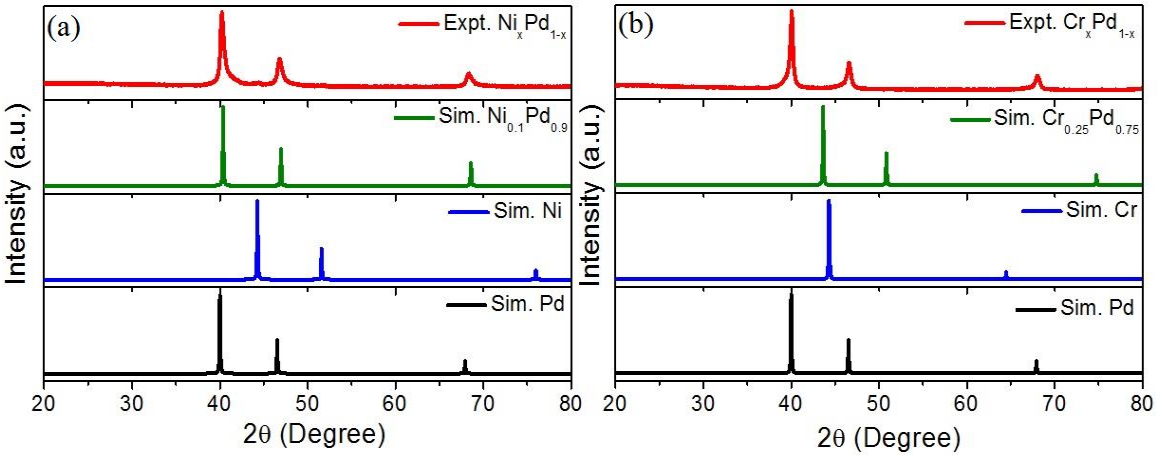

Figure 2.4. PXRD comparison of simulated and experimental PXRD pattern of (a) Ni_xPd_{1-x} and (b) Cr_xPd_{1-x} samples.

2.4.2. TEM Analysis

The TEM images of the synthesized nanoparticles give a lot of insight into the morphology of the particles and their size. **Figure 2.5a** shows the TEM image of Eu_xPd_{1-x} in which we can visualize aggregated particles. Concentric rings in the SAED pattern in

Figure 2.5b represents (111), (200), (220), (311) and (222) planes. Interplanar distance, as calculated from the HRTEM image in **Figure 2.5c**, is found to be 0.226 nm, which corresponds to (111) plane of the crystal structure.

Figure 2.5d shows the TEM image of Yb_xPd_{1-x}, which again displays that the particles have got aggregated. The size of the particles in this case can be determined and is less than 10 nm. The compounds synthesized in this work are found to be polycrystalline in nature as can be clearly visualized from the SAED images of these compounds in **Figure 2.5e**. In these SAED images, several concentric circles are easily visible which prove that the sample is polycrystalline in nature.

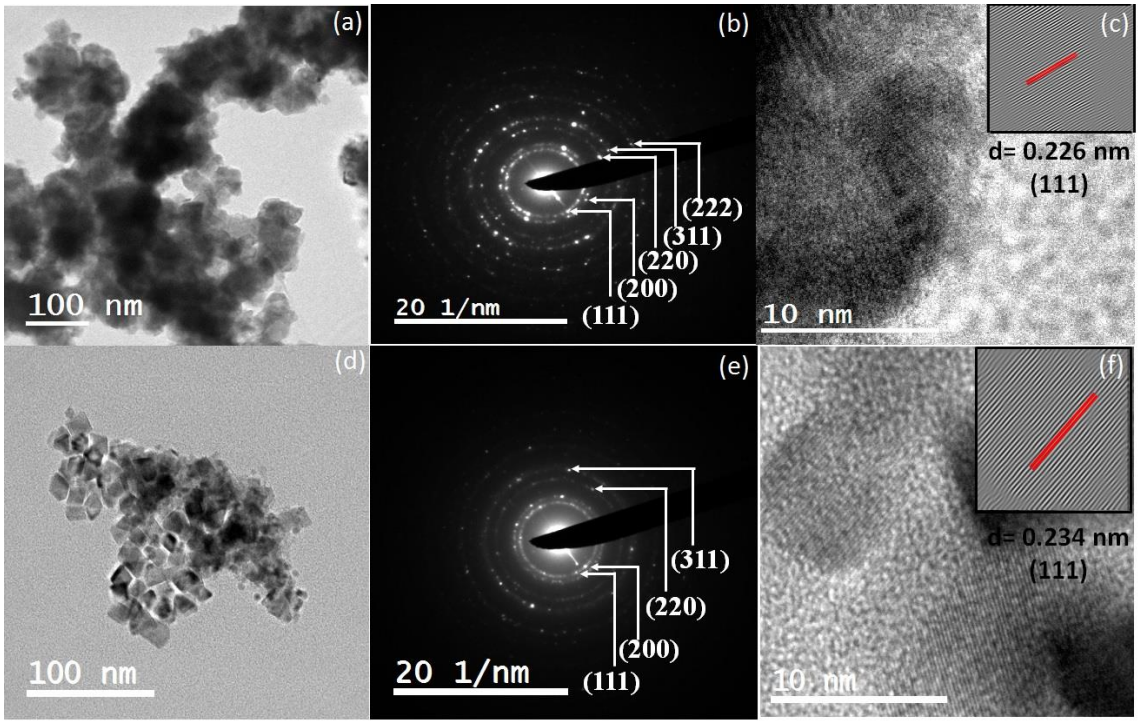

Figure 2.5. TEM images of (a) Eu_xPd_{1-x} and (d) Yb_xPd_{1-x}. Corresponding SAED pattern of (b) Eu_xPd_{1-x} and (e) Yb_xPd_{1-x}. HRTEM images of (c) Eu_xPd_{1-x} and (f) Yb_xPd_{1-x}. Inset figure in c and f corresponds to the inverse FFT image for the calculation of d-spacing.

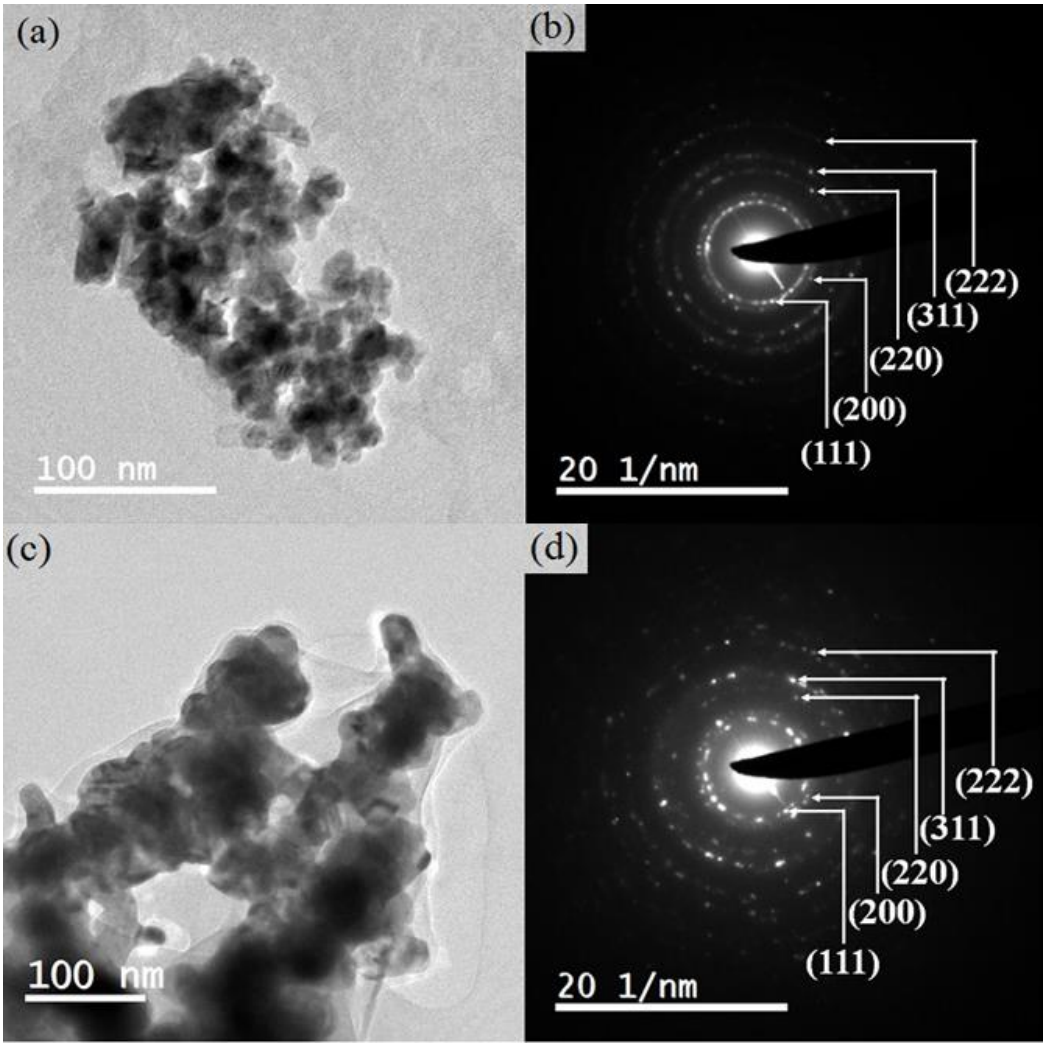

Figure 2.6. TEM images of (a) Cr_xPd_{1-x} and (c) Ni_xPd_{1-x} show that the particles are aggregated. Corresponding SAED pattern of (b) Cr_xPd_{1-x} and (d) Ni_xPd_{1-x} explains the polycrystalline nature of the samples.

2.4.3. FESEM-EDAX Analysis

FESEM images of the particles shows the highly aggregated nature of the system (**Figure 2.7**). EDX spectra of the as-prepared sample are shown in **Figure 2.8**. The EDX from the FESEM analysis clearly confirms the presence of respective elements in the Yb_xPd_{1-x} and Eu_xPd_{1-x} nanoparticles. In the EDAX spectra, peaks are observed at 1.5 keV and 2.8 keV for Yb and Pd respectively and 5.8 keV, 1.1 keV and 2.8 keV for Eu and Pd respectively. The absence of other elements indicates that the prepared nanoparticles have a high purity level.

` From the EDAX elemental analysis in **Figure 2.8a**, the atomic percentage of Yb and Pd are found to be 7.43±1.7 % and 92.57±0.79 %, respectively, which suggests an stoichiometric ratio of 0.92:0.08 for the compound Yb_xPd_{1-x}. A similar stoichiometry of 0.88:0.12 is observed, as seen from **Figure 2.8b**, for the compound Eu_xPd_{1-x}.

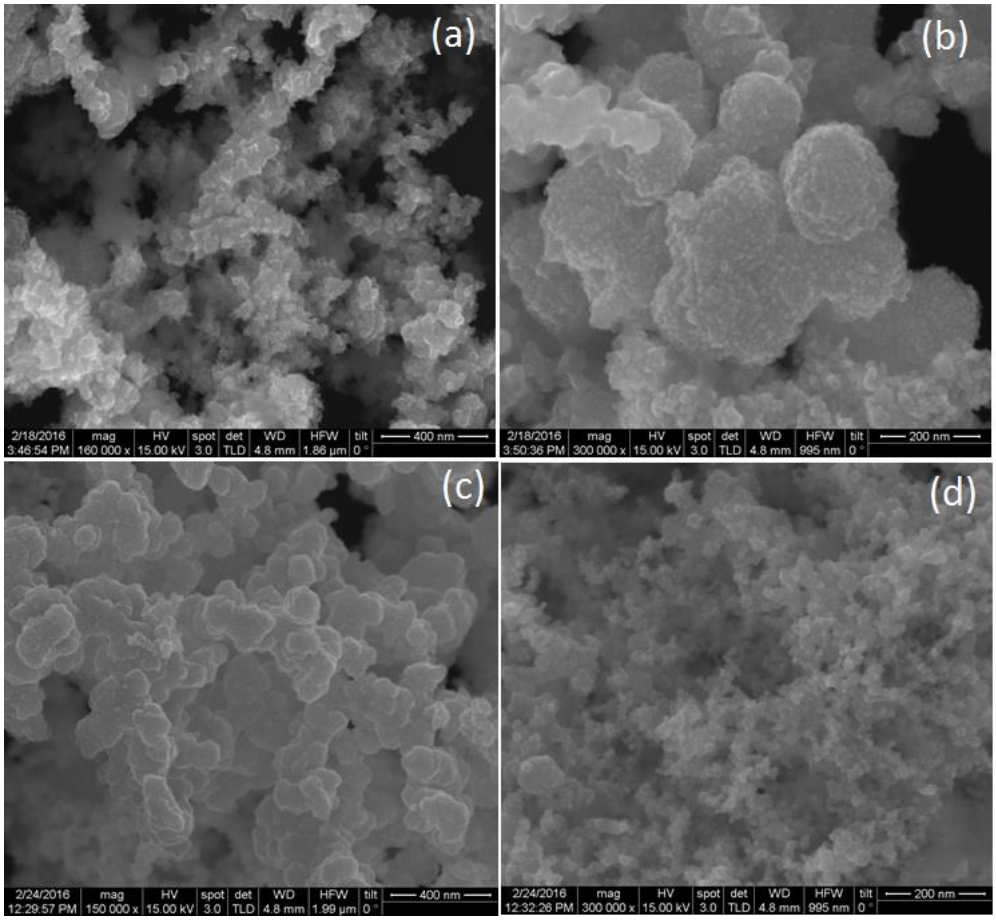

Figure 2.7. FESEM images of (a,b) Yb_xPd_{1-x} and (c,d) Eu_xPd_{1-x} nanoparticles.

2.4.4. XANES Analysis

To confirm the oxidation state of europium and ytterbium in RE_xPd_{1-x} compounds, we have performed the XANES measurements at the Eu L_{III}-edge and Yb L_{III}-edge, at 300 K and ambient pressure (**Figure 2.9**). This is a strong experimental tool in order to firmly establish the valence state of an element in a compound. The spectra shows only one absorption peak centered at 6983 eV and 8952 eV, respectively for for Eu_xPd_{1-x} and Yb_xPd_{1-x} (**Figure 2.9a,b**). It can be attributed to trivalent Eu and Yb atoms

and clearly confirms the absence of divalent Yb and mixed valence behavior. This value is characteristic of the $4f^6$ (Eu^{3+}) and $4f^{13}$ (Yb^{3+}) configurations and arises due to a $2p_{3/2}$ to 5*d* transition.[55] These results directly corroborate with magnetic susceptibility data, which predicts trivalent Eu and Yb in the system.

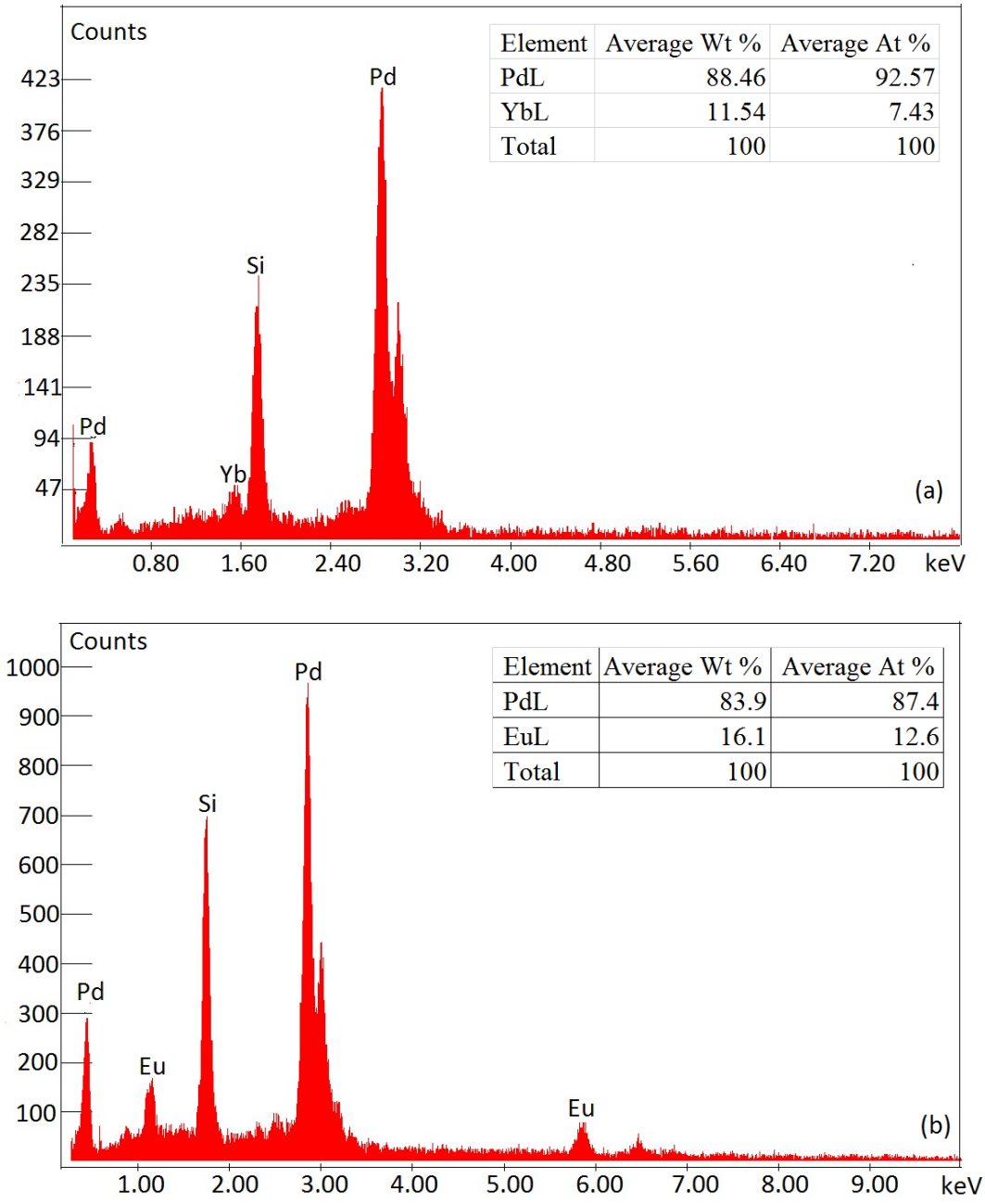

Figure 2.8. EDAX spectra of (a) Yb_xPd_{1-x} and (b) Eu_xPd_{1-x} nanoparticles. The table shown in the inset list the average composition obtained from the EDAX measurements.

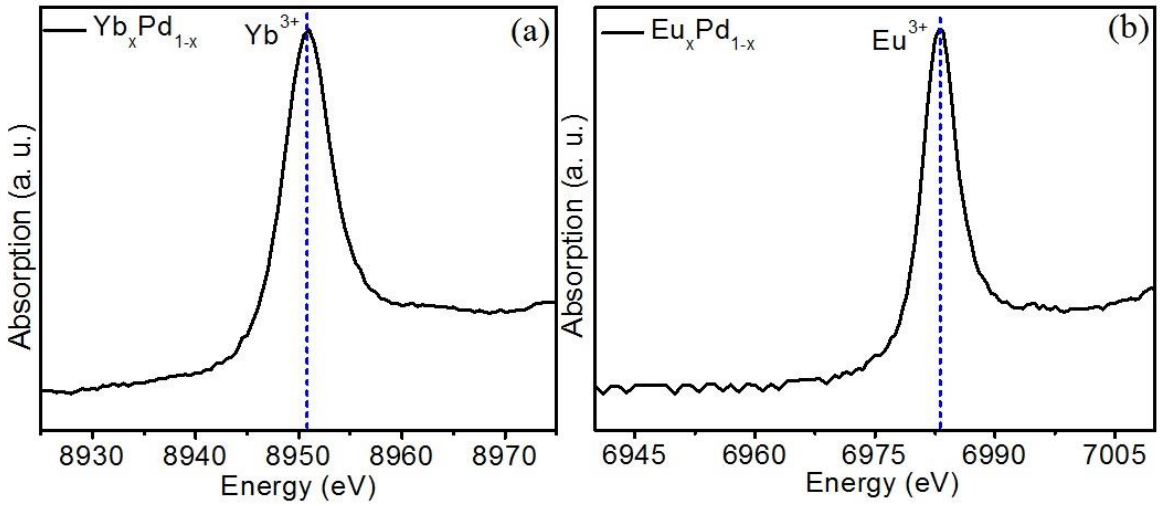

Figure 2.9. X-ray absorption near edge spectroscopy of Yb_L$_{III}$ and Eu_L$_{III}$ in (a) Yb_xPd_{1-x} and (b) Eu_xPd_{1-x} compounds.

2.4.5. Electrochemical Catalytic Activity

2.4.5.1. Comparison of EOR activity of RE_xPd_{1-x} (*RE* = Yb, Eu)

The EOR studies of pure Yb_xPd_{1-x}, Eu_xPd_{1-x} and commercial Pd/C were performed in alkaline medium (0.5 M KOH) by running CV in the potential ranges (-0.85-0.3 V) at a sweep rate of 50 mV/s.

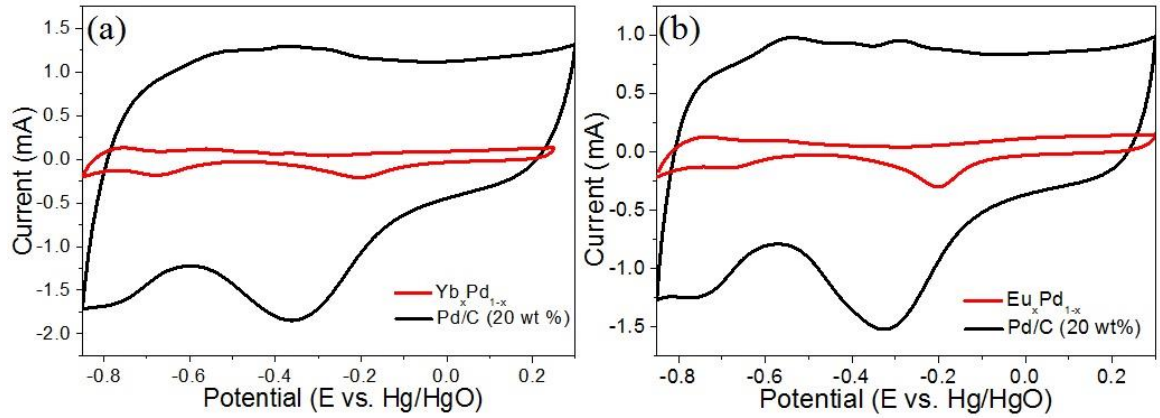

Figure 2.10. Cyclic voltammagram of (a) Yb_xPd_{1-x} and (b) Eu_xPd_{1-x} in N_2 saturated 0.5 M KOH measured at a sweep rate of 50 mV/sec.

Figure 2.10 shows the characteristic CV curve of the catalyst and comparison to the commercially available Pd/C (20 wt%). Two potential peaks can be observed in the

forward potential scan which correspond to different electrochemical processes occurring on the surface of the catalyst. Peak in the potential range between -0.8-0.65V is due to the oxidation of the adsorbed hydrogen.[56-59]

$$\mathbf{Pd\text{-}H_{ads} + OH^- \rightarrow Pd + H_2O + e^-}$$

Another peak emerges in the range -0.2 to 0.2 V. This can be attributed to the formation of the palladium (II) oxide layer on the surface of the catalyst. The mechanism of the process still remains unclear. However, it is accepted that OH^- are first chemisorbed in the initial stage of the oxide formation and then they are transformed to higher oxides.[60]

$$\mathbf{Pd + OH^- \leftrightarrow Pd\text{-}OH_{ads} + e^-}$$

$$\mathbf{Pd\text{-}OH_{ads} + OH^- \leftrightarrow Pd\text{-}O + H_2O + e^-}$$

$$\mathbf{Pd\text{-}OH_{ads} + Pd\text{-}OH_{ads} \leftrightarrow Pd\text{-}O + H_2O}$$

Another peak around -0.2 V during the reverse scan corresponds to the reduction of Pd (II) oxide.

$$\mathbf{Pd\text{-}O + H_2O + 2e^- \leftrightarrow Pd + 2OH^-}$$

The cyclic voltammetric behaviour of the process of electrooxidation of ethanol on RE_xPd_{1-x} electrode surface in 0.5 M KOH is shown in **Figure 2.10**. The CV curves have been collected with a sweep rate of 50 mV/s. A single oxidation peak can be seen in the anodic sweep, in the range -0.1 V to 0.1 V vs Hg/HgO, which corresponds to the oxidation of ethanol. Another oxidation peak in the cathodic sweep can be attributed to the process of oxidation of surface-adsorbed CO_{ads} species. Here, under similar experimental conditions (at 0.5 M KOH+1 M EtOH), the recorded maximum of oxidation current-density of both Yb_xPd_{1-x} and Eu_xPd_{1-x}, at ca. 1.0 V, was approximately 8 and 5

times as high as the corresponding value for the polycrystalline Pd/C (20 wt %) modified electrode (**Figure 2.11**).

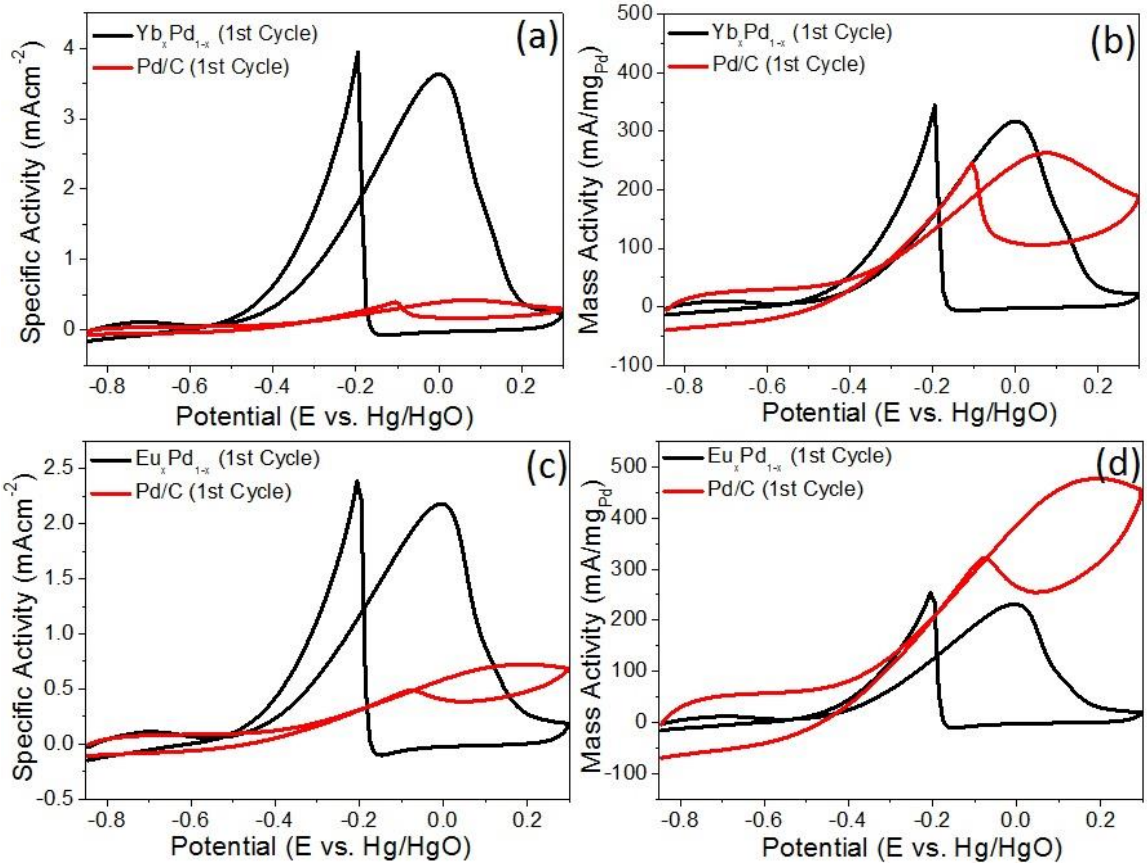

Figure 2.11. Cyclic voltammograms for the oxidation of 1 M ethanol in 0.5 M KOH at a scan rate of 50 mVs^{-1}. Comparison of the (a) specific activity and (b) mass activity of Yb_xPd_{1-x}, (c) specific activity and (d) mass activity of Eu_xPd_{1-x} with that of commercial Pd/C (20 wt%) towards ethanol electroxidation.

In terms of specific activity, *RE* based catalysts show better activity compared to commercially available Pd/C. But when compared in terms of mass activity, Eu_xPd_{1-x} do not show enhancement in activity. However, Yb_xPd_{1-x} shows slight enhancement in the activity of Pd.

The activity and the stability of the catalyst were checked by cycling the catalyst in the potential range -0.85 V to 0.3 V vs. Hg/HgO at a sweep rate of 0.1 V/s (**Figure 2.12**). The activity of both catalysts increases with increasing cycle number. This can be

attributed to the fact that Pd surface gets cleaned up of various intermediates adsorption with increase in cycle number.

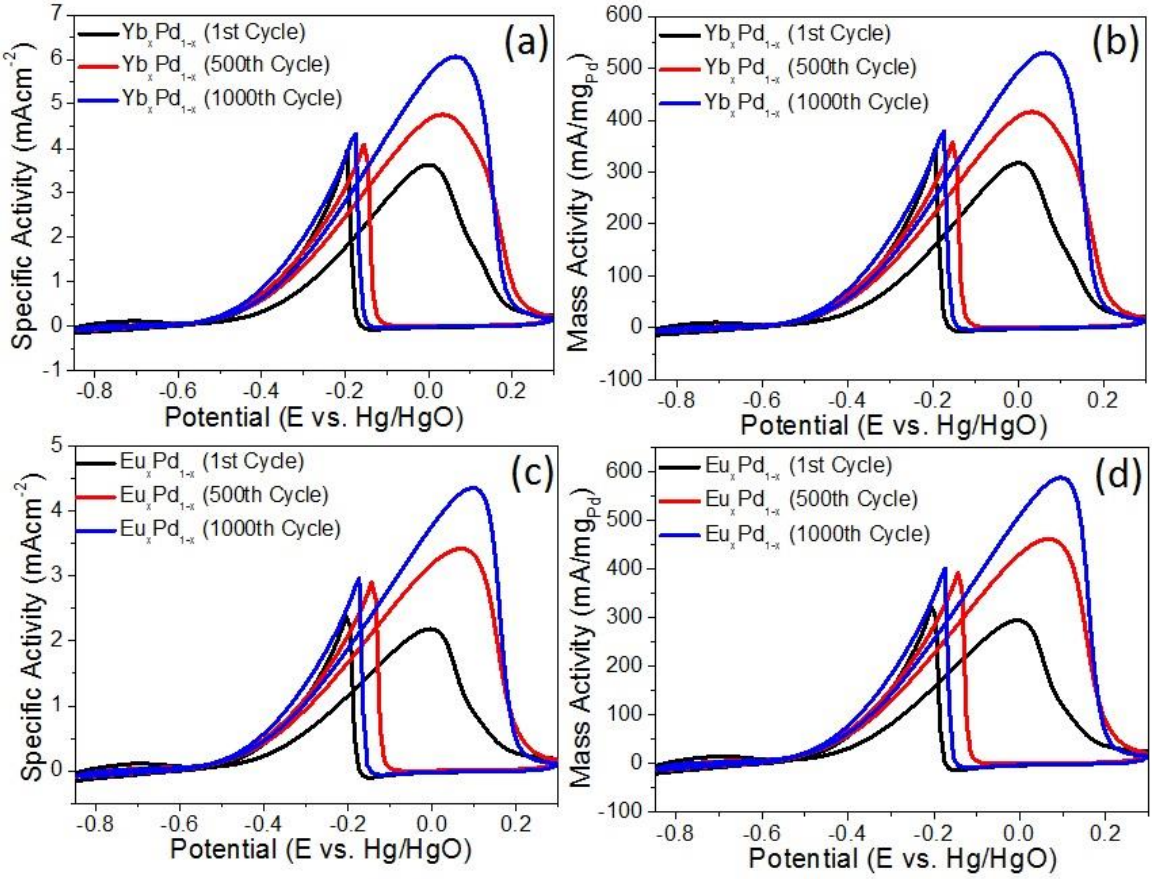

Figure 2.12. (a) Specific activity, (b) mass activity of Yb_xPd_{1-x} and (c) specific activity, (d) mass activity of Eu_xPd_{1-x} at 1st, 500th and 1000th cycle towards ethanol oxidation.

Figure 2.13 shows the change in the specific activity and mass activity of the samples with increase in cycle number. The activity of the samples is compared with that of the commercially available Pd/C (20 wt%). **Table 2.1** lists out the number of times increase in the activity of the sample with respect to the Pd/C catalyst. It can be concluded from the table that doping with Yb enhances the activity of Pd to a much greater extent compared to the Eu doped Pd.

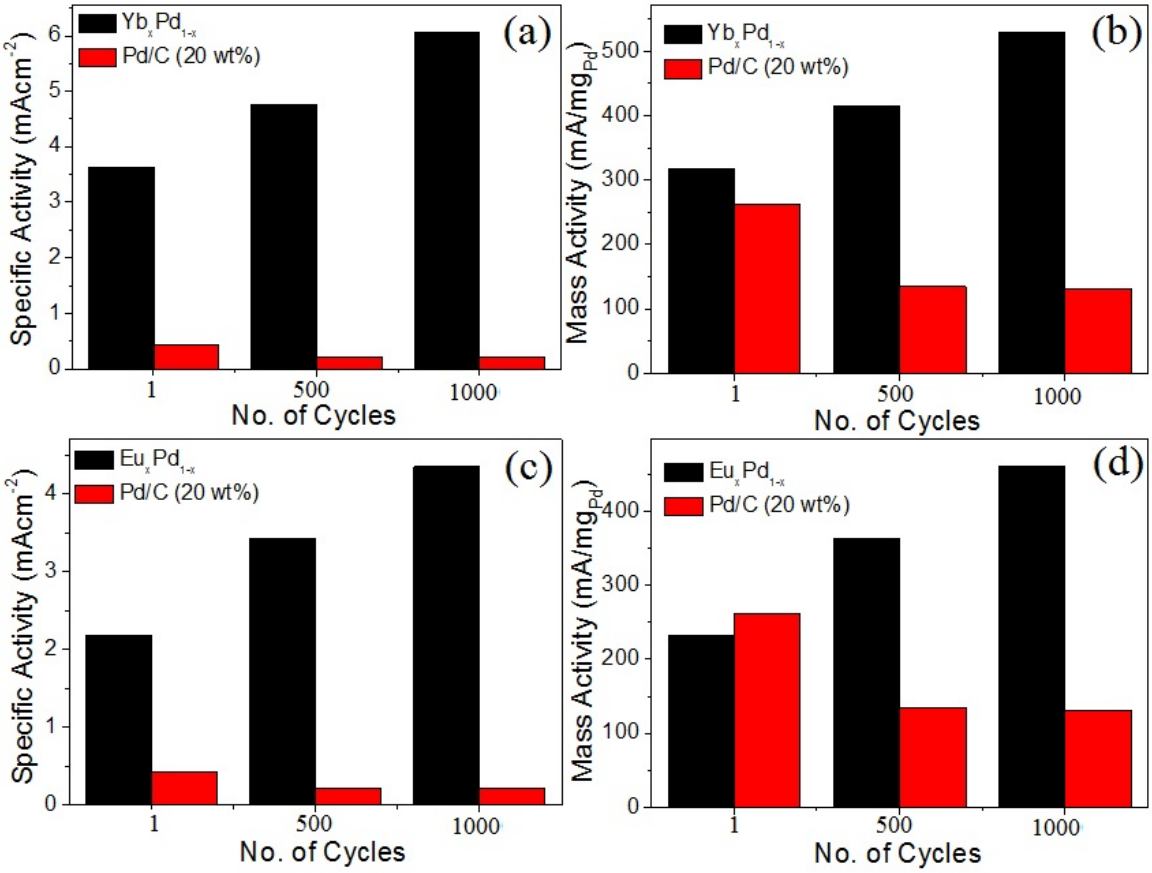

Figure 2.13. Comparison of the electrochemical activity between RE_xPd_{1-x} and Pd/C towards ethanol oxidation as a function of the number of cycles. (a) Specific activity of Yb_xPd_{1-x} and Pd/C, (b) mass Activity of Yb_xPd_{1-x} and Pd/C, (c) specific activity of Eu_xPd_{1-x} and Pd/C and (d) mass activity of Yb_xPd_{1-x} and Pd/C at 1st, 500th and 1000th cycle for ethanol oxidation

Table 2.1. Electro-catalytic activity results for the oxidation of ethanol on Yb_xPd_{1-x} and Eu_xPd_{1-x} nanocatalysts.

	Yb_xPd_{1-x}		Eu_xPd_{1-x}	
Cycle No.	Increase in Specific Activity	Increase in Mass Activity	Increase in Specific Activity	Increase in Mass Activity
1	8.6	1.2	5.1	0.9
500	21.8	3	15.6	2.7
1000	28.6	4	20.5	3.5

The stability of the RE_xPd_{1-x} NPs for EOR was investigated by employing chronoamperometry (CA) technique at -0.2 V for 1000 sec (**Figure 2.14**). It can be clearly observed that current decay is slower for Yb_xPd_{1-x}, which indicates superior electrochemical stability during 1000 sec test. The CA curve shows that Yb_xPd_{1-x} has good tolerance towards ethanol electro-oxidation.

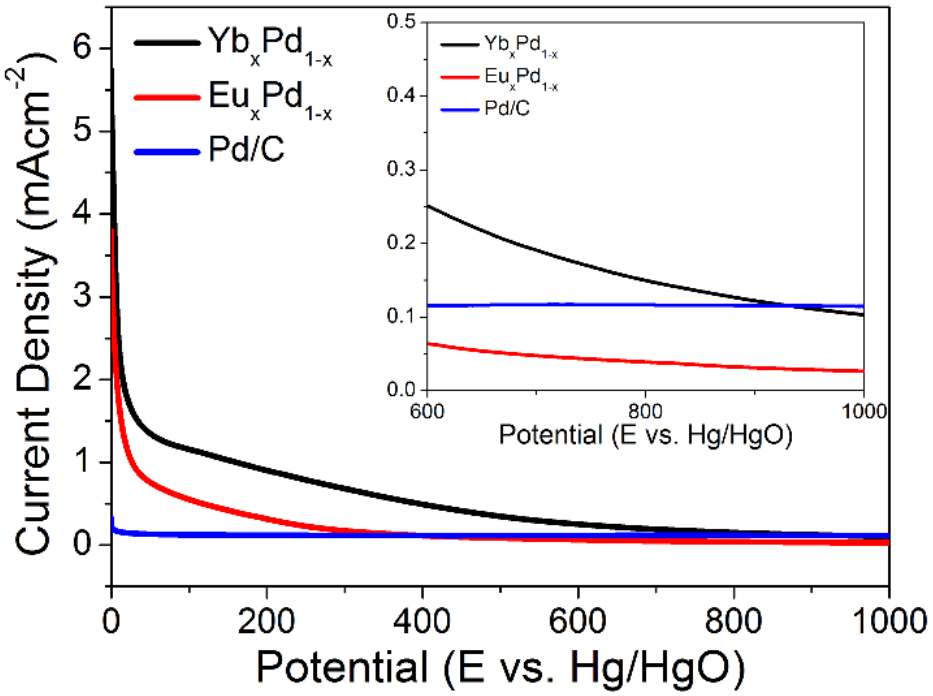

Figure 2.14. Comparison of CA measurement obtained for (a) Yb_xPd_{1-x} and (b) Eu_xPd_{1-x} nanoparticles in 0.5 M KOH + 1 M EtOH solution at -0.2 V vs Hg/HgO for ethanol electroxidation

2.4.5.2. Comparison of EOR activity of TM_xPd_{1-x} (*TM* = Ni, Cr)

To understand the role of *RE* in amplifying the activity of palladium, TM_xPd_{1-x} (*TM* = Ni,Cr) have been synthesized and ethanol electroxidation have been studied.

Figure 2.15 shows the specific activity and mass activity of the sample with respect to the cycle number. Both the catalyst shows anomalous behavior with increase in cycle number. Specific activity of the catalyst for Ni_xPd_{1-x} decreases with increase in cycle number (**Figure 2.15a,b**). A shift in peak potential is observed which may be due to

the leaching out nickel from the bulk. But, in case of Cr_xPd_{1-x}, activity of the sample increases till 500th cycle and then decreases again (**Figure 2.15c,d**). Increase observed may be attributed to the fact that the surface of the catalyst gets activated after some cycles.

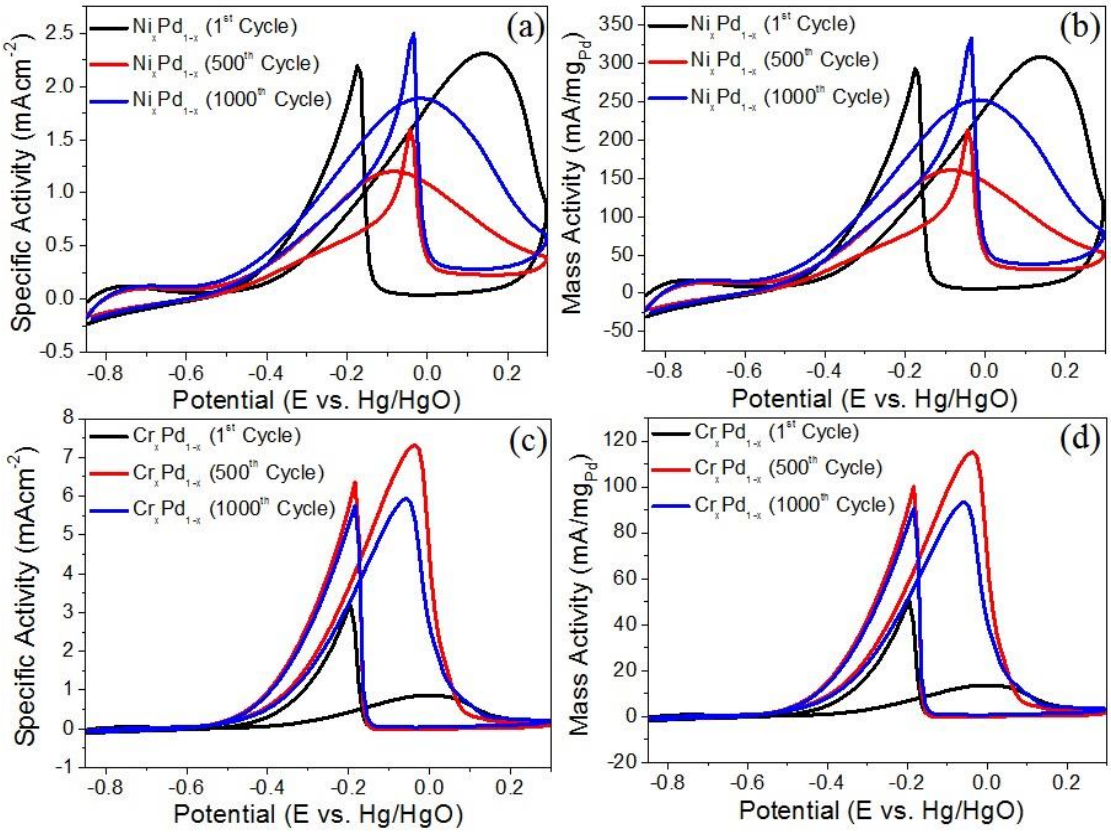

Figure 2.15. (a) Specific activity, (b) mass activity of Ni_xPd_{1-x} and (c) specific activity, (d) mass activity of Cr_xPd_{1-x} at 1st, 500th and 1000th cycle towards ethanol oxidation.

Figure 2.16 shows the comparison of specific activity and mass activity of the sample with that of the Pd/C. Enhancement in the specific activity of the *TM* doped Pd is observed for both the sample. However, the mass activity in both the case is lower compared to Pd/C. Chronoamperometric measurements were carried out in 0.5 M KOH at -0.2 V vs Hg/HgO for 1000 sec. Ni-doped Pd was found to show better activity compared to the Cr analogue and Pd/C (**Figure 2.17**).

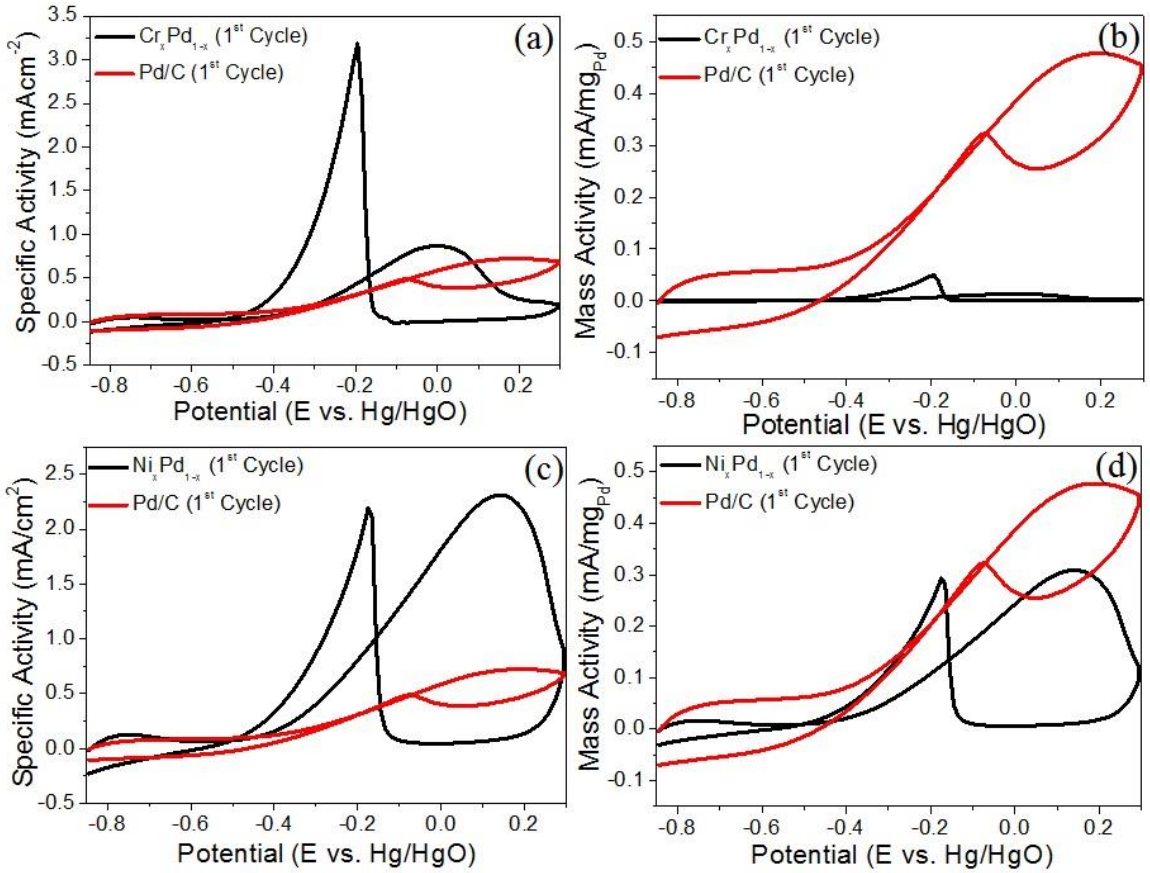

Figure 2.16. Cyclic voltammograms for the oxidation of 1 M ethanol in 0.5 M KOH at a scan rate of 50 mVs^{-1}. Comparison of the (a) specific activity and (b) mass activity of Cr_xPd_{1-x}, (c) specific activity and (d) mass activity of Ni_xPd_{1-x} with that of commercial Pd/C (20 Wt%) towards ethanol electroxidation.

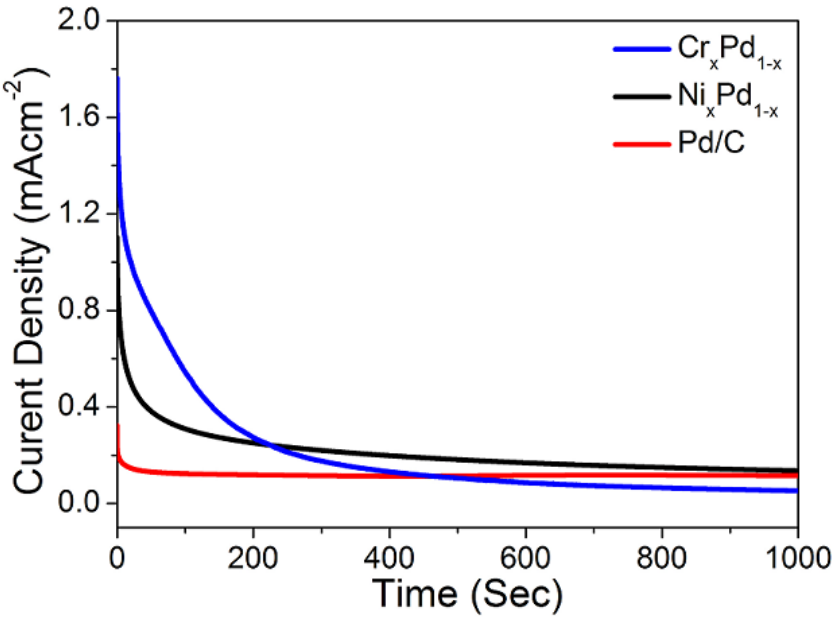

Figure 2.17. Comparison of CA measurement for Cr_xPd_{1-x}, Ni_xPd_{1-x} and commercial Pd/C catalysts in 0.5 M KOH + 1 M EtOH solution at -0.2 V vs Hg/HgO.

Bar chart representation of the specific activity and the mass activity of Ni_xPd_{1-x} and Cr_xPd_{1-x} with increase in cycle number suggest the stability of the sample (**Figure 2.18**). The increase in catalytic activity upon cycling is compared with the Pd/C is listed in **Table 2.2**. It can be clearly concluded that Ni doped Pd is a better catalyst both in terms of activity and stability.

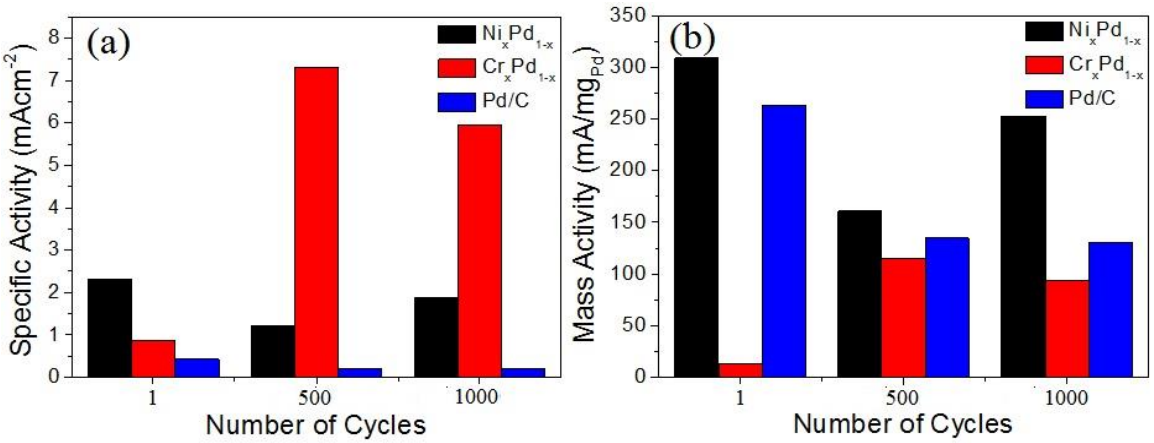

Figure 2.18. Comparison of the activity of TM_xPd_{1-x} with Pd/C as a function of number of cycles. (a) Specific activity of Ni_xPd_{1-x}, Cr_xPd_{1-x} and Pd/C, (b) mass activity of Ni_xPd_{1-x}, Cr_xPd_{1-x} and Pd/C for ethanol oxidation.

Table 2.2. Electro-catalytic activity results for the oxidation of ethanol on Cr_xPd_{1-x} and Ni_xPd_{1-x} nanocatalysts.

	Cr_xPd_{1-x}		**Ni_xPd_{1-x}**	
Cycle No.	Increase in Specific activity	Increase in Mass activity	Increase in Specific activity	Increase in Mass activity
1	2	0.05	5.44	1.17
500	33.5	0.11	5.51	1.19
1000	28	0.71	8.9	1.93

2.4.5.3. Comparison of EOR activity of RE_xPt_{1-x} with RE_xPd_{1-x} (*RE* = Yb, Eu)

Same reaction parameters were followed in studying the electrocatalytic activity of *RE*xPt1-x. **Figure 2.19** shows the cycle-dependent specific activity and mass activity

of the sample. Yb-doped Pt compound shows better activity compared to the Eu counterpart.

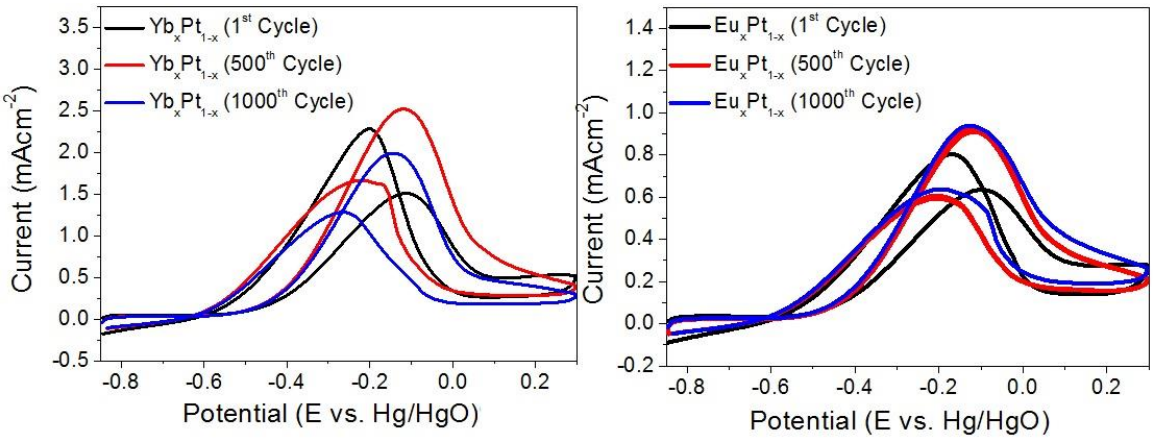

Figure 2.19. Specific activity of (a) Yb_xPt_{1-x} and (b) Eu_xPt_{1-x} at 1st, 500th and 1000th cycle towards ethanol oxidation.

Table 2.2. Comparison of specific activity of RE_xX_{1-x} (*RE* = Yb, Eu and X = Pd, Pt) nanocatalysts results for the oxidation of ethanol.

	Specific Activity			
Cycle No.	**Yb_xPt_{1-x}**	**Yb_xPd_{1-x}**	**Eu_xPt_{1-x}**	**Eu_xPd_{1-x}**
1	1.51	3.63	0.64	2.18
500	2.52	4.76	0.91	3.42
1000	1.99	6.06	0.94	4.35

It can be clearly seen from **Table 2.2** that *RE* doped Pd compounds have higher specific activity compared to the *RE* doped Pt nanocatalysts. Pt compound has less activity, which may be due to the CO poisoning.[61] Among the *RE*s, Yb shows the best activity for ethanol electroxidation.

2.5. Proposed Mechanism of ethanol electroxidation

Very few studies have addressed the mechanism of complete ethanol electrooxidation due to its complexity and generally incomplete oxidation. However, the oxidation mechanism to acetaldehyde and acetic acid is better known and generally accepted. A study of the composition of the products and intermediates of an ethanol fuel cell was made by Paik et al. showing a wide variety of products ranging from CO_2 and simple C1 molecules such as formic acid and methanol to complex molecules such as C2

radicals and ethers showing the oxidation of ethanol follows a very complex mechanism formed of various reaction paths.[62]

It is generally accepted that the oxidation of ethanol in alkaline media starts with the formation of either a CH_3CHO_{ads} species on the path to acetaldehyde or a strongly adsorbed ethoxy molecules on the surface of the Pd after the adsorption of ethanol.[60, 63] The oxidation of this ethoxy molecule is thought to be the rate limiting step of ethanol electrooxidation rather than the dissociative adsorption of ethanol.[64] The oxidation of the ethoxy molecule is followed by the desorption of the adsorbed molecule in a non-rate limiting step.[60]

$$\mathbf{Pd + CH_3CH_2OH \rightarrow Pd\text{-}CH_3CH_2OH_{ads}}$$

$$\mathbf{Pd\text{-}CH_3CH_2OH_{ads} + 2OH^- \rightarrow Pd + CH_3CHO + 2H_2O + 2e^-}$$

$$\mathbf{Pd\text{-}CH_3CH_2OH_{ads} + 3OH^- \rightarrow Pd + CH_3CO_{ads} + 3H_2O + 3e^-}$$

$$\mathbf{Pd + OH^- \rightarrow Pd\text{-}OH_{ads} + e^-}$$

$$\mathbf{Pd\text{-}CH_3CO_{ads} + Pd\text{-}OH_{ads} \rightarrow Pd\text{-}CH_3COOH_{ads}}$$

$$\mathbf{Pd\text{-}CH_3COOH_{ads} + OH^- \rightarrow Pd + CH_3COO^- + H_2O}$$

2.6. Concluding Remarks

We have successfully synthesized Yb and Eu substituted RE_xPd_{1-x} (*RE* = Eu and Yb) nanoparticles using simple solvothermal synthetic technique. The most important part of our project work is that the electrocatalytic activity of *RE* based nanoparticles have been compared with transition metal based nanoparticles (Cr_xPd_{1-x} and Ni_xPd_{1-x}) and have been found to be catalytically more active than its transition metal counterparts. Next we compared the activity of RE_xPd_{1-x} with that of the RE_xPt_{1-x} and still RE_xPd_{1-x} was found to have more activity. We firmly believe that *RE* doped Pd nanoparticles are promising materials towards energy applications in the near future and that these compounds have

the potential to completely change the outlook of various electrochemical reactions in the days to come.

2.4. References

1. Shen, S. Y.; Zhao, T. S.; Xu, J. B.; Li, Y. S., *J. Power Sources* **2010,** *195* (4), 1001-1006.

2. Zhang, Z. Y.; Xin, L.; Sun, K.; Li, W. Z., *Int. J. Hydrogen Energ.* **2011,** *36* (20), 12686-12697.

3. Li, Y. S.; Zhao, T. S.; Liang, Z. X., *J. Power Sources* **2009,** *187* (2), 387-392.

4. Verma, A.; Jha, A. K.; Basu, S., *J. Power Sources* **2005,** *141* (1), 30-34.

5. Matsuoka, K.; Iriyama, Y.; Abe, T.; Matsuoka, M.; Ogumi, Z., *J. Power Sources* **2005,** *150*, 27-31.

6. Colmenares, L.; Wang, H.; Jusys, Z.; Jiang, L.; Yan, S.; Sun, G. Q.; Behm, R. J., *Electrochim. Acta* **2006,** *52* (1), 221-233.

7. Wang, H.; Jusys, Z.; Behm, R. J., *J. Power Sources* **2006,** *154* (2), 351-359.

8. Wang, Q.; Sun, G. Q.; Jiang, L. H.; Xin, Q.; Sun, S. G.; Jiang, Y. X.; Chen, S. P.; Jusys, Z.; Behm, R. J., *Phys. Chem. Chem. Phys.* **2007,** *9* (21), 2686-2696.

9. Huang, L.; Sorte, E. G.; Sun, S. G.; Tong, Y. Y. J., *Chem. Commun.* **2015,** *51* (38), 8086-8088.

10. Neto, A. O.; Giz, M. J.; Perez, J.; Ticianelli, E. A.; Gonzalez, E. R., *J. Electrochem. Soc.* **2002,** *149* (3), A272-A279.

11. Vigier, F.; Coutanceau, C.; Hahn, F.; Belgsir, E. M.; Lamy, C., *J. Electroanal. Chem.* **2004,** *563* (1), 81-89.

12. Christensen, P. A.; Jones, S. W. M.; Hamnett, A., *Phys. Chem. Chem. Phys.* **2013,** *15* (40), 17268-17276.

13. He, Q. G.; Shyam, B.; Macounova, K.; Krtil, P.; Ramaker, D.; Mukerjee, S., *J. Am. Chem. Soc.* **2012,** *134* (20), 8655-8661.

14. Suffredini, H. B.; Salazar-Banda, G. R.; Avaca, L. A., *J. Power Sources* **2007,** *171* (2), 355-362.

15. Huang, Y. Y.; Cai, J. D.; Liu, M. Y.; Guo, Y. L., *Electrochim. Acta* **2012,** *83*, 1-6.

16. Matsumoto, F., *Electrochemistry* **2012,** *80* (3), 132-138.

17. Tusi, M. M.; Polanco, N. S. O.; da Silva, S. G.; Spinace, E. V.; Neto, A. O., *Electrochem. Commun.* **2011,** *13* (2), 143-146.

18. Figueiredo, M. C.; Santasalo-Aarnio, A.; Vidal-Iglesias, F. J.; Solla-Gullon, J.; Feliu, J. M.; Kontturi, K.; Kallio, T., *Appl. Catal. B-Environ.* **2013,** *140*, 378-385.

19. Tayal, J.; Rawat, B.; Basu, S., *Int. J. Hydrogen Energ.* **2012,** *37* (5), 4597-4605.

20. Li, M.; Cullen, D. A.; Sasaki, K.; Marinkovic, N. S.; More, K.; Adzic, R. R., *J. Am. Chem. Soc.* **2013,** *135* (1), 132-141.

21. Dutta, A.; Ouyang, J. Y., *ACS Catal.* **2015,** *5* (2), 1371-1380.

22. Jacob, J. M.; Corradini, P. G.; Antolini, E.; Santos, N. A.; Perez, J., *Appl. Catal. B-Environ.* **2015,** *165*, 176-184.

23. Zhao, Y. H.; Wang, R. Y.; Han, Z. X.; Li, C. Y.; Wang, Y. S.; Chi, B.; Li, J. Q.; Wang, X. J., *Electrochim. Acta* **2015,** *151*, 544-551.

24. Yang, X.; Yang, Q. D.; Xu, J.; Lee, C. S., *J. Mater. Chem.* **2012,** *22* (48), 25492-25492.

25. Datta, J.; Dutta, A.; Mukherjee, S., *J. Phys. Chem. C* **2011,** *115* (31), 15324-15334.

26. Zhu, W.; Ke, J.; Wang, S. B.; Ren, J.; Wang, H. H.; Zhou, Z. Y.; Si, R.; Zhang, Y. W.; Yan, C. H., *ACS Catal.* **2015,** *5* (3), 1995-2008.

27. Liao, F. L.; Lo, T. W. B.; Sexton, D.; Qu, J.; Wu, C. T.; Tsang, S. C. E., *Catal. Sci. Technol.* **2015,** *5* (2), 887-896.

28. Almeida, T. S.; Van Wassen, A. R.; VanDover, R. B.; de Andrade, A. R.; Abruna, H. D., *J. Power Sources* **2015,** *284*, 623-630.

29. Carmo, M.; Sekol, R. C.; Ding, S. Y.; Kumar, G.; Schroers, J.; Taylor, A. D., *ACS Nano* **2011,** *5* (4), 2979-2983.

30. Li, L.; Yuan, X. X.; Xia, X. Y.; Du, J.; Ma, Z.; Ma, Z. F., *J. Inorg. Mater.* **2014,** *29* (10), 1044-1048.

31. He, Q. G.; Chen, W.; Mukerjee, S.; Chen, S. W.; Laufek, F., *J. Power Sources* **2009,** *187* (2), 298-304.

32. Li, G. L.; Jiang, L. H.; Jiang, Q.; Wang, S. L.; Sun, G. Q., *Electrochim. Acta* **2011,** *56* (22), 7703-7711.

33. Zhu, L. D.; Zhao, T. S.; Xu, J. B.; Liang, Z. X., *J. Power Sources* **2009,** *187* (1), 80-84.

34. Wang, H.; Xu, C. W.; Cheng, F. L.; Jiang, S. P., *Electrochem. Commun.* **2007,** *9* (5), 1212-1216.

35. Dutta, A.; Datta, J., *J. Phys. Chem. C* **2012,** *116* (49), 25677-25688.

36. Wang, Y.; Shi, F. F.; Yang, Y. Y.; Cai, W. B., *J. Power Sources* **2013,** *243*, 369-373.

37. Bahemmat, S.; Ghassemzadeh, M.; Afsharpour, M.; Harms, K., *Polyhedron* **2015,** *89*, 196-202.

38. Du, W. X.; Mackenzie, K. E.; Milano, D. F.; Deskins, N. A.; Su, D.; Teng, X. W., *ACS Catal.* **2012,** *2* (2), 287-297.

39. da Silva, S. G.; Assumpcao, M. H. M. T.; Silva, J. C. M.; De Souza, R. F. B.; Spinace, E. V.; Neto, A. O.; Buzzo, G. S., *Int. J. Electrochem. Sci.* **2014,** *9* (10), 5416-5424.

40. Mao, H. M.; Wang, L. L.; Zhu, P. P.; Xu, Q. J.; Li, Q. X., *Int. J. Hydrogen Energ.* **2014,** *39* (31), 17583-17588.

41. Zhou, W. J.; Zhou, Z. H.; Song, S. Q.; Li, W. Z.; Sun, G. Q.; Tsiakaras, P.; Xin, Q., *Appl. Catal. B-Environ.* **2003,** *46* (2), 273-285.

42. Bambagioni, V.; Bianchini, C.; Filippi, J.; OberhauserIal, W.; Marchionni, A.; Vizza, F.; Psaro, R.; Sordelli, L.; Foresti, M. L.; Innocenti, M., *Chemsuschem* **2009,** *2* (1), 99-112.

43. Santos, D. M. F.; Sljukic, B.; Amaral, L.; Sequeira, C. A. C.; Maccio, D.; Saccone, A., *Polymer Electrolyte Fuel Cells 14* **2014,** *64* (3), 1095-1102.

44. Rosalbino, F.; Delsante, S.; Borzone, G.; Angelini, E., *In.t J. Hydrogen Energ.* **2008,** *33* (22), 6696-6703.

45. Subbarao, U.; Gutmann, M. J.; Peter, S. C., *Inorg. Chem.* **2013,** *52* (4), 2219-2227.

46. Subbarao, U.; Peter, S. C., *Inorg. Chem.* **2012,** *51* (11), 6326-6332.

47. Peter, S. C.; Sarkar, S.; Kanatzidis, M. G., *Inorg. Chem.* **2012,** *51* (20), 10793-10799.

48. Fisher, I. R.; Bud'ko, S. L.; Song, C.; Canfield, P. C.; Ozawa, T. C.; Kauzlarich, S. M., *Phys. Rev. Lett.* **2000,** *85* (5), 1120-1123.

49. Nilsson, A.; Eriksson, B.; Martensson, N.; Andersen, J. N.; Onsgaard, J., *Phys. Rev. B* **1987,** *36* (17), 9308-9311.

50. Pauling, L., *The Nature of the Chemical Bond*. United States, 1960.

51. Pauling, L., *The Nature of the Chemical Bond*. 3 ed.; Cornel University Press: Ithaca, NY, 1960; p 410.

52. Harris, R.; Raynor, G. V., *J. Less-Common Metals* **1965,** *9*, 263-269.

53. Harris, I. R.; Raynor, G. V.; Winstanley, C. J., *J. Less-Common Met.* **1967,** *12*, 69-74.

54. Chon, G. B.; Shinoda, K.; Suzuki, S.; Jeyadevan, B., *Mater. Trans.* **2010,** *51* (4), 707-711.

55. Inoue, T.; Kubozono, Y.; Kashino, S.; Takabayashi, Y.; Fujitaka, K.; Hida, M.; Inoue, M.; Kanbara, T.; Emura, S.; Uruga, T., *Chem. Phys. Lett.* **2000,** *316*, 381−386.

56. Takamura, T.; Minamiyama, K. i., *J. Electrochem. Soc.* **1965,** *112* (3), 333-335.

57. Prabhuram, J.; Manoharan, R.; Vasan, H. N., *J. Appl. Electrochem. 28* (9), 935-941.

58. Grden, M.; Kotowski, J.; Czerwinski, A., *J. Solid. State Electr.* **2000,** *4* (5), 273-278.

59. Grden, M.; Czerwinski, A., *J. Solid. State Electr.* **2008,** *12* (4), 375-385.

60. Liang, Z. X.; Zhao, T. S.; Xu, J. B.; Zhu, L. D., *Electrochim. Acta* **2009,** *54* (8), 2203-2208.

61. Wang, Y.; Zou, S. Z.; Cai, W. B., *Catalysts* **2015,** *5* (3), 1507-1534.

62. Paik, Y.; Kim, S. S.; Han, O. H., *Electrochem. Commun.* **2009,** *11* (2), 302-304.

63. Friedl, J.; Stimming, U., *Electrochim. Acta* **2013,** *101*, 41-58.

64. Antolini, E.; Gonzalez, E. R., *J. Power Sources* **2010,** *195* (11), 3431-3450.

Chapter 3

3. Synthesis of novel hexagonal nanoparticles of $CoPd_2Se_2$ and its electrochemical ORR studies

3.1. Introduction

Interest in alkaline electrocatalysis has been growing in industry and space programmes due to less intermediate poisoning and higher stability.[1-2] Oxygen reduction reaction (ORR) in alkaline medium is of great industrial importance. They serve as cathode materials in numerous alkaline fuel cells, chlor-alkali electrolysis (for electrolysis of NaCl) with air depolarized cathodes,[3] and metal-air batteries.[4-5]

Adsorption energy of neutral species is weakly affected by potential difference between the electrodes whereas the adsorption of charged species has a strong potential dependence. Ionic species such as I^- adsorbs very strongly on Pt surface, in acidic medium, whereas it has very weak interaction with Pt surface in alkaline medium.[6] In alkaline medium, even if an ionic species such as SO_4^{2-} is present, the effect of electrocatalysis will be much weaker than it would be in acidic medium. Because of this particular reason, industries prefer electrocatalytic reactions in alkaline medium.[7]

However, electrochemical oxygen reduction reaction remains a major challenge in polymer electrolyte fuel cell (PEFC) applications due to a high overpotential. To date, only materials based on Pt have shown sufficient activity and stability for reliable proton exchange membrane fuel cell (PEMFC) operation.

Carbon-supported platinum-based alloy catalysts such as Pt-Fe/C,[8] Pt-Ni/C,[9] Pt-Co/C,[10] Pt-Cr/C[11] have been widely investigated as active material for ORR.

The need for Pt, however, poses problems due to the high cost and limited resources. Thus, mass production of Pt-based PEMFCs might be restricted in near future.[12-16] In addition, Pt is vulnerable to methanol oxidation, making its use as a cathode in direct methanol fuel cell inefficient. Extensive research efforts have been devoted to reduce the amount of Pt required in electrocatalysts that would show sufficient stability in acid, which is to date the only relevant medium for PEFCs due to the unavailability of alkaline membranes.

Chalcogenides represent another possible alternative to the Pt-based catalyst. Chalcogenide based catalysts such as NiS_2,[17] CoS_2,[18] $Co_{1-x}S$,[19] $CoSe_2$,[20-22] MoS_2,[23-25] WS_2[26] show promising applications towards electrochemical hydrogen evolution reaction. Co_3S_4[27] shows considerable activity towards ORR. Ruthenium selenides and their analogues are known to show quite high activity for the ORR as shown in **Table 3.1**.

Table 3.1. List of ORR kinetics data of some of the chalcogenide catalyst (reprinted with permission from ref [28] ©2011 Elsevier)

Catalysts	Onset Potential vs. RHE (V)	$E_{1/2}$ vs. RHE (V)	Reference
$Mo_{4.2}Ru_{1.8}Se_8$	0.87	0.54	29
$Mo_4Ru_6Se_4$	0.84	0.66	30
$Mo_4Ru_6Se_6$	0.85	0.67	30
$Mo_4Ru_6Se_8$	0.85	0.62	30
$Mo_4Ru_6Se_9$	0.85	0.60	30
$(Ru_{1-x}Mo_x)_ySeO_z$	0.85	0.58	1
$(Ru_{1-x}Mo_x)_ySeO_2$	0.90	0.72	31
Ru_xSe_y	0.83		32
Ru_xSe_y	0.87		32
$Ru_{1.92}Mo_{0.08}SeO_4$	0.85	0.71	33
$RuSe_{0.17}$	0.84	0.67	34
Ru	0.75	0.54	35
Ru/S	0.84	0.58	
Ru/Se	0.90	0.69	
Ru_xSe_y	0.90	0.71	
Pt/C	1.0	0.87	
$RuSe_x$/C	0.85	0.73	36
(WO_3)–$Ru_2Se_{0.1}$/C	0.90	0.59	37
$Ru_2Se_{0.1}$	0.90	0.50	
$RuSe_x$/C (Se, 6.3 wt%)	0.84	0.63	38
$RuSe_x$/C (Se, 11.8 wt%)	0.86	0.66	38
$RuSe_x$/C (Se, 16.7 wt%)	0.89	0.68	38
$RuSe_{0.15}$/C	0.81	0.70	39
$RuSe_{0.30}$/C	0.82	0.64	39
$RuSe_{0.60}$/C	0.84	0.62	39
RuSe/C	0.87	0.65	39
$(Ru_xSe_y)_{xyl}$	0.89	0.68	40
$(RuFeSe)_{xyl}$		0.69	40
$(RuFeSe)_{DCB}$		0.71	40
This Work	0.89	0.79	

Ternary metal chalcogenide are currently being explored for their promising application in ORR such as WCoSe.[41] Normally, tungsten and cobalt are not thermodynamically stable in this potential window due to electrochemical oxidation. However, after the formation of the W–Co–Se chalcogenide, no anodic oxidation current could be observed, indicating that the synthesized chalcogenide is electrochemically stable in this potential range. It has been reported that selenium can play a role in protecting the electrochemical oxidation of metals.[42] The preparations of several electrocatalysts with promising ORR activities including CoSe,[43] $CoSe_2$,[44] Co_9Se_8, CoS_2, Co_3S_4, FeS_2, $(Co,Ni)S_2$, $(Co,Fe)S_2$ and W–Co–Se, and chalcogen-free transition metals have been reported.[44]

In this work, the hexagonal shaped nanoparticles of $CoPd_2Se_2$ have been synthesized for the first time. Since chalcogenides have semi-conducting nature, 10 wt % Vulcan XC-72R has been used to increase the conductivity. The materials have been characterized using XRD, TEM, FESEM, EDX and XPS techniques. The compound shows good activity towards electrochemical ORR.

3.2. Experimental Section

3.2.1. Synthesis

3.2.1.1. Chemicals

Palladium acetylacetonate ($Pd(C_5H_7O_2)_2$, 99%), cobalt acetylacetonate ($Co(C_5H_7O_2)_2$, 99%), selenous acid (H_2SeO_3, 98%), trioctylphosphine ($P(C_8H_{17})_3$, 90%), oleylamine ($C_{18}H_{35}NH_2$, 70%) were purchased from Sigma Aldrich. All the reagents were used without further purification. Distilled water (18.2 mΩ) was used throughout the synthesis and measurements.

3.2.1.2. Synthesis of $CoPd_2Se_2$

$CoPd_2Se_2$ nanoparticles were synthesized by colloidal method. $Pd(acac)_2$ (0.1 mmol), H_2SeO_3 (0.1 mmol) and $Co(acac)_2$ (0.07 mmol) were mixed together in 25 ml oleyl amine in a 50 ml two-necked RB. 800 μL of trioctylphosphine was then added to the solution. The RB was then fitted to a condenser, vacummized and purged with Ar gas. It was then heated at 220 ^oC for 3 h. The product obtained was repeatedly washed with hexane-ethanol mixture for several times and then dried in vacuum oven at 60 ^oC for 6 h.

3.2.2. Characterization

3.2.2.1. Powder X-ray Diffraction (PXRD)

The PXRD measurements were done at room temperature on a Rigaku miniflex X-ray diffractometer with Cu-Kα X-ray source (λ = 1.5406 Å), equipped with a position sensitive detector in the angular range $20^o \leq 2\theta \leq 60^o$ with the step size 0.02^o and scan rate of 1 sec/step calibrated against corundum standard. The experimental patterns were compared to the pattern simulated from the database.

3.2.2.2. Powder XRD Refinement

Rietveld profile analysis in the Fullprof suite was used to refine the X-ray diffraction data. The background was estimated by the linear interpolation between a set background points with refinable heights, and the peak shapes were described by a gaussian function. Two phases were used to fit the experimental pattern. A scale factor, a zero error factor, cell parameters, shape and backgrounds were refined for both the phases.

3.2.2.3. Elemental Analysis

Quantitative microanalysis on all the samples were performed with a FEI NOVA NANOSEM 600 instrument equipped with an EDAX® instrument. Data were acquired with an accelerating voltage of 20 kV and a 100 s accumulation time. The EDAX analysis was performed using P/B-ZAF standardless method (where, Z = atomic no. correction factor, A = absorption correction factor, F = fluorescence factor, P/B = peak to background model) on selected spots and points.

3.2.2.4. Transmission Electron Microscopy (TEM)

TEM images and selected area electron diffraction patterns were collected using a JEOL JEM-2010 TEM instrument. The samples for these measurements were prepared by sonicating the nanocrystalline powders in ethanol and drop-casting a small volume onto a carbon-coated copper grid.

3.2.2.5. X-ray Photoelectron Spectroscopy (XPS)

XPS measurement was performed on an Omicron Nanotechnology spectrometer using a Mg−Kα (λ = 1253.6 eV) X-ray source with a relative composition detection better than 0.1%.

3.2.2.6. Electrochemical Studies

All the electrochemical measurements were carried out using a CHI 760E electrochemical workstation with three electrode channels at room temperature. A conventional three electrode set-up consisting of a glassy carbon (GC) (having diameter 3 mm) as working electrode, platinum wire as counter electrode and Hg/HgO (MMO) as reference electrode were used. Before all the measurements, the electrolyte was de-aerated with continuous purging of nitrogen gas for 30 min. The catalyst ink was

prepared by dispersing 1 mg of catalyst in 200 μL of mixed solvent solution (IPA: H_2O = 1:3 v/v). Nafion solution (5 wt%, Sigma Aldrich) is diluted with isopropyl alcohol (IPA) to 0.05 wt%. From the prepared catalyst ink, a 5 μL of the slurry was dropcasted on GC electrode and then 1 drop of 0.05 wt% of Nafion solution have been added to the dropcasted electrode and dried overnight in air. The GC electrode was polished with 0.05 μm alumina slurry and washed several times with distilled water prior to the deposition of catalyst slurry. Chronoamperometric (CA) measurements were performed in 0.1 M KOH electrolyte solution. Linear sweep voltammetry (LSV) was recorded with a sweep rate of 5 mV/s in 0.1 M KOH electrolyte solution under steady state conditions. Tafel plots (TP) were derived from LSV measurement.

3.3. Results and Discussions

3.3.1. Structure Analysis

The crystal structure of $CoPd_2Se_2$ is isotypic to K_2ZnO_2[45] crystallizing in orthorhombic system with *Ibam* space group. Parallel chains of edge-sharing $CoSe_{4/2}$ tetrahedra run along [0,0,1] and [½, ½, 1] as shown in **Figure 3.1.**[46] Co occupies tetrahedral voids formed by selenium (Figure 3.1 b). The Pd atoms are surrounded by five selenium atoms in a distorted quadratic–prismatic arrangement (**Figure 3.1. c**). **Figure 3.3** shows a section of a unit cell occupied by Se atoms in all the face-center. A quarter of the tetrahedral voids are occupied by the Co atoms. The Co–Se has a bond length of 2.348(1) Å which is slightly longer than the sum of Pauling's covalent radii of 2.33 Å (**Figure 3.2**). The Se–Co–Se angles within the tetrahedra are 115.61˚, 113.41˚ and 99.81˚, with a significant compression along the chain direction. This leads to short Co–Co distances of only 2.501(1) Å. These distances are even shorter than in fcc cobalt metal (2.503 Å). This indicates strong one-dimensional Co–Co bonding within the $CoSe_{4/2}$

chains. Palladium atoms separate the chains with only five selenium neighbors in a distorted quadratic–prismatic arrangement. Pd–Se bond lengths range from 2.475 to 2.852 Å. The shortest bonds are approximately the sum of the covalent radii (2.41 Å), whereas the longer Pd–Se distance of 2.852 Å indicates a rather weak interaction.

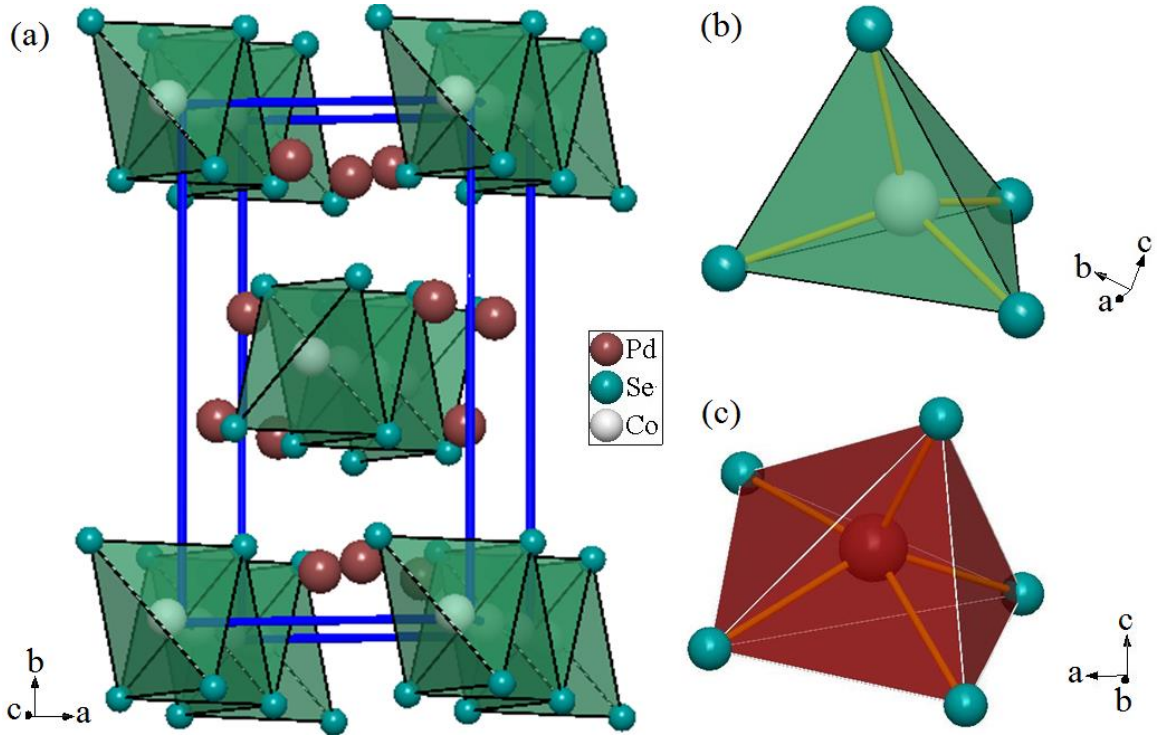

Figure 3.1. (a) Orthorhombic (*Ibam*) crystal structure of $CoPd_2Se_2$ showing parallel chains of $CoSe_{4/2}$ tetrahedra along c-axis. The unit cell is outlined as blue solid lines. (b) Co atoms are in tetrahedral environment and (c) Pd atoms are in distorted quadratic–prismatic arrangement.

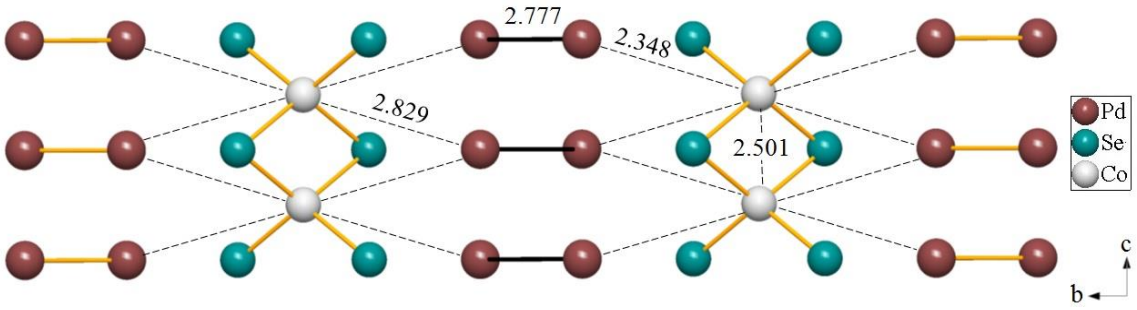

Figure 3.2. The crystal structure of the compound $CoPd_2Se_2$ showing Pd-Pd, Co-Co and Pd-Co bond-distances.

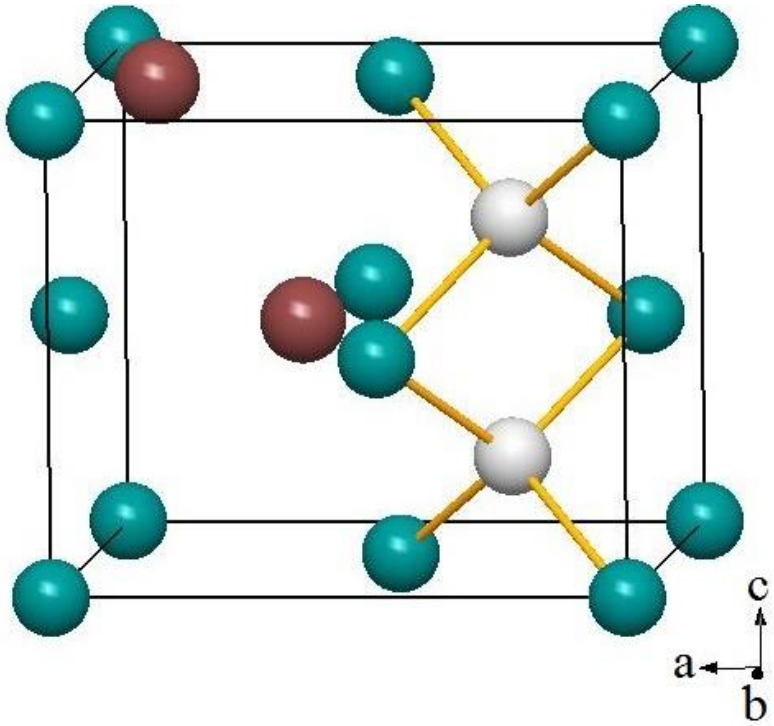

Figure 3.3. A fragment of a unit cell showing that the Se atoms occupy the fcc positions and one-fourth of the tetrahedral voids are occupied with Co atoms.

3.3.2. Synthesis and PXRD Analysis

The synthesis of CoPd2Se2 nanoparticles require oleyl amine as the solvent. Oleyl amine is a long chain primary alkyl amine. It not only act as a solvent and a surfactant but also as an electron donor at elevated temperature.[47] Oleyl amine acts as a reducing agent at 220 ^{o}C and trioctylphosphine (TOP) act as a stabilizing agent and also prevents agglomeration of nanoparticles.[48] Optimum ratio between them results in intermediate particle size.[49] In our synthesis approach, oleyl amine act as high boiling point coordinating solvent and also as a reducing and a capping agent.

The PXRD pattern of $CoPd_2Se_2$ was compared with the simulated patterns as shown in **Figure 3.4**. The prominent peaks (2θ values) observed at 35.94^{o}, 43.6^{o}, 50.36^{o} corresponds to the (211), (231) and (042) planes of $CoPd_2Se_2$, respectively. The PXRD pattern could be indexed as orthorhombic with *Ibam* space group and lattice parameters *a*

= 5.993 Å, *b* = 10.493 Å, *c* = 5.003 Å. **Figure 3.5** shows the presence of small percentage of $Pd_{17}Se_{15}$ in the PXRD pattern. To know the percentage of each phase present in the system, the PXRD data was refined with the following equation,

$$W_i = \frac{S_i\,(ZMV)_i}{\sum_{j=1}^{n} S_j\,(ZMV)_j}$$

where, W_i the weight fraction of phase 'i', S_i and S_j are the refined scale factor of phase 'i' and phase 'j' respectively, Z is the number of formula unit in a unit cell, M is the molar mass of respective phases, V is the volume of the unit cell.

Using the above mentioned formula, percentage of $CoPd_2Se_2$ and $Pd_{17}Se_{15}$ have been found to be 92.5 % and 7.5 % respectively.

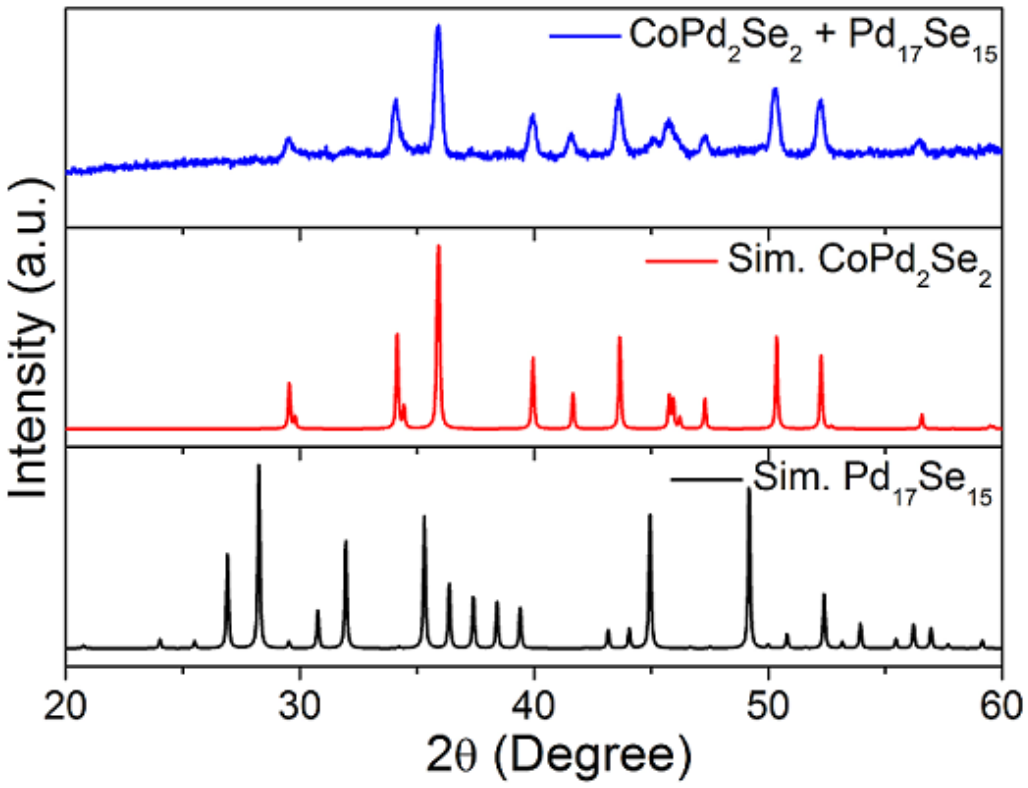

Figure 3.4. Comparison of experimental PXRD pattern with that of the simulated pattern of $CoPd_2Se_2$ and $Pd_{17}Se_{15}$.

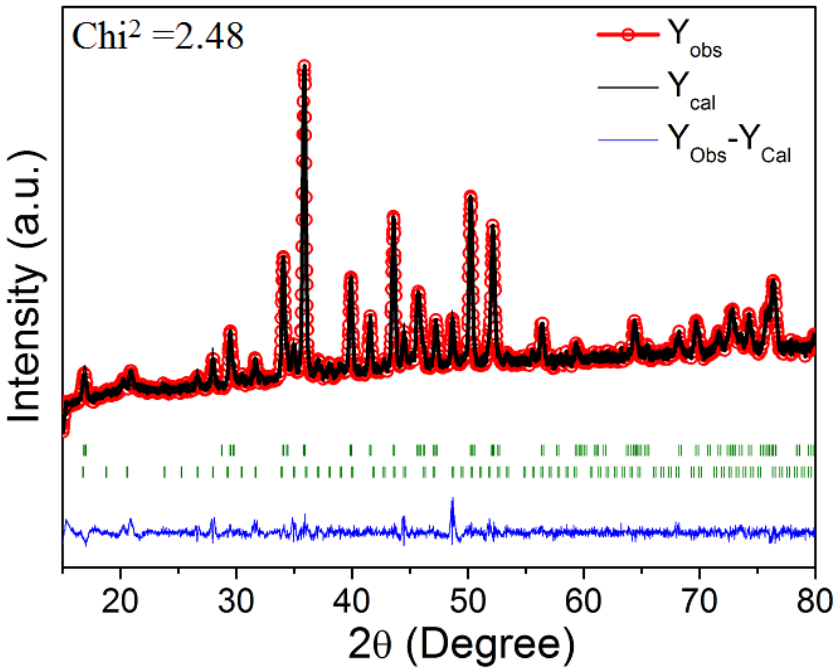

Figure 3.5. Rietveld refinement of the powder XRD pattern of as synthesized $CoPd_2Se_2$ nanoparticles. The fitting resulted with the additional peaks of second phase $Pd_{17}Se_{15}$.

3.3.3. TEM Analysis

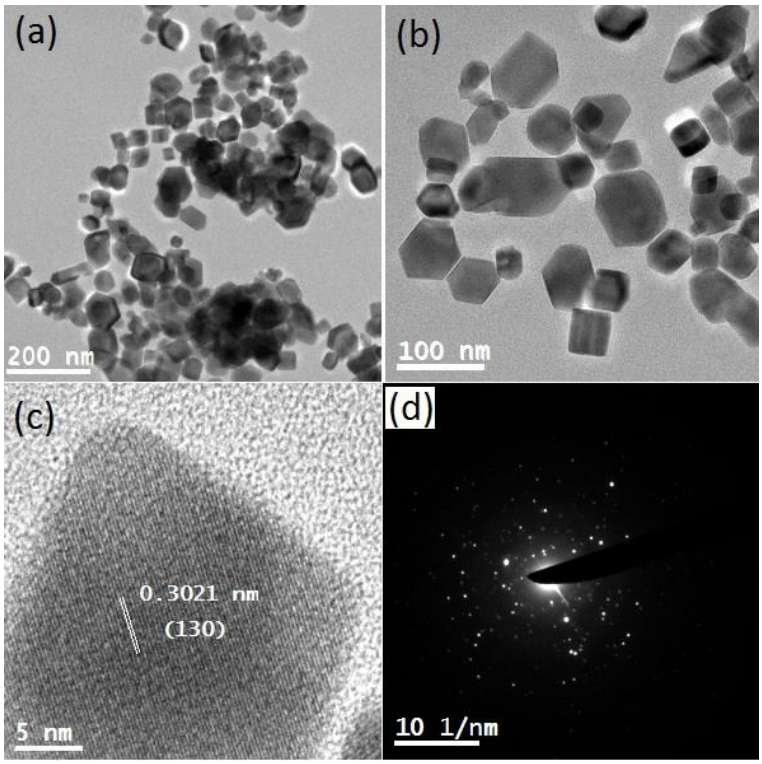

Figure 3.6. (a,b) TEM images shows the hexagonal nanoparticles, (c) HRTEM image shows the exposed (130) plane, (d) SAED pattern shows the polycrystalline of $CoPd_2Se_2$ nano particles.

The TEM images show the presence of hexagonal nanoparticles of size less than 100 nm (**Figure 3.6**) with (130) plane exposed. The SAED (**Figure 3.6d**) pattern describes the polycrystalline nature of the particles.

Chalcogenides have less electronic conductivity. To increase the electronic conductivity, 10 wt% of vulcan has been used as a support. TEM images of the as-prepared sample is shown in **Figure 3.7a**. A thin layer of carbon can be clearly seen in the background. HRTEM images is shown in **Figure 3.7b** which corresponds to (353) plane of the catalyst.

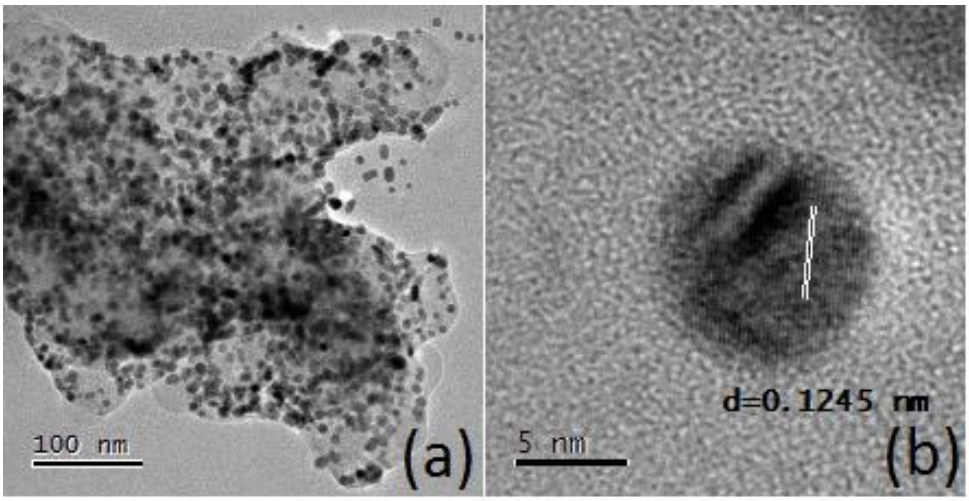

Figure 3.7. (a) TEM image shows that the particles are well-dispersed on vulcan, (b) HRTEM image of $CoPd_2Se_2$ nano particles shows that (353) surface is exposed with a d-spacing of 0.1245 nm.

3.3.4. FESEM Analysis

The FESEM images corroborate with the TEM images and show that the $CoPd_2Se_2$ nanoparticles have hexagonal-like morphology (**Figure 3.8**). The EDX spectrum (**Figure 3.9**) from the FESEM analysis clearly confirms the presence of Co, Pd and Se in the sample. In the EDX spectrum, peaks are observed at 0.7 and 6.9 keV for Co, 0.25 and 2.8 keV for Pd and 1.3 and 11.25 keV for Se. Strong peak at 1.7 keV confirms

the presence of Si element from the silicon wafer on which the sample has been coated. The absence of other elements indicates that the prepared nanoparticles have a high purity level.

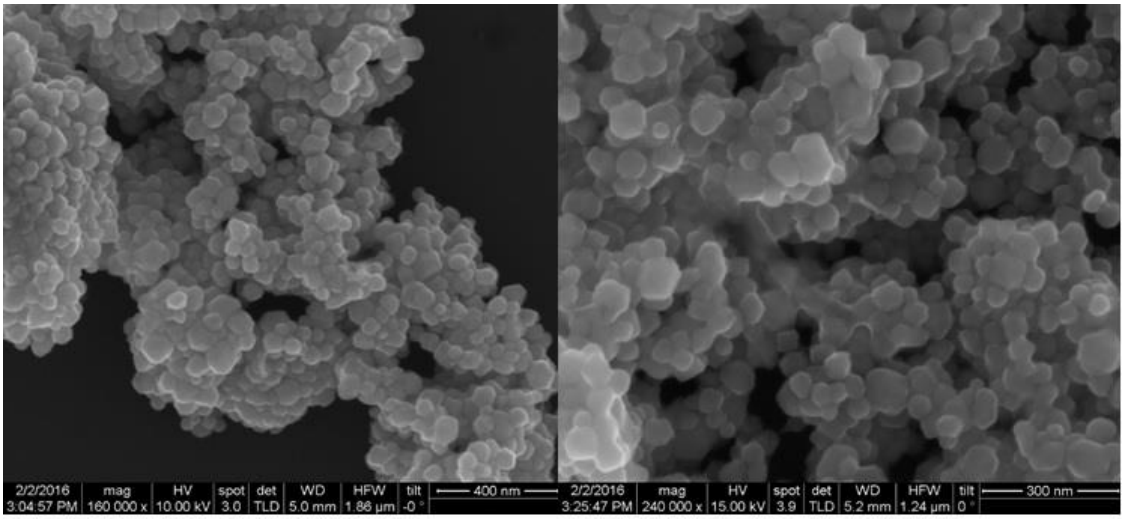

Figure 3.8. FESEM images of $CoPd_2Se_2$ nano particles.

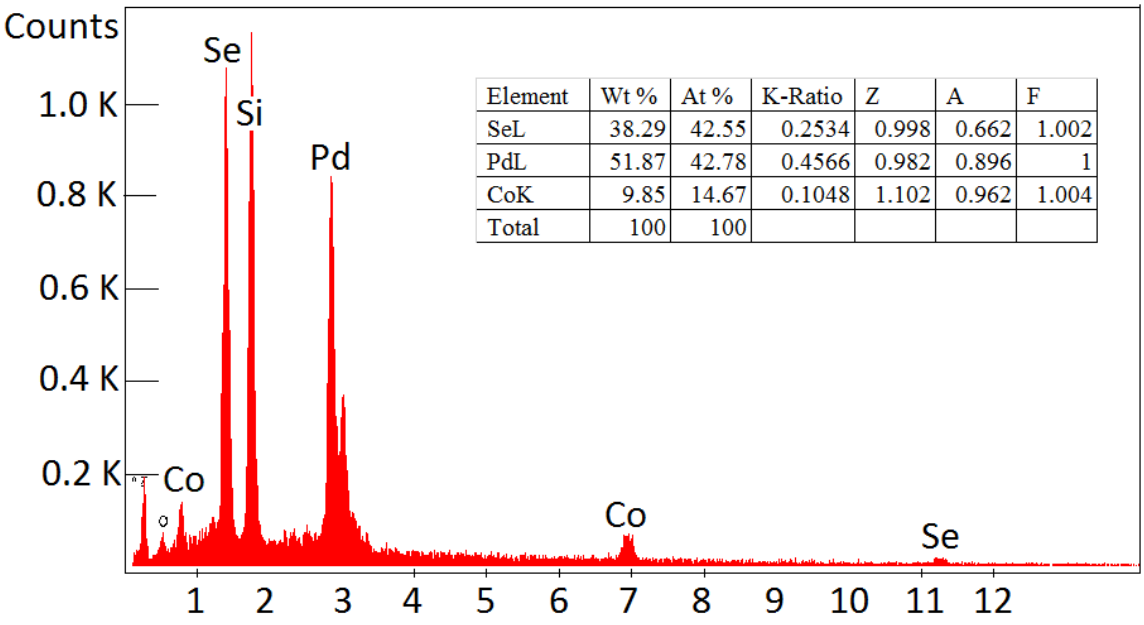

Element	Wt %	At %	K-Ratio	Z	A	F
SeL	38.29	42.55	0.2534	0.998	0.662	1.002
PdL	51.87	42.78	0.4566	0.982	0.896	1
CoK	9.85	14.67	0.1048	1.102	0.962	1.004
Total	100	100				

Figure 3.9. EDX spectrum of $CoPd_2Se_2$ nanoparticles. The inset table represents the composition of individual elements present in the system.

Rough estimation of presence of each phase from EDX measurements:

Taking 14.67 as the exact atomic percent of cobalt from EDX data, following equation can be written:

$$14.67\ Co + 42.55\ Pd + 42.78\ Se \rightarrow 14.67\ CoPd_2Se_2 + 0.79\ Pd_{17}Se_{15}$$

Table 3.2. Estimation of contribution from each phase present from EDX spectra.

Elements	**Reactant**	**$CoPd_2Se_2$**	**$Pd_{17}Se_{15}$**	**Reactant-Product**
Co	14.67	14.67	--	0
Pd	42.55	14.67 x 2=29.34	0.79 x 17 =13.43	0
Se	14.67	14.67 x 2=29.34	0.79 x 15 = 11.85	1.39

From **Table 3.2** it can be obtained that,

Approximate percentage of $CoPd_2Se_2 = \frac{14.67}{14.67+0.79}$ x 100 = 94.89 %

And, approximate percentage of $Pd_{17}Se_{15} = \frac{0.79}{0.79+14.67}$ x 100 = 5.11 %

The percentage of each phase obtained from EDX corroborates with that obtained from rietveld refinement.

3.3.5. X-ray Photoelectron Spectroscopy

XPS was employed to understand the elemental composition of the sample. In **Figure 3.10a**, peak 781 eV corresponds to Co-3*p*. Peaks at 336.3 eV and 341.5 eV corresponds to Pd-3$d_{5/2}$ and Pd-3$d_{3/2}$, respectively (**Figure 3.10b**). The location of the peak 3$d_{5/2}$ corresponds to +2 oxidation state of Pd. Se-3$d_{5/2}$ is located at 54.7 eV as can be seen from **Figure 3.10b** and corresponds to -2 oxidation state of Se.

3.3.6. Electrocatalytic Activity

The glassy carbon modified electrode was first activated prior to RDE measurements in N_2 saturated 0.1 M KOH solution (**Figure 3.11**). To evaluate the

electrocatalytic activity of $CoPd_2Se_2$, the linear sweep voltammetry curves were then recorded in O_2 saturated 0.1 M KOH solution, at a scan rate of 5 mVs^{-1}.

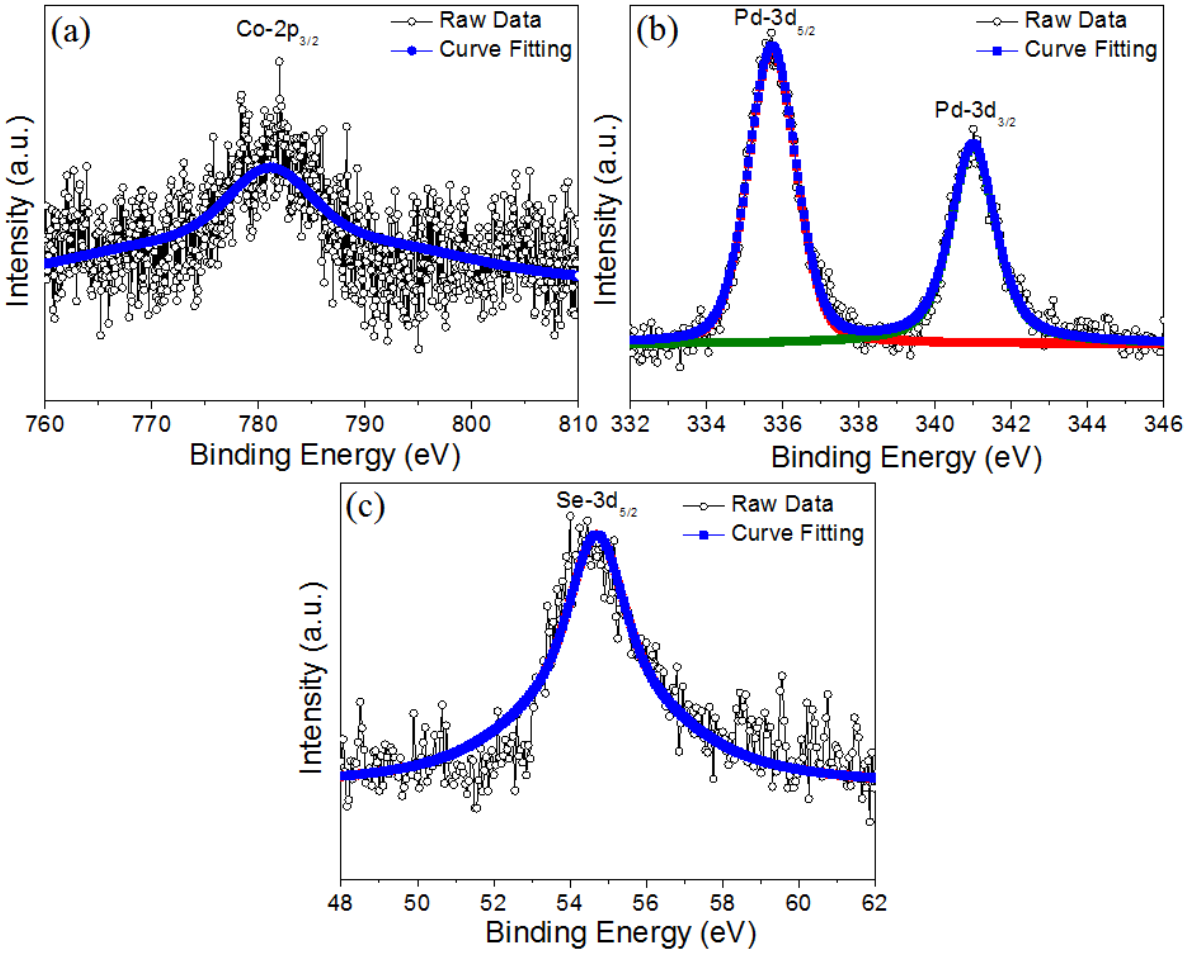

Figure 3.10. Core level XPS spectra of (a) Co, (b) Pd and (c) Se elements in $CoPd_2Se_2$ nanocomposite.

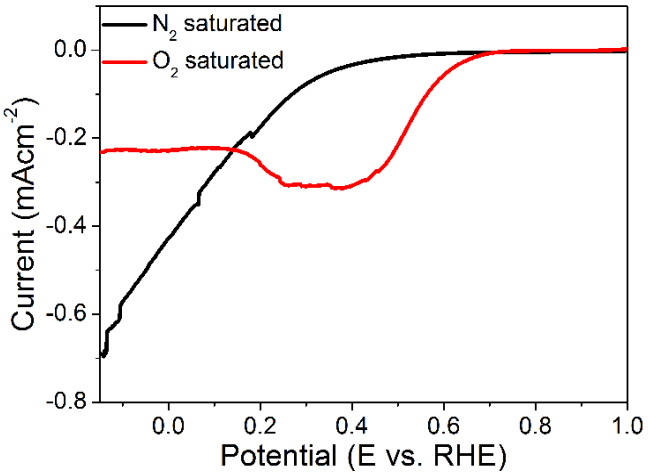

Figure 3.11. LSV polarization curve of $CoPd_2Se_2$ nanoparticle in both N_2 and O_2 saturated 0.1 M KOH solution with a sweep rate of 5 mV/sec.

But as seen from the figure, chalcogenide sample as is well-known, have lower electronic conductivity because of their semiconducting nature. Various carbon supports such as CNT, rGO, vulcan and activated carbon are known to increase the conductivity of chalcogenide samples. So, in this work, $CoPd_2Se_2$ nanoparticles are grown in-situ over vulcan XC-72. Further works are carried over $CoPd_2Se_2$/vulcan nanocomposite.

Keeping all the parameters same, RDE measurement are carried out on $CoPd_2Se_2$/vulcan modified GC electrode in N_2 saturated and O_2 saturated 0.1 M KOH (**Figure 3.12**). In the voltammetric profile, Pd-O reduction (-0.25 to -0.4V) region is well defined. It is seen that $CoPd_2Se_2$ nanoparticles, a material with little ORR activity by itself, when grown on vulcan XC-72 exhibits surprisingly high performance for ORR in alkaline medium. The polarization curves for ORR on $CoPd_2Se_2$/vulcan at different rotation rates are shown in **Figure 3.13** in which current densities are normalised with respect to the geometrical surface area (0.0706 cm^2). They all reached a well-defined diffusion limited current.

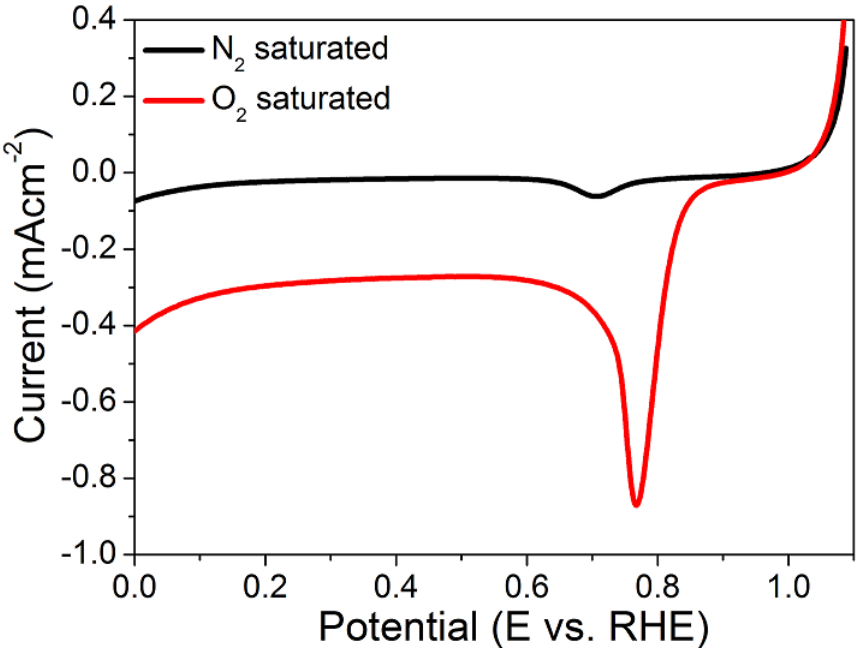

Figure 3.12. LSV polarization curve of $CoPd_2Se_2$/vulcan nanoparticle in both N_2 and O_2 saturated 0.1 M KOH solution with a sweep rate of 5 mV/sec.

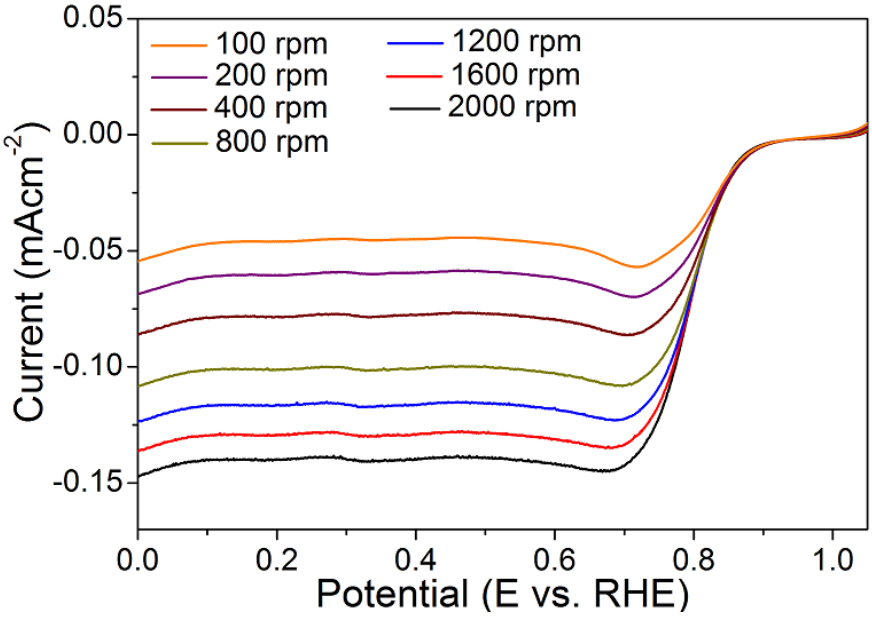

Figure 3.13. LSV polarization curve at different rpm rate in 0.1 M KOH at a sweep rate of 5 mV/sec.

The current-potential dependence of the reaction rate can be described by Koutecky-Levich (K-L) equation:

$$\frac{1}{j} = \frac{1}{j_k} + \frac{1}{j_d}$$

where j is the measured current density ($mAcm^{-2}$), and j_k and j_d are the kinetic and diffusion limited current densities.

Figure 3.14 shows the corresponding K-L plot obtained from the inverse current densities (j^{-1}) as a function of inverse square root of rotation rate ($\omega^{-1/2}$) at different potentials, respectively.

The J_d term can be termed from the Levich equation:

$$J_d = \frac{Id}{A} = 0.62\ nFD^{2/3}\upsilon^{-1/6}\omega^{1/2}C_{O2}$$

where n is the number of electron transferred, F is the Faraday's constant (96485 C mol^{-1}), A is the area of the electrode (0.0706 cm^{-2}), D is the diffusion coefficient of O_2 in 0.1 M KOH solution (1.9 x 10^{-5} cm^2s^{-1}), υ is the kinematic viscosity of the electrolyte (0.01

cm^2s^{-1}), ω is the angular frequency of rotation, $\omega = 2\pi f/60$, f is the RDE rotation rate in rpm, and C_{O2} is the concentration of molecular oxygen in 0.1 M KOH solution. (1.2×10^{-3} mol L^{-1}).

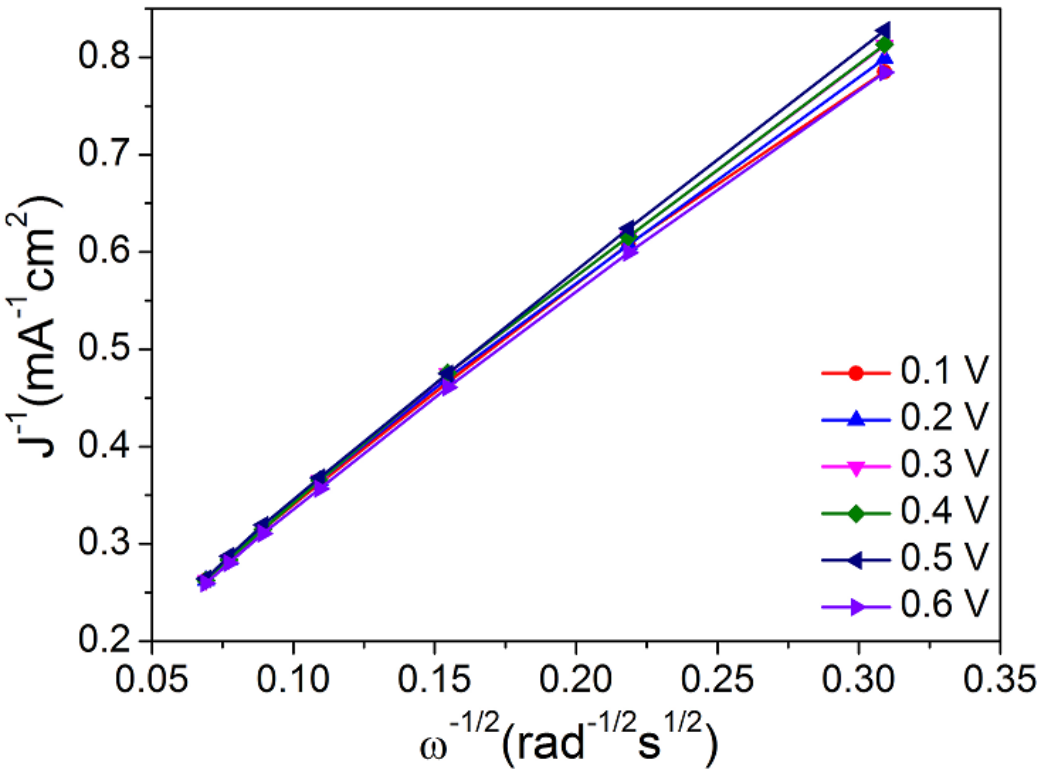

Figure 3.14. Koutecky-Levich plot for $CoPd_2Se_2$/vulcan nanocomposite at different potentials. The plots are generated from the LSV curves of all the samples tested in oxygen-saturated 0.1 M KOH solution with different rotating speeds.

The plot of 1/j vs. $\omega^{-1/2}$ for potential range of 0.1–06 V (vs. RHE) yields a series of essentially parallel straight lines, having a slope value of B. The linearity and parallelism of all the lines in **Figure 3.14** indicate that the electron number transferred per oxygen molecule and the active surface area of the catalyst does not obviously change in the potential range measured. A value of n = 4 is obtained for the catalyst $CoPd_2Se_2$, unlike Co-Se and $CoSe_2$/C which has a value of n = 3.4 and 3.5, respectively.[50]

For ORR kinetic study, the Tafel slope obtained towards the ORR was 116 mV dec^{-1} at higher overpotential (**Figure 3.15**). This Tafel slope value indicates that the oxygen reduction catalyzed by the $CoPd_2Se_2$ chalcogenide is controlled by the first charge-transfer step, similar to that of a Pt catalyst.[51] At lower overpotential tafel slope of 78 $mVdec^{-1}$ has been observed.

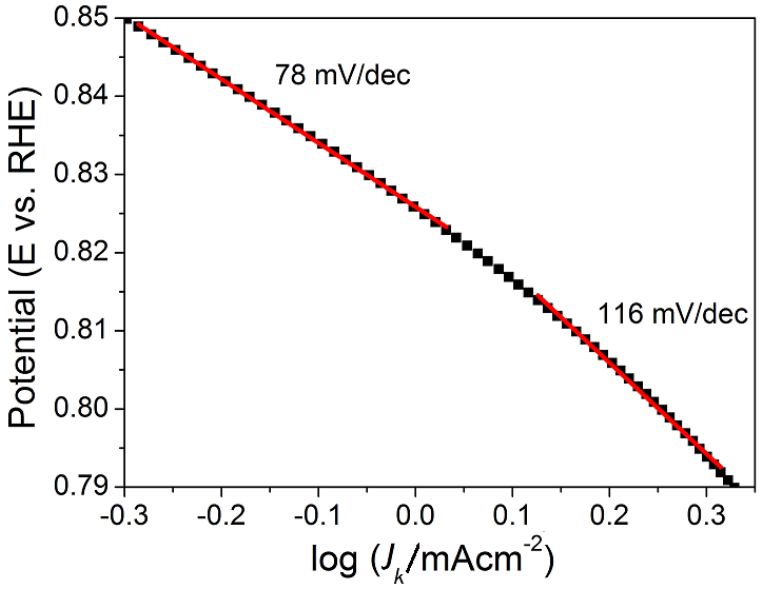

Figure 3.15. Tafel plots for ORR at $CoPd_2Se_2$ in O_2 saturated 0.1 M KOH solution.

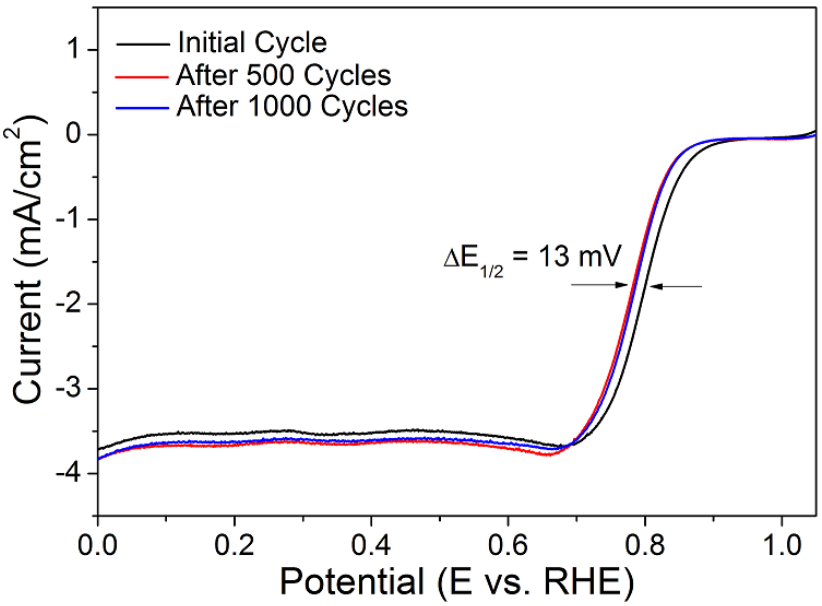

Figure 3.16. ORR polarization curves for $CoPd_2Se_2$/Vulcan before and after potential cycling between 0 to 1.0 V (1200 rpm, scan rate: 5 $mVsec^{-1}$)

To compare the electrocatalytic stability of the sample for the ORR, the stability test of the catalysts were carried out by cycling the catalyst in the potential range between −0.85 and +0.25V (vs. Hg/HgO) for 1000 cycles in O_2-saturated 0.1 M KOH solution at 25 ˚C. $E_{1/2}$ difference of only 13 mV has been observed after cycling the catalyst for 1000 cycles (**Figure 3.16**).

The density of state at Fermi level for cobalt could be changed by some electron transfer from cobalt to selenium, and this would play an important role in the chemical adsorption process of oxygen.[29, 52] Therefore, the catalytic activity of the Co–Se compounds for ORR might be attributed to the electronic structure modified by selenium.

3.4. Concluding Remarks

A novel ternary metal chalcogenide catalyst for oxygen reduction was synthesized by colloidal method. This chalcogenide catalyst demonstrated a significantly high ORR activity. It is believed that selenium might play an important role in the modification of metals such as palladium and cobalt. The chalcogen-modified electronic structures might provide the metals with the enhanced stability and catalytic activity. Further work on this ternary non-noble chalcogenide catalyst will address the detailed catalytic mechanism and the performance improvement. Since we have observed $Pd_{17}Se_{15}$ as small and inevitable impurity phase during the course of the synthesis, we targeted the synthesis of this binary phase in form. The details about the synthesis, characterization and electrochemical properties of $Pd_{17}Se_{15}$ are explained in the next chapter.

3.5. References

1. McLean, G. F.; Niet, T.; Prince-Richard, S.; Djilali, N., *Int. J. Hydrogen Energ.* **2002,** *27* (5), 507-526.

2. Kinoshita, K.; Electrochemical, S., *Electrochemical oxygen technology*. Wiley: New York, 1992.

3. Lipp, L.; Gottesfeld, S.; Chlistunoff, J., *J. Appl. Electrochem.* **2005,** *35* (10), 1015-1024.

4. Carlsson, L.; Öjefors, L., *J. Electrochem. Soc.* **1980,** *127* (3), 525-528.

5. Yang, C.-C., *Int. J. Hydrogen Energ.* **2004,** *29* (2), 135-143.

6. Morallón, E.; Vázquez, J. L.; Aldaz, A., *J. Electroanal. Chem.* **1992,** *334* (1–2), 323-338.

7. Spendelow, J. S.; Wieckowski, A., *Phys. Chem. Chem. Phys.* **2007,** *9* (21), 2654-2675.

8. Li, W.; Zhou, W.; Li, H.; Zhou, Z.; Zhou, B.; Sun, G.; Xin, Q., *Electrochim. Acta* **2004,** *49* (7), 1045-1055.

9. Yang, H.; Coutanceau, C.; Léger, J.-M.; Alonso-Vante, N.; ClaudeLamy, *J. Electroanal. Chem.* **2005,** *576* (2), 305-313.

10. Salgado, J. R. C.; Antolini, E.; Gonzalez, E. R., *Appl. Catal. B: Environmental* **2005,** *57* (4), 283-290.

11. Yang, H.; Alonso-Vante, N.; Léger, J.-M.; Lamy, C., *J. Phys. Chem. B* **2004,** *108* (6), 1938-1947.

12. Shao, Y.; Zhang, S.; Wang, C.; Nie, Z.; Liu, J.; Wang, Y.; Lin, Y., *J. Power Sources* **2010,** *195* (15), 4600-4605.

13. Wang, J.; Chen, Y.; Liu, H.; Li, R.; Sun, X., *Electrochem. Commun.* **2010,** *12* (2), 219-222.

14. Wen, Z.; Liu, J.; Li, J., *Adv. Mater.* **2008,** *20* (4), 743-747.

15. Huo, R.; Jiang, W.-J.; Xu, S.; Zhang, F.; Hu, J.-S., *Nanoscale* **2014,** *6* (1), 203-206.

16. Wei, Z. D.; Chan, S. H.; Li, L. L.; Cai, H. F.; Xia, Z. T.; Sun, C. X., *Electrochim. Acta* **2005,** *50* (11), 2279-2287.

17. Tang, C.; Pu, Z.; Liu, Q.; Asiri, A. M.; Sun, X., *Electrochim. Acta* **2015,** *153*, 508-514.

18. Faber, M. S.; Dziedzic, R.; Lukowski, M. A.; Kaiser, N. S.; Ding, Q.; Jin, S., *J. Am. Chem. Soc.* **2014,** *136* (28), 10053-10061.

19. Wang, H. L.; Liang, Y. Y.; Li, Y. G.; Dai, H. J., *Angew. Chem. Int. Ed.* **2011,** *50* (46), 10969-10972.

20. Kong, D.; Wang, H.; Lu, Z.; Cui, Y., *J. Am. Chem. Soc.* **2014,** *136* (13), 4897-4900.

21. Liu, Q.; Shi, J.; Hu, J.; Asiri, A. M.; Luo, Y.; Sun, X., *ACS Appl. Mater. Inter.* **2015,** *7* (7), 3877-3881.

22. Zhang, H.; Lei, L.; Zhang, X., *RSC Adv* .**2014,** *4* (97), 54344-54348.

23. Chhowalla, M.; Shin, H. S.; Eda, G.; Li, L.-J.; Loh, K. P.; Zhang, H., *Nat. Chem.* **2013,** *5* (4), 263-275.

24. Chen, S.; Duan, J.; Tang, Y.; Jin, B.; Zhang Qiao, S., *Nano Energ.* **2015,** *11*, 11-18.

25. Wang, H.; Lu, Z.; Kong, D.; Sun, J.; Hymel, T. M.; Cui, Y., *ACS Nano* **2014,** *8* (5), 4940-4947.

26. Duan, J. J.; Chen, S.; Chambers, B. A.; Andersson, G. G.; Qiao, S. Z., *Adv. Mater.* **2015,** *27* (28), 4234-4241.

27. Feng, Y.; He, T.; Alonso-Vante, N., *Chem. Mater.* **2008,** *20* (1), 26-28.

28. Feng, Y. J.; Gago, A.; Timperman, L.; Alonso-Vante, N., *Electrochim. Acta* **2011,** *56* (3), 1009-1022.

29. Vante, N. A.; Jaegermann, W.; Tributsch, H.; Honle, W.; Yvon, K., *J. Am. Chem. Soc.* **1987,** *109* (11), 3251-3257.

30. Solorzaferia, O.; Ellmer, K.; Giersig, M.; Alonsovante, N., *Electrochim. Acta* **1994,** *39* (11-12), 1647-1653.

31. Alonso-Vante, N.; Bogdanoff, P.; Tributsch, H., *J. Catal.* **2000,** *190* (2), 240-246.

32. Le Rhun, V.; Garnier, E.; Pronier, S.; Alonso-Vante, N., *Electrochem. Commun.* **2000,** *2* (7), 475-479.

33. Schmidt, T. J.; Paulus, U. A.; Gasteiger, H. A.; Alonso-Vante, N.; Behm, R. J., *J Electrochem. Soc.* **2000,** *147* (7), 2620-2624.

34. Bron, M.; Bogdanoff, P.; Fiechter, S.; Hilgendorff, M.; Radnik, J.; Dorbandt, I.; Schulenburg, H.; Tributsch, H., *J. Electroanal. Chem.* **2001,** *517* (1–2), 85-94.

35. Cao, D.; Wieckowski, A.; Inukai, J.; Alonso-Vante, N., *J. Electrochem. Soc.* **2006,** *153* (5), A869-A874.

36. Papageorgopoulos, D. C.; Liu, F.; Conrad, O., *Electrochim. Acta* **2007,** *52* (15), 4982-4986.

37. Kulesza, P. J.; Miecznikowski, K.; Baranowska, B.; Skunik, M.; Kolary-Zurowska, A.; Lewera, A.; Karnicka, K.; Chojak, M.; Rutkowska, I.; Fiechter, S.; Bogdanoff, P.; Dorbandt, I.; Zehl, G.; Hiesgen, R.; Dirk, E.; Nagabhushana, K. S.; Boennemann, H., *J. Appl. Electrochem.* **2007,** *37* (12), 1439-1446.

38. Inukai, J. J.; Cao, D. X.; Wieckowski, A.; Chang, K. C.; Menzel, A.; Komanicky, V.; You, H., *J. Phys. Chem. C* **2007,** *111* (45), 16889-16894.

39. Colmenares, L.; Jusys, Z.; Behm, R. J., *J. Phys. Chem. C* **2007,** *111* (3), 1273-1283.

40. Delacôte, C.; Lewera, A.; Pisarek, M.; Kulesza, P. J.; Zelenay, P.; Alonso-Vante, N., *Electrochim. Acta* **2010,** *55* (26), 7575-7580.

41. Lee, K.; Zhang, L.; Zhang, J., *Electrochem. Commun.* **2007,** *9* (7), 1704-1708.

42. Bron, M.; Bogdanoff, P.; Fiechter, S.; Dorbandt, I.; Hilgendorff, M.; Schulenburg, H.; Tributsch, H., *J. Electroanal. Chem.* **2001,** *500* (1–2), 510-517.

43. Nekooi, P.; Akbari, M.; Amini, M. K., *Int. J. Hydrogen Energ.* **2010,** *35* (12), 6392-6398.

44. Feng, Y.; He, T.; Alonso-Vante, N., *Electrochim. Acta* **2009,** *54* (22), 5252-5256.

45. Vielhaber, E.; Hoppe, R., *Z. Anorg. Allg. Chem.* **1968,** *360* (1-2), 7-14.

46. Pocha, R.; Lohnert, C.; Johrendt, D., *J. Solid State Chem.* **2007,** *180* (1), 191-197.

47. Mourdikoudis, S.; Liz-Marzan, L. M., *Chem. Mater.* **2013,** *25* (9), 1465-1476.

48. Chen, Y. Z.; Luo, X. H.; Yue, G. H.; Luo, X. T.; Peng, D. L., *Mater. Chem. Phys.* **2009,** *113* (1), 412-416.

49. Carenco, S.; Boissiere, C.; Nicole, L.; Sanchez, C.; Le Floch, P.; Mezailles, N., *Chem. Mater.* **2010,** *22* (4), 1340-1349.

50. Feng, Y. J.; He, T.; Alonso-Vante, N., *Electrochim. Acta* **2009,** *54* (22), 5252-5256.

51. Zhang, K.; Yue, Q.; Chen, G.; Zhai, Y.; Wang, L.; Wang, H.; Zhao, J.; Liu, J.; Jia, J.; Li, H., *J. Phys. Chem. C* **2011,** *115* (2), 379-389.

52. Lee, K.; Savadogo, O.; Ishihara, A.; Mitsushima, S.; Kamiya, N.; Ota, K., *J. Electrochem. Soc.* **2006,** *153* (1), A20-A24.

Chapter 4

4. Facile synthesis of stable $Pd_{17}Se_{15}$ phase towards electrochemical oxygen reduction

4.1. Introduction

Platinum and platinum based catalysts are considered as the most popular and efficient catalyst material for ORR.[1] However, due to its high cost, limited resources, low stability and vulnerability to fuel poisoning effects, its application is severely hindered and bulk production of Pt-based cathodes is restricted.[2-6] Therefore, the development of Pt-free electrocatalysts for ORR with improved catalytic activity and durability is highly desirable but remains a significant challenge.

As a potential replacement for the Pt electrocatalyst for ORR, palladium (Pd) has received considerable attention because of its similar physical properties to those of Pt, including a face-centered cubic (fcc) crystal structure, a similar atomic size and electronic configuration.[7] In addition, it is less expensive and more abundant than Pt. Various palladium based compounds/alloys such as PdFe,[8] PtPd,[9] Pd_3Sn,[10] PdCo, PdSn, PdCoSn, PdAgSn, PdNiSn,[11] show good activity towards ORR.

Chalcogenide based catalysts such as Rh_xS_y,[12] RuSe,[13] Ru-Mo-Se,[14] Ru-Fe-Se,[15] $CoSe_2$,[16] Co_3S_4,[17] $FeSe_2$,[18] NiSe[19] show high activity for ORR. Ruthenium selenides and their analogues are known to show quite high activity for the ORR.

Palladium based selenides are known to exist in different types of phases such as PdSe,[20] $Pd_{17}Se_{15}$,[21] Pd_7Se_4, $Pd_{2.5}Se$, Pd_3Se,[22] Pd_4Se,[23] $Pd_{4.5}Se$, Pd_7Se, Pd_8Se and $PdSe_2$.[24] $Pd_{17}Se_{15}$ phase has high stability towards harsh acidic (1M H_2SO_4) and basic (6M KOH) conditions.[21] The phase is highly conducting as seen from reported literature.[23] Various synthesis procedures have been employed for the synthesis of different phases. Synthesis of palladium selenide phases by thermal decomposition of benzylselenolates, 2-(methoxycarbonyl)ethyl-selenolates, 2-(diethylamino)ethane-selenolates and monoseleno-carboxylates have been well reported.[25-28] These phases are known to promote wide variety of applications such as in organic and electro-catalysis, in dye-sensitized solar cells, in electronics industry and in lithography.

4.2. Experimental Section

4.2.1. Synthesis

4.2.1.1. Chemicals

Palladium acetylacetonate ($Pd(C_5H_7O_2)_2$, 99%), selenous acid (H_2SeO_3, 98%), sodium borohydride ($NaBH_4$) and nafion binder (5 wt%) were purchased from Sigma-Aldrich. Polyvinyl pyrrollidone (PVP) was purchased from SDFCL and tetraethylene glycol ($C_8H_{18}O_5$) was purchased from Alfa Aesar. All the reagents were used without further purification. Distilled water (18.2 MΩcm) was used throughout the synthesis and measurements.

4.2.1.2. Synthesis of $Pd_{17}Se_{15}$

$Pd_{17}Se_{15}$ nanoparticles were synthesized by polyol synthesis method. $Pd(acac)_2$ (0.09 mmol) and 0.108 mmol H_2SeO_3 (0.1 mmol) were mixed together in 15 ml TEG in a 50 ml two-necked RB. 40 mg $NaBH_4$ was then added to the solution followed by stirring thoroughly. The RB was then fitted to a condenser, vacummised and purged with Ar gas. It was then heated at 220 ^oC for 3 h. The product obtained was repeatedly washed with hexane-ethanol mixture for several times and then dried in vacuum oven at 60 ^oC for 6 h.

4.2.2. Characterization

4.2.2.1. Powder X-ray Diffraction (PXRD)

The PXRD measurements were done at room temperature on a Rigaku miniflex X-ray diffractometer with Cu-Kα X-ray source (λ = 1.5406 Å), equipped with a position sensitive detector in the angular range $20^o \leq 2\theta \leq 60^o$ with the step size 0.02^o and scan rate of 1 sec/step calibrated against corundum standard. The experimental patterns were compared to the pattern simulated from the database.

4.2.2.2. Elemental Analysis

Quantitative microanalysis on all the samples were performed with a FEI NOVA NANOSEM 600 instrument equipped with an EDAX® instrument. Data were acquired with an accelerating voltage of 20 kV and a 100 sec accumulation time. The EDAX analysis was performed using P/B-ZAF standardless method (where, Z = atomic no. correction factor, A = absorption correction factor, F = fluorescence factor, P/B = peak to background model) on selected spots and points.

4.2.2.3. Transmission Electron Microscopy (TEM)

TEM images and selected area electron diffraction patterns were collected using a JEOL JEM-2010 TEM instrument. The samples for these measurements were prepared by sonicating the nanocrystalline intermetallic powders in ethanol and drop-casting a small volume onto a carbon-coated copper grid.

4.2.2.4. X-ray Photoelectron Spectroscopy (XPS)

XPS measurement was performed on an Omicron Nanotechnology spectrometer using a Mg−Kα (λ = 1253.6 eV) X-ray source with a relative composition detection better than 0.1%.

4.2.2.5. Electrochemical Studies

All the electrochemical measurements were carried out using a CHI 760E electrochemical workstation with three electrode channels at room temperature. A conventional three electrode set-up consisting of a glassy carbon (GC) (having diameter 3 mm) as working electrode, platinum wire as counter electrode and Hg/HgO (MMO) as reference electrode were used. Before all the measurements, the electrolyte was de-aerated with continuous purging of nitrogen gas for 30 min. The catalyst ink was prepared by dispersing 1 mg of catalyst in 200 µL of mixed solvent solution (IPA: H_2O = 1:3 v/v). Nafion solution (5 wt%, Sigma Aldrich) is diluted with isopropyl alcohol (IPA) to 0.05 wt%. From the prepared catalyst ink, a 5 µL of the slurry was dropcasted on GC electrode and then 1 drop of 0.05 wt% of Nafion solution have been added to the dropcasted electrode and dried overnight in air. The GC electrode was polished with 0.05 µm alumina slurry and washed several times with distilled water prior to the deposition of catalyst slurry. Chronoamperometric (CA) measurements were performed in 0.1 M KOH

electrolyte solution. Linear sweep voltammetry (LSV) was recorded with a sweep rate of 5 mV/sec in 0.1 M KOH electrolyte solution under steady state conditions. Tafel plots (TP) were derived from LSV measurement.

4.3. Results and Discussions

4.3.1. Structure Analysis

$Pd_{17}Se_{15}$ exists in cubic crystal structure with space group of $Pm\bar{3}m$. The Pd atom in (1/2, 1/2, 1/2) is surrounded by a regular octahedron of selenium atoms as shown in **Figure 4.1**. The Pd-Se bond distance is about 2.58 Å. Similar to $PdSe_2$ and PdS_2, the remaining Pd atoms have either square or almost square coordination.[29]

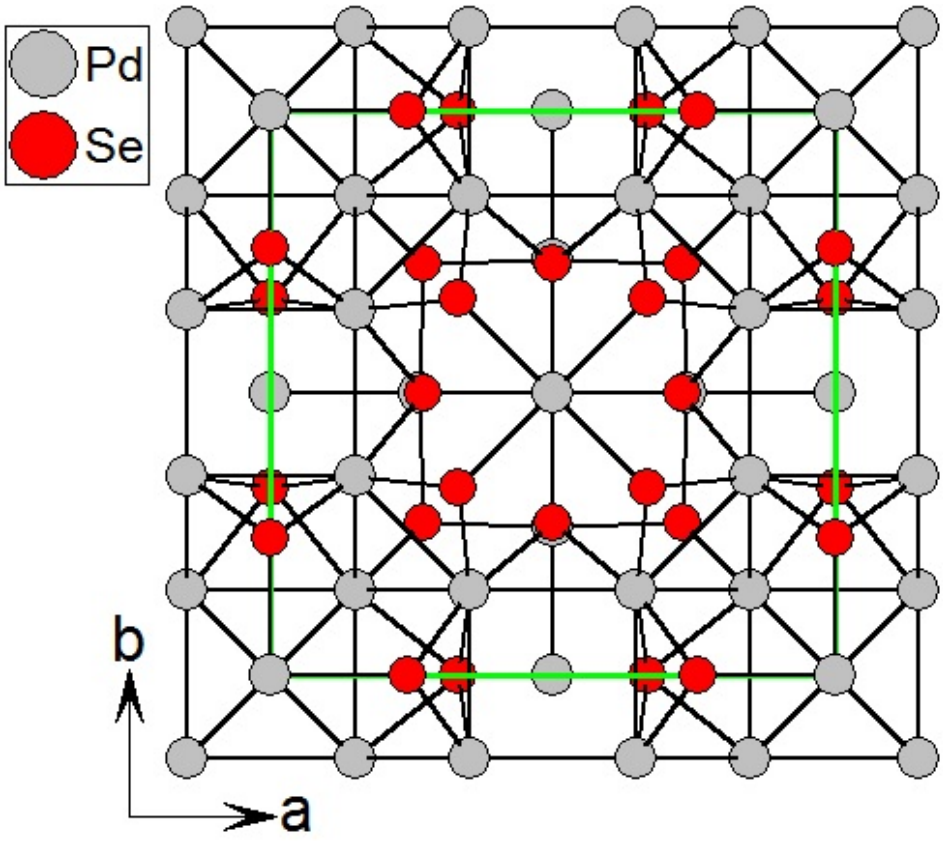

Figure 4.1. Cubic ($Pm\bar{3}m$) crystal structure of $Pd_{17}Se_{15}$ showing unit cell outlined as green solid lines.

4.3.2. Synthesis and PXRD Analysis

$Pd_{17}Se_{15}$ nanoparticles were synthesized using TEG as solvent. The advantage of using TEG is that it is a high boiling solvent that is widely used in the synthesis of metal nanoparticles. It not only act as a reducing agent but can also stabilize nanoparticle due to its chelating property. The chelating effect of the solvent is highly beneficial for controlling particle nucleation, particle growth and agglomeration of nanoparticles. It has lower polarity compared to water but its chelating property imparts water-like solubility to the solvent. $NaBH_4$ helps in the reduction of metal salts to metal nanoparticles. PVP is used as a surfactant and capping agent that controls the particle size of the particles.

Experimental powder XRD pattern of the $Pd_{17}Se_{15}$ sample prepared by colloidal synthesis method was compared with the simulated patterns from the reported crystal structure and shown in **Figure 4.2**. The prominent peaks (2θ values) observed at 27.78°, 44.2°, 48.36° correspond to the (311), (511,333) and (440) planes of $Pd_{17}Se_{15}$, respectively. The PXRD pattern of $Pd_{17}Se_{15}$ could be indexed as cubic with $Pm\bar{3}m$ space group.

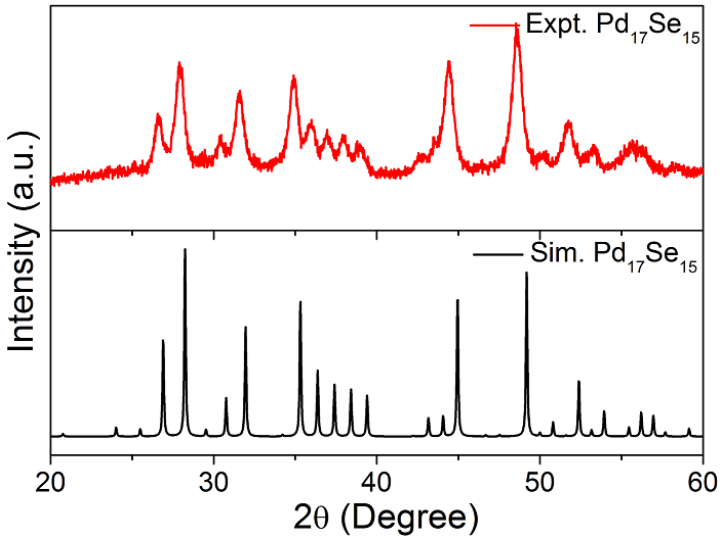

Figure 4.2. Comparison of experimental PXRD pattern with that of the simulated pattern of $Pd_{17}Se_{15}$.

4.3.3. TEM Analysis

The TEM images show that the $Pd_{17}Se_{15}$ nanoparticles are interlinked with each other and have aggregated morphology (**Figure 4.3a**) and the TEM images prove that the nanoparticles are less than 50 nm in size (**Figure 4.3b**). From HRTEM image, d-spacing (between two lattice fringes) was calculated to be 0.47 nm and 0.327 nm which corresponds to the (210) and (311) planes of the particles are exposed (**Figure 4.3c**). The SAED pattern shown in **Figure 4.3d** shows the polycrystalline nature of the nanoparticles. The diffraction pattern contains (310), (400), (510), (810), (742) planes which confirms the formation of $Pd_{17}Se_{15}$ nanoparticle.

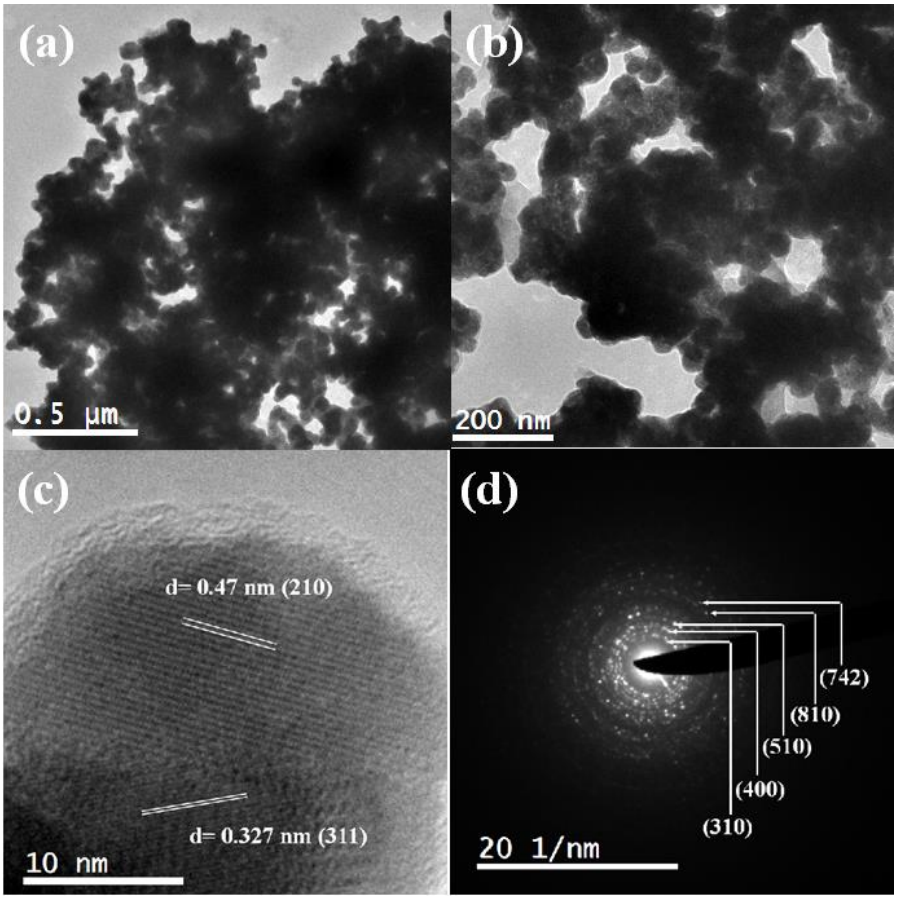

Figure 4.3. (a) TEM images shows the aggregated nature of the particle, (b) magnified TEM showing that the particles are interconnected, (c) HRTEM image shows the exposed (210) and (311) planes and (d) SAED pattern of $Pd_{17}Se_{15}$ nano particles shows polycrystalline nature of the nanoparticles.

4.3.4. FESEM Analysis

FESEM images of the particles shows the highly aggregated nature of the system. Elemental mapping and the EDX spectra of the as-prepared sample are shown in **Figure 4.4** and **Figure 4.5**, respectively. The EDX and the elemental mapping from the FESEM analysis clearly confirm the presence of Pd and Se in the $Pd_{17}Se_{15}$ nanoparticles. In the EDX spectrum, peaks are observed at 0.25 keV and 2.8 keV for Pd and 1.3 keV and 11.25 keV for Se. The absence of other elements indicates that the prepared nanoparticles have high purity level.

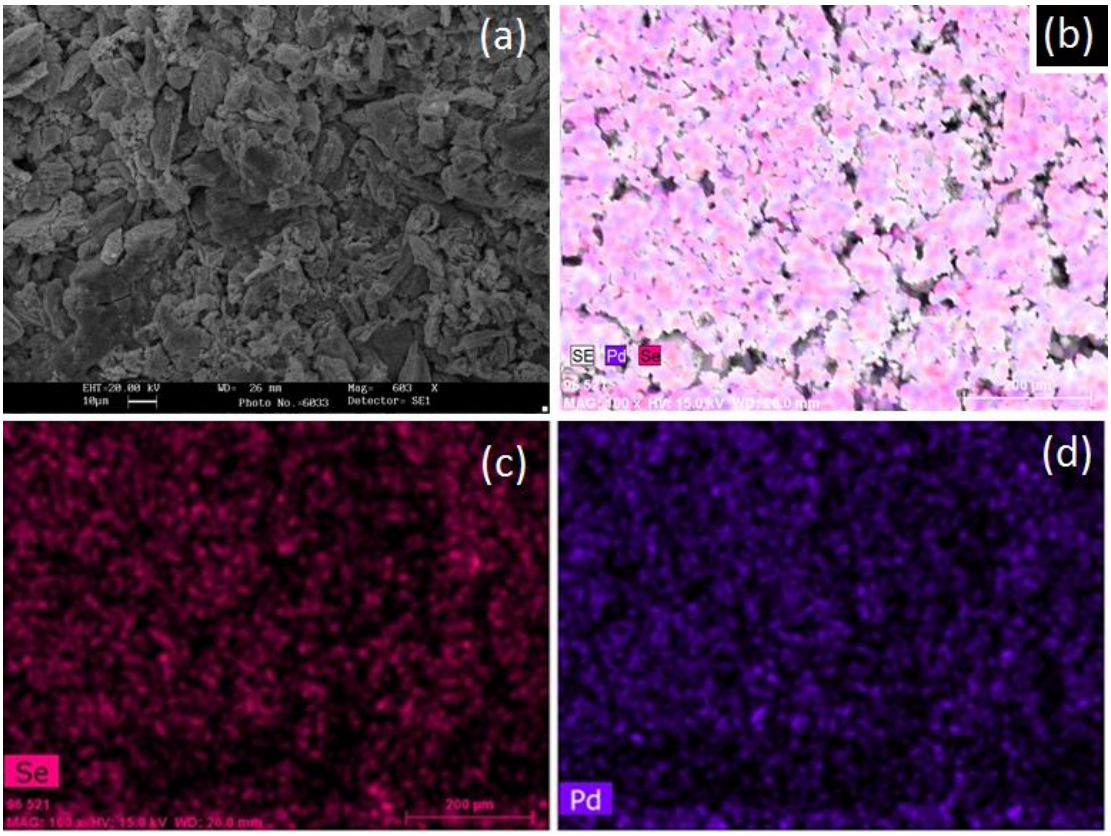

Figure 4.4. (a) SEM images of the as-prepared $Pd_{17}Se_{15}$, (b) elemental mapping of $Pd_{17}Se_{15}$ shows the presence of both the elements. Elemental mapping of individual elements – (c) Se (pink) and (d) Pd (purple).

From the EDX elemental analysis, the atomic percentage of Pd and Se are found to be 60.31±1.6 % and 39.69±1.2 %, respectively, which is in good agreement with the expected stoichiometric ratio of 17:15 for the compound $Pd_{17}Se_{15}$.

4.3.5. X-ray Photoelectron Spectroscopy (XPS)

XPS was employed to understand the elemental composition of the sample. From **Figure 4.6a**, it is clear that Pd-3$d_{5/2}$ and Pd-3$d_{3/2}$ are located at 336.3 eV and 341.5 eV, respectively. The location of the peak 3$d_{5/2}$ corresponds to +2 oxidation state of Pd. Se-3$d_{5/2}$ is located at 54.7 eV as can be seen from **Figure 4.6b** and corresponds to -2 oxidation state of Se.

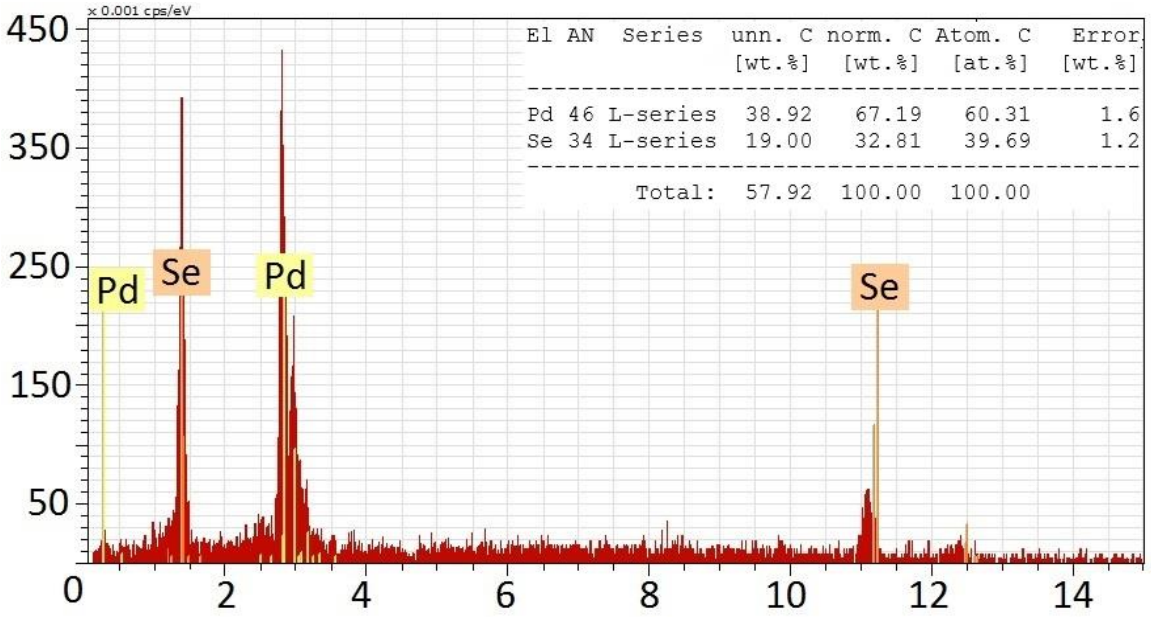

Figure 4.5. EDX spectrum of $Pd_{17}Se_{15}$ nanoparticles. The elemental composition of the sample is provided as inset.

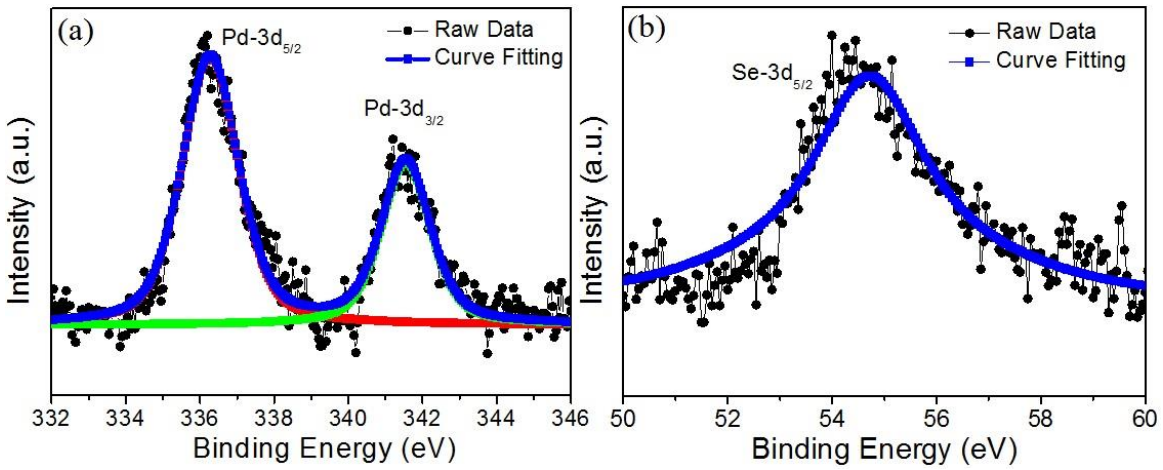

Figure 4.6. Core level XPS spectra of $Pd_{17}Se_{15}$ nanoparticles. High resolution XPS spectrum of (a) Pd-3$d_{5/2}$, Pd-3$d_{3/2}$ and (b) Se-3*d*.

4.3.6. Electrocatalytic Activity

Cyclic voltammetry (CV) of a $Pd_{17}Se_{15}$ nanoparticles, coated on glassy carbon rotating disk electrode (GC-RDE), in both O_2-saturated and N_2-saturated 0.1 M KOH solution is shown in **Figure 4.7**. In the N_2-saturated voltametric profile, a very weak PdO reduction (-0.25 to -0.4V vs. RHE) region is seen. In O_2 saturated solution, enhancement in current in the range (0 to -0.4 V vs. RHE) is observed.

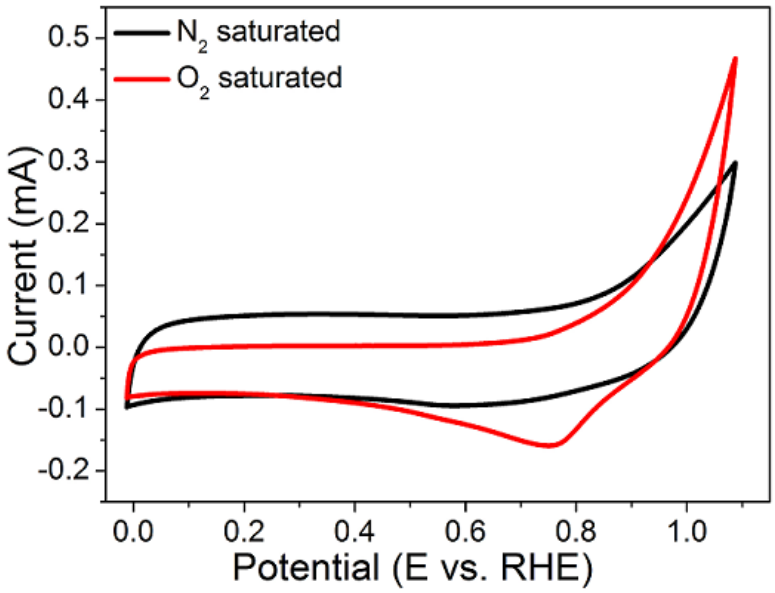

Figure 4.7. CV curve of the as-prepared sample in N_2 saturated (black line) and O_2 saturated (red line) 0.1 M KOH solution with a sweep rate of 50 mV/sec.

RDE measurements were carried out at different rotation rate in 0.1 M KOH. The polarization curves for ORR at different rotation rates are shown in **Figure 4.8** in which current densities are normalised with respect to the geometrical surface area (0.0706 cm^2). They all reached a well-defined diffusion limited current. At 1600 rpm, the catalyst showed an ORR onset potential of about 0.87 V versus RHE. The ORR current density at 1600 rpm was about 5.8 $mAcm^{-2}$ at 0.7 V versus RHE. **Figure 4.9** shows the corresponding K-L plot obtained from the inverse current densities (j^{-1}) as a function of inverse square root of rotation rate ($\omega^{-1/2}$) at different potentials, respectively.

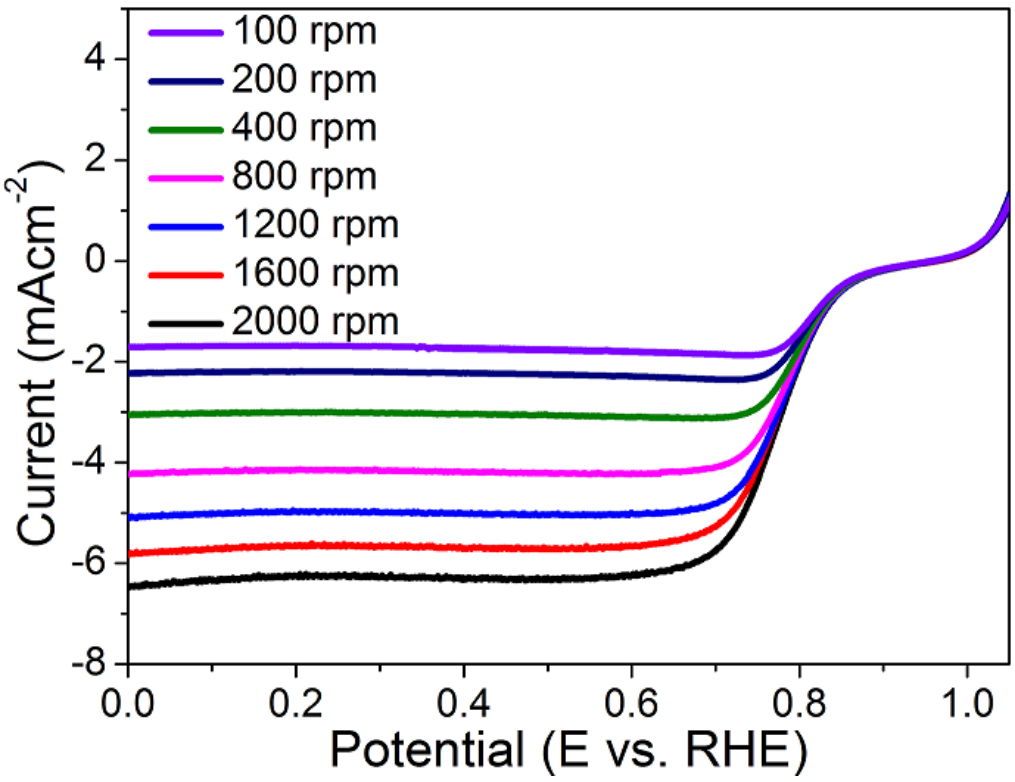

Figure 4.8. Linear Polarization curves of $Pd_{17}Se_{15}$ at different rpm in 0.1 M KOH with a sweep rate of 5 mV/sec.

The current-potential dependence of the reaction rate can be described by Koutecky-Levich (K-L) equation:

$$\frac{1}{j} = \frac{1}{j_k} + \frac{1}{j_d}$$

where j is the measured current density (mAcm^{-2}), and j_k and j_d are the kinetic and diffusion limited current densities, respectively.

Linear Sweep Voltammetry measurements were carried out under an oxygen saturated environment by sweeping the potential between -0.85 V and 0.25 V vs. Hg/HgO. The J_d term can be termed from the Levich equation:

$$J_d = \frac{Id}{A} = 0.62\ nFD^{2/3}\upsilon^{-1/6}\omega^{1/2}C_{O2}$$

where n is the number of electron transferred, F is the Faraday's constant (96485 C mol^{-1}), A is the area of the electrode (0.0706 cm^{-2}), D is the diffusion coefficient of O_2 in 0.1 M KOH solution (1.9 x 10^{-5} cm^{2}s^{-1}), υ is the kinematic viscosity of the electrolyte (0.01 cm^{2}s^{-1}), ω is the angular frequency of rotation, $\omega = 2\pi f/60$, f is the RDE rotation rate in rpm, and C_{O2} is the concentration of molecular oxygen in 0.1 M KOH solution (1.2 x 10^{-3} mol L^{-1}).

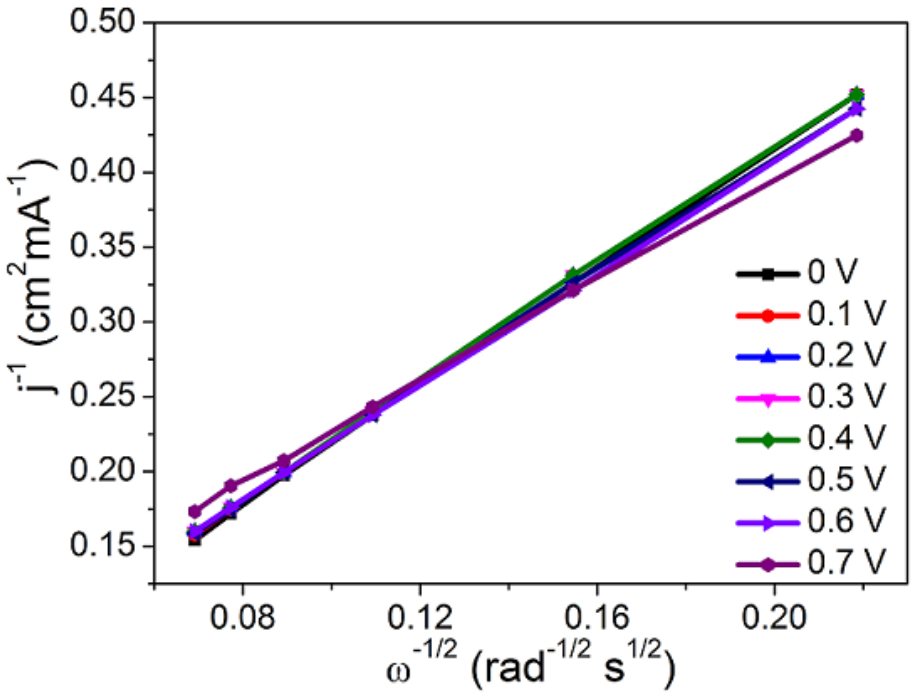

Figure 4.9. Corresponding koutecky-levich (K-L) plot derived at different potential.

The K-L plots are linear indicating first order dependen**ce** of the kinetics of ORR on $Pd_{17}Se_{15}$ surface. The slope and intercept of the straight lines will give "B-factor" and kinetic current density (j_k) respectively. The number of electrons calculated from the slope of K-L plots is close to five on an average. Four electrons are expected theoretically but an observed extra electron can be due to a parasitic reaction going on in parallel.[30]

In ORR kinetic study, the tafel slope obtained for the catalyst was 98 mV dec^{-1} as shown in **Figure 4.10**. This Tafel slope value indicates that the oxygen reduction catalyzed by the $Pd_{17}Se_{15}$ chalcogenide is controlled by the first charge-transfer step, similar to that of a Pt catalyst.

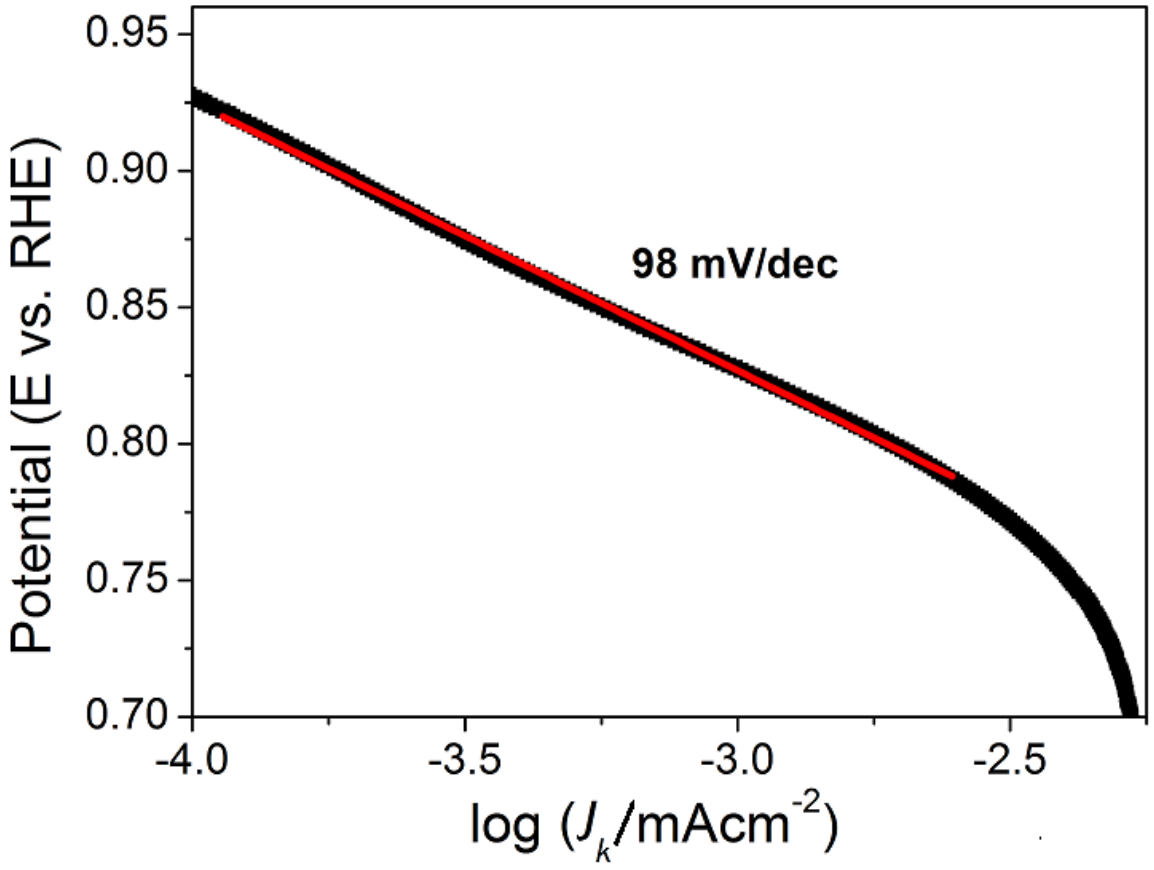

Figure 4.10. Tafel plots for ORR at $Pd_{17}Se_{15}$ in O_2 saturated 0.1 M KOH solution.

4.4. Concluding Remarks

Nanostructured $Pd_{17}Se_{15}$ has been successfully synthesized using colloidal synthesis route. The nanoparticles exhibited cubic $Pm\bar{3}m$ space group. The catalytic activity of $Pd_{17}Se_{15}$ exhibited activity similar to that of $CoPd_2Se_2$. Excess selenium in the case of $Pd_{17}Se_{15}$, compared to $CoPd_2Se_2$, might play an important role in the modification of fermi-level of palladium. Further work on this chalcogenide catalyst will address the detailed catalytic mechanism and the performance improvement. Theoretical work is under progress that will put further insight into the role of selenium in enhancing the ORR activity.

4.5. References

1. Stamenkovic, V. R.; Fowler, B.; Mun, B. S.; Wang, G.; Ross, P. N.; Lucas, C. A.; Marković, N. M., *Science* **2007,** *315* (5811), 493-497.

2. Shao, Y.; Zhang, S.; Wang, C.; Nie, Z.; Liu, J.; Wang, Y.; Lin, Y., *J. Power Sources* **2010,** *195* (15), 4600-4605.

3. Wang, J.; Chen, Y.; Liu, H.; Li, R.; Sun, X., *Electrochem. Commun.* **2010,** *12* (2), 219-222.

4. Wen, Z.; Liu, J.; Li, J., *Adv. Mater.* **2008,** *20* (4), 743-747.

5. Huo, R.; Jiang, W.-J.; Xu, S.; Zhang, F.; Hu, J.-S., *Nanoscale* **2014,** *6* (1), 203-206.

6. Wei, Z. D.; Chan, S. H.; Li, L. L.; Cai, H. F.; Xia, Z. T.; Sun, C. X., *Electrochim. Acta* **2005,** *50* (11), 2279-2287.

7. Liu, H.; Koenigsmann, C.; Adzic, R. R.; Wong, S. S., *ACS Catal.* **2014,** *4* (8), 2544-2555.

8. Neergat, M.; Gunasekar, V.; Rahul, R., *J. Electroanal. Chem.* **2011,** *658* (1-2), 25-32.

9. Li, H. Q.; Sun, G. Q.; Li, N.; Sun, S. G.; Su, D. S.; Xin, Q., *J. Phys. Chem. C* **2007,** *111* (15), 5605-5617.

10. Lu, C. Y.; Guan, W. S.; Hoang, T. K. A.; Li, Y. L.; Doan, T. N. L.; Zhao, H. B., *Int. J. Electrochem. Sci.* **2015,** *10* (6), 5077-5085.

11. Zhu, F. C.; Wang, M.; He, Y. W.; Ma, G. S.; Zhang, Z. H.; Wang, X. G., *Electrochim. Acta* **2014,** *148*, 291-301.

12. Papageorgopoulos, D. C.; Liu, F.; Conrad, O., *Electrochim. Acta* **2007,** *52* (15), 4982-4986.

13. Cao, D.; Wieckowski, A.; Inukai, J.; Alonso-Vante, N., *J. Electrochem. Soc.* **2006,** *153* (5), A869-A874.

14. Schmidt, T. J.; Paulus, U. A.; Gasteiger, H. A.; Alonso-Vante, N.; Behm, R. J., *J. Electrochem. Soc.* **2000,** *147* (7), 2620-2624.

15. Delacôte, C.; Lewera, A.; Pisarek, M.; Kulesza, P. J.; Zelenay, P.; Alonso-Vante, N., *Electrochim. Acta* **2010,** *55* (26), 7575-7580.

16. Feng, Y. J.; He, T.; Alonso-Vante, N., *Electrochim. Acta* **2009,** *54* (22), 5252-5256.

17. Feng, Y.; He, T.; Alonso-Vante, N., *Chem. Mater.* **2008,** *20* (1), 26-28.

18. Zheng, Q. L.; Cheng, X.; Li, H. Y., *Catalysts* **2015,** *5* (3), 1079-1091.

19. Swesi, A. T.; Masud, J.; Nath, M., *Energ. Environ. Sci.* **2016**.

20. Ijjaali, I.; Ibers, J. A., *Z. Kristallogr.-New Cryst. Struct.* **2001,** *216* (4), 485-486.

21. Kukunuri, S.; Karthick, S. N.; Sampath, S., *J. Mater. Chem. A* **2015,** *3* (33), 17144-17153.

22. Hannu-Kuure, M. S.; Palda'n, K.; Oilunkaniemi, R.; Laitinen, R. S.; Ahlgren, M., *J. Organomet. Chem.* **2003,** *687* (2), 538-544.

23. Kukunuri, S.; Austeria, P. M.; Sampath, S., *Chem. Commun.* **2016,** *52* (1), 206-209.

24. Olsen, T.; Rost, E.; Gronvold, F., *Acta Chem. Scand., Ser. A* **1979,** *33*, 251-256.

25. Dey, S.; Jain, V. K.; Varghese, B., *J. Organomet. Chem.* **2001,** *623* (1–2), 48-55.

26. Pal, M. K.; Jain, V. K.; Kushwah, N. P.; Wadawale, A.; Glazun, S. A.; Starikova, Z. A.; Bregadze, V. I., *J. Organomet. Chem.* **2010,** *695* (24), 2629-2634.

27. Kumbhare, L. B.; Jain, V. K.; Phadnis, P. P.; Nethaji, M., *J. Organomet. Chem.* **2007,** *692* (7), 1546-1556.

28. Kumbhare, L. B.; Jain, V. K.; Varghese, B., *Inorg. Chim. Acta* **2006,** *359* (2), 409-416.

29. Geller, S., *Acta. Cryst.* **1962,** *15*, 713-721.

30. Demarconnay, L.; Coutanceau, C.; Leger, J. M., *Electrochim. Acta* **2008,** *53* (8), 3232-3241.

5. Concluding Remarks and Future Directions

In this research, we have investigated the electrocatalytic activity of various Pd based nanomaterials. These compounds are potential candidates as anode/cathode for direct ethanol fuel cell. The compounds were synthesized using facile solvothermal and colloidal synthesis approaches. The objective of this work was to develop an efficient and low cost alternative to the current state-of-art material. We also focussed on enhancing the already available state-of art material. Motivated on the recent developments in the area of Pd and Pd-based compounds, we have selected a few interesting compounds which were never reported in nanocrystalline morphology.

In **chapter 1**, we tried doping Pd with *RE* such as Yb and Eu by 10 % and studied the electrocatalytic activity of the doped compounds towards ethanol electroxidation. To our amusement, *RE* amplified the activity of Pd by five to eight-fold in terms of specific activity and slight enhancement was observed in terms of mass activity. To study the role of *RE*, we further extended our strategy and doped Pd with transition metals such as Ni and Cr. Similar electrochemical measurements were carried out for transition metal doped Pd but the enhancement in activity was not much as compared to that by *RE* doping. Theoretical study is under progress that will give further understanding about the role of

RE in the catalytic enhancement. We also planned to dope Pd with different percentage of *RE* atoms and study their comparative electrocatalytic activity towards EOR.

In **chapter 2**, we have synthesized $CoPd_2Se_2$ in nanocrystalline form to increase the surface area and to check its activity towards electrochemical ORR. During the synthesis, $Pd_{17}Se_{15}$ was obtained as the impurity phase in every case, which is inevitable. The synthesis procedure was optimized and the impurity phase was reduced to as low as 7 %. Detailed characterization was done and ORR study was carried out.

To understand the contribution from the minor impurity phase of $Pd_{17}Se_{15}$, we synthesized the compound and characterized. The detailed studies are discussed in **chapter 3**. Electrochemical ORR measurements were carried out and both the phase were found to have similar onset potential. In addition to that both the compounds showed remarkable stability towards ORR. In future, we planned to synthesize mixed phase having different percentage of $CoPd_2Se_2$ and $Pd_{17}Se_{15}$ and study the ORR activity and stability of these samples.

After the successful results of the initial approaches, we would like to extend our strategy on different palladium based compounds. One such example is Au_xPd_{1-x}. The preliminary studies made on Au_xPd_{1-x} as efficient catalyst for the ethanol oxidation reaction and oxygen reduction reaction. The compound was synthesized following oleyl amine reduction method. The TEM image of the as-obtained compound is given in **Figure 5.1**.

TEM image in **Figure 5.1a,c** shows that the nanoparticles form well-separated cluster of particles. HRTEM image is shown in **Figure 5.1b**. Interplanar spacing calculated from the HRTEM image shows that the (111) plane of the nanoparticles are exposed. Polycrystalline nature of the sample can be confirmed from the SAED pattern of the sample shown in **Figure 5.1d**.

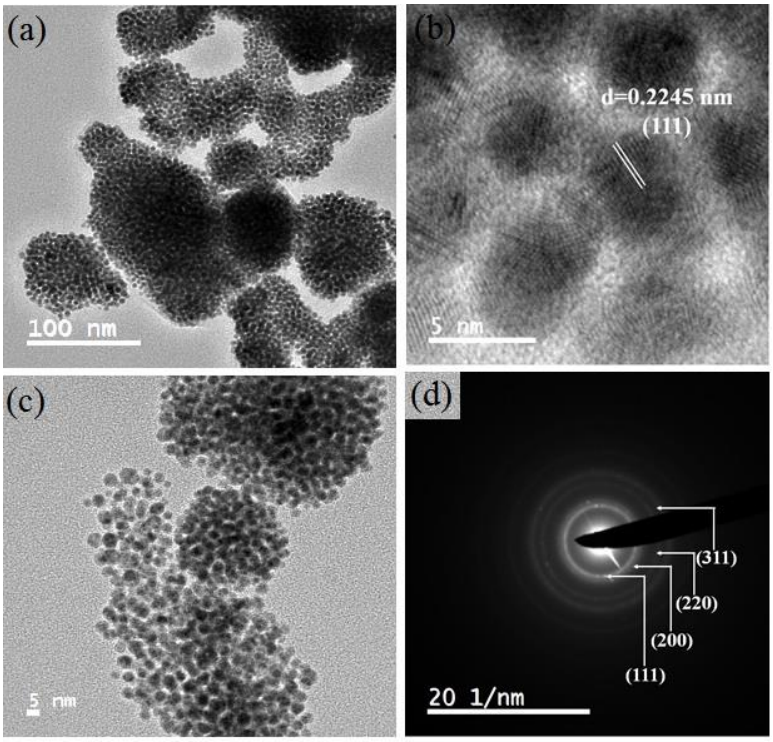

Figure 5.1. (a) TEM images of Au_xPd_{1-x} nanoparticles, (b) HRTEM image show d-spacing corresponding to (111) plane, (c) magnified TEM image of Au_xPd_{1-x} nanoparticles and (d) corresponding SAED pattern shows the polycrystalline nature of the sample.

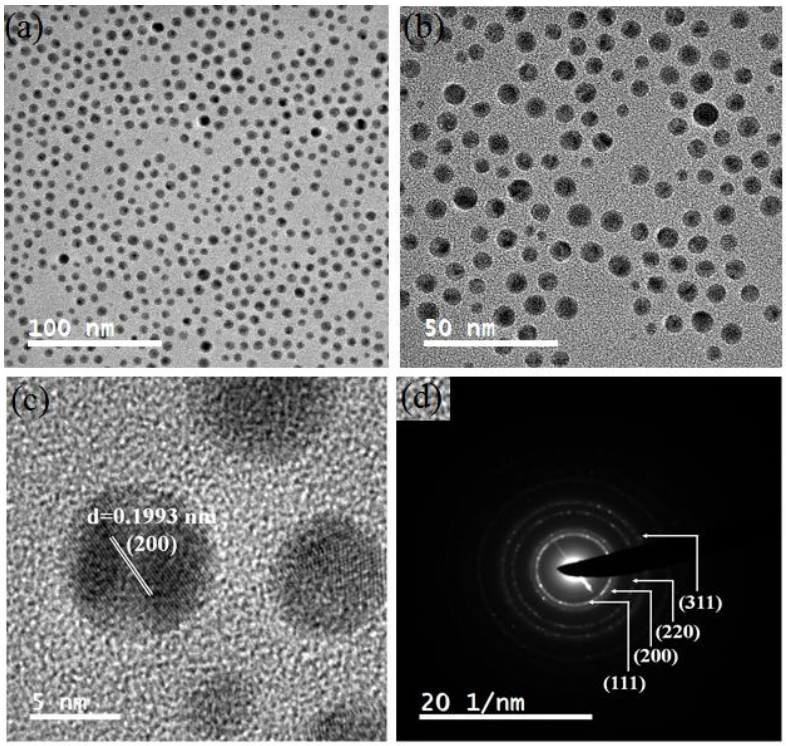

Figure 5.2. (a, b) TEM image of Au_xPd_{1-x}@Ag, (c) HRTEM image show d-spacing corresponding to (200) plane and (d) corresponding SAED pattern shows the polycrystalline nature of the sample.

The Au_xPd_{1-x} particles are then coated with Ag and the TEM images are shown in **Figure 5.2.** It can be seen that the particles do not form bunches as the Au_xPd_{1-x} sample. The particles are well-separated as can be seen in the **Figure 5.2a,b**. Unlike Au_xPd_{1-x}, (200) plane is exposed in the case of Au_xPd_{1-x}@Ag as seen in **Figure 5.2c**. SAED pattern confirms the polycrystalline nature of the sample (**Figure 5.2d**).

Electrochemical ORR activity of the uncoated Au_xPd_{1-x} can be seen in **Figure 5.3**. **Figure 5.3a** shows the cyclic voltammagram for the sample in N_2 saturated and O_2 saturated 0.1 M KOH solution with a sweep rate of 50 mV/sec. It clearly shows the activity of the sample towards ORR. Rotation rate dependent linear sweep voltammagram shows that the activity of the sample increases with increase in rotation rate. This can be attributed to the increase in O_2 diffusion with increase in rotation rate.

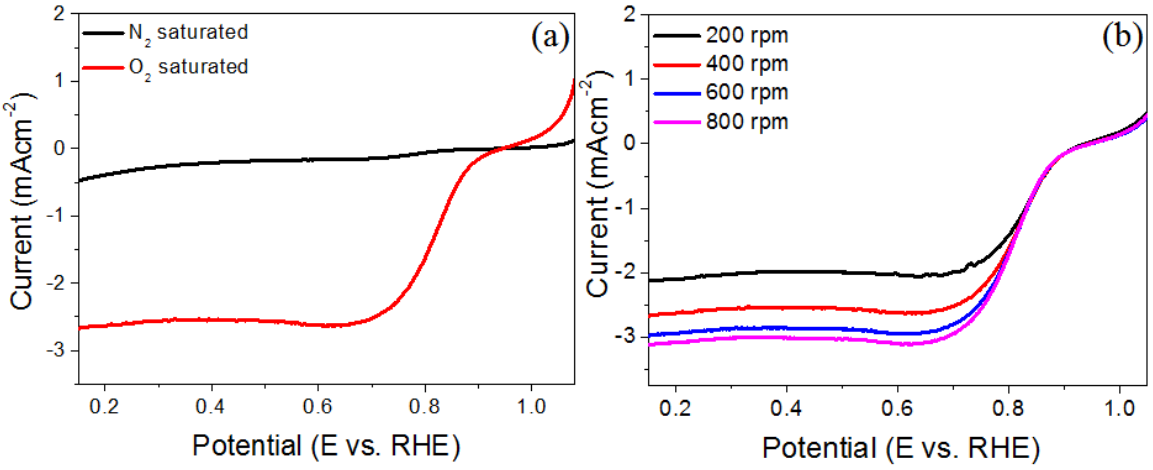

Figure 5.3. LSV polarization curve of Au_xPd_{1-x} nanoparticle (a) in both N_2 and O_2 saturated 0.1 M KOH solution with a sweep rate of 5 mV/sec, (b) at different rpm in O_2 saturated 0.1 M KOH solution.

The uncoated sample was checked for ethanol oxidation reaction. **Figure 5.4a** shows the CV curve of the sample without ethanol. **Figure 5.4b,c** shows the specific activity and the mass activity of the sample in 0.5 M KOH + 1 M EtOH solution. The sample has a specific activity of 2.8 $mAcm^{-2}$ and 4.5 mA cm^{-2} at 1st cycle and 1000th cycle,

respectively. Mass activity of 225 mA/mg_{Pd} and 400 mA/mg_{Pd} is seen at 1st cycle and at 1000th cycle, respectively. Chronoamperometric measurement at -0.2 V shows that the sample has considerable stability.

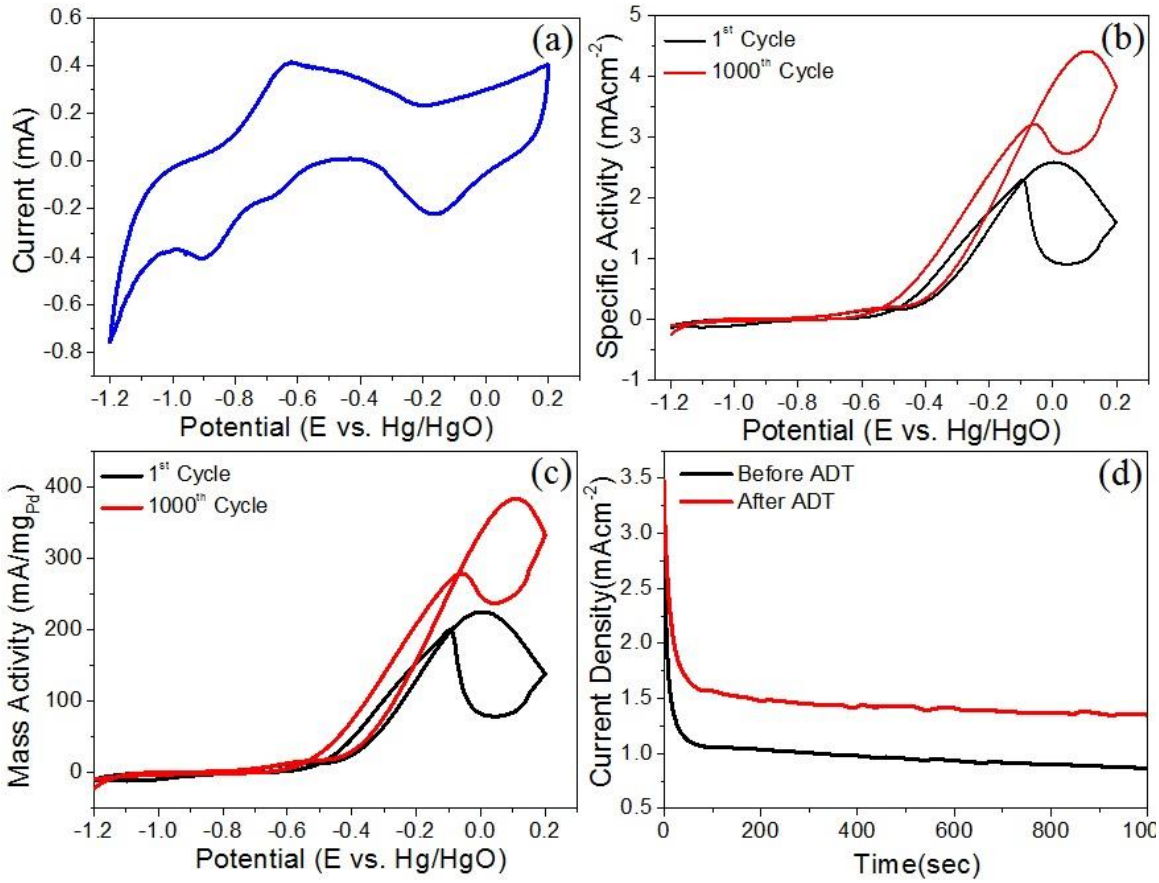

Figure 5.4. (a) CV curve obtained for Au_xPd_{1-x} in 0.5 M KOH solution at a scan rate of 50 mV/sec, (b) specific activity, (c) mass activity of Au_xPd_{1-x} with respect to cycles at a scan rate of 50 mV/sec to check the stability of the catalyst in 0.5 M KOH + 1 M EtOH, (d) chronoamperometric plots of Au_xPd_{1-x} in 0.5 M KOH + 1 M EtOH solution for 1000 sec at electrode potential of -0.2 V vs Hg/HgO

Electrochemical ORR and EOR measurements on Ag coated sample need to be performed. Comparison between the coated and the uncoated sample will reveal the efficiency of our synthetic strategy. The strategy will be extended to synthesize Ni, Co, Mn coated Au_xPd_{1-x} sample. A comparative study of the electrocatalytic activity of the samples will then be made to understand the activity of uncoated and the coated samples. This comparative study will help us to logically design catalyst having better activity in future.

In future, we planned to synthesize non-noble metal chalcogenide nanoparticles and study their activity towards hydrogen evolution reaction, oxygen reduction reaction and small organic molecule oxidation. Since, chalcogenides show supercapacitive behaviour, we will try to focus our research towards the synthesis and fabrication of electrochemical supercapacitor.

List of Publications

Publications included in Thesis

1. The role of Rare-Earths in enhancing electrocatalytic activity of Pd nanoparticles towards Ethanol Oxidation Reaction; Sarma, Saurav Ch.; Subbarao, Udumula; Jana, Rajkumar; Khulbe, Yatish; Peter, Sebastian C. (manuscript communicated)

2. Synthesis of novel hexagonal nanoparticles of $CoPd_2Se_2$ and its electrochemical ORR studies; Sarma, Saurav Ch.; Mishra, Vidyanshu; Subbarao, Udumula; Peter, Sebastian C. (manuscript under preparation)

Publications not included in Thesis

3. Structural Evolution of the Compounds $Eu_3T_2In_9$ (T = Cu and Ag) through the Superstructure of $EuCu_2Ge_2$ and their Physical Properties; Subbarao, Udumula; Sarma, Saurav Ch.; Sarkar, Sumanta; Mishra, Vidyanshu; Khulbe, Yatish; Peter, Sebastian C. (manuscript under revision)